UNIVERSITY OF CALIFORNIA, SAN DIEGO

Theory of Vortex Crystal Formation in Two-Dimensional Turbulence

A dissertation submitted in partial satisfaction of the
requirements for the degree Doctor of Philosophy
in Physics

by

Dezhe Jin

Committee in charge:

Professor Daniel H. E. Dubin, Chairman
Professor Patrick H. Diamond
Professor C. Fred Driscoll
Professor Thomas M. O'Neil
Professor Richard L. Salmon
Professor William R. Young

1999

The dissertation of Dezhe Jin is approved, and it is acceptable in quality and form for publication on microfilm:

Chair

University of California, San Diego

1999

This dissertation is dedicated to my wife Cheng-Ai,
my Mother Rong-Zi, and my Father Chang-Xi.

TABLE OF CONTENTS

LIST OF FIGURES

ACKNOWLEDGMENTS

This thesis would have not been possible without my thesis advisor, Professor Daniel Dubin, who has inspired my interest in non-neutral plasma physics, and has guided me throughout my entire research. With his keen intuition and critical mind, he has pointed me right directions, corrected my occasional blunders, and encouraged my independent thinking. A seasoned physicist, he is a powerful challenger of any plausible theory and has constantly urged me to explore new possibilities . Ordeals as those unwelcome possibilities were at the times he brought them up, they have constituted the framework of my thesis today. And I thank him for bringing out those ”impossible” possibilities and shedding light on me when I was in complete darkness. His door has always been open, and I enjoyed very much being his student.

Professor Thomas O’Neil has been a great influence in my research. His indisputable wisdom in combination with warm strength and genuine elegance have always made his comments profound and enlightening. When I started to think about statistical interpretation of the vortex crystals, he pointed out to me the importance of the incompressibility of Euler flow in the formation of the vortex crystals. This has been the key insight leading to the conclusions in my thesis.

I wish to express my gratitude to Professor Fred Driscoll for his tremendous help during my thesis work. He generously provided all of the computation power that I asked for, and solved numerous computer related problems for me. He also kindly endured my relentless abuse of the computers. Without his heart-warming support in every way, my research would have been impossible.

I have benefited greatly from the nonlinear dynamics and non-equilibrium statistics courses that I had with Professor Patrick Diamond. These classes have added many useful tools for analyzing the phenomena studied in this thesis. The study of the filamentation of vortex patch in chapter 2 was inspired in part by his lectures on shock waves. I also thank him for his advice on my career choices after graduate school.

As my thesis committee members, Professor Richard Salmon and Professor William Young provided many insightful comments that improved the quality of the thesis. I thank them for their time and expertise.

I thank Dr. Kevin Fine, Dr. Ann Cass, and Professor Fred Driscoll for having done the beautiful experiments on vortex crystals. They also kindly provided all of the experimental data for my analysis. Discussions with them have been very useful.

Dr. Francois Anderegg, David Schecter, Jason Kriesel, James Danielson, Eric Hollman and Terry Hilsabeck had made my daily life in the office and many trips to the APS meetings much more enjoyable. David, the most diligent person in the group and my sincere officemate for the past 4 years, also shared with me many thoughts on research and American culture. I also thank him for being such a good messenger whenever my wife calls unexpectedly. Jo Ann Christina provided friendly and prompt secretarial help.

The friendship with many people outside my work has often sustained and nurtured me over the years. In particular, I thank Edward Lever and his wife Alison, Alfred Liu, Christian Seberino and his wife Ann, Jason Fleischer, Yang-Sik Kim, Dong-Soo Shin, Bo Yang, Chuang Ren and his wife Yan-Hong Xu, Mr.Binkley and his family. I thank them for all their selfless help, generous love, and countless joyful moments that they brought me through the years. Our special friends Mr. Binkley and his family have provided me, on many occasions, unique American cultural experiences.

Finally, my deepest thanks goes to my wife Cheng-Ai Chi and my parents Chang-Xi and Rong-Zi Jin. Cheng-Ai has been more than a wonderful wife for me. She has been with me through all of the ups and downs in my graduate study, and has made sure that I did my best in my work. Despite her heavy load as a graduate student in the International Relationships and Pacific Study at UCSD and later as the China Marketing Manager in her company, she has done as much as possible to ensure me to stay focused on my study. Cheng-Ai has given my life balance and made the last five years happy ones. My parent have always encouraged me to get the best out of my life. Their faith in me has been a constant source of energy that has powered me through out my days as a student.

Part of chapter 1 has been published in Physical Review Letters, D. Z. Jin and D. H. E. Dubin, **80**, 4434 (1998). The thesis author was the primary investigator and single author of this paper.

VITA

February 13, 1967	Born, Tumen, Jilin Province, P.R. China
1985–1990	B.S., Tsinghua University, Beijing, P.R. China
1990–1992	Assistant Lecturer, Department of Physics Tsinghua University, Beijing, P.R. China
1992–1994	M.S., Tsinghua University, Beijing, P.R. China
1994–1995	Teaching Assistant, Department of Physics University of California, San Diego
1995–1999	Research Assistant, Department of Physics University of California, San Diego
1999	Doctor of Philosophy University of California, San Diego

PUBLICATIONS

"Regional maximum entropy theory of vortex crystal formation."
Physical Review Letters, **80**, 4434 (1998)

FIELDS OF STUDY

Major Field: Physics

Studies in Theoretical Mechanics.
Professors Donald R. Fredkin and Benjamin Grinstein

Studies in Mathematical Physics.
Professor Kim Griest

Studies in Advanced Classical Electrodynamics.
Professor Thomas M. O'Neil

Studies in Equilibrium Statistical Mechanics.
Professor Daniel H. E. Dubin

Studies in Quantum Mechanics.
Professor Roger F. Dashen

Studies in Plasma Physics.
Professor Daniel H. E. Dubin

Studies in Nonlinear and Nonequilibrium Dynamics of Physical Systems.
Professor Patrick H. Diamond

Studies in Nonneutral Plasmas.
Professor Thomas M. O'Neil

Studies in Renormalization in Field Theory, the Renormalization Group, and Critical Phenomena.
Professor Terence T. Hwa

Studies in Fluid Mechanics and Combustion.
Professor Yves Pomeau

Studies in Group Theoretical Methods in Physics.
Professor Aneesh V. Manohar

Studies in Advanced Solid-State Physics.
Professor Jorge E. Hirsch

ABSTRACT OF THE DISSERTATION

Theory of Vortex Crystal Formation
in Two-Dimensional Turbulence

by

Dezhe Jin
Doctor of Philosophy in Physics
University of California, San Diego, 1999
Professor Daniel H. E. Dubin, Chairman

Recent experiments with pure electron plasmas have found that freely relaxing turbulence in inviscid, incompressible, two-dimensional (2D) Euler flows can spontaneously form "vortex crystals" – symmetric, stable arrays of strong vortices (coherent patches of intense vorticity) that co-rotate with a background of low vorticity. This thesis presents a theory of these novel equilibrium states of 2D turbulence.

The thesis consists of three sections.

In the first section, we formulate a statistical theory of the vortex crystals. It is shown that the vortex crystals are well described as "regional" maximum fluid entropy (RMFE) states, which are equilibrium states reached through ergodic mixing of the background by the strong vortices. Given the dynamically conserved quantities of the Euler flow as well as the number of the strong vortices and the vorticity distributions within each strong vortex, the theory predicts the positions of the strong vortices and the coarse-grained vorticity distribution of the background. These predictions agree well with the observed vortex crystals.

In the second section, we study the dynamics of the interaction between the strong vortices and the background. A simple model of the strong vortex-background system is introduced. The model consists of several point vortices and a background with constant vorticity and nearly circular boundary. The total circulation of the point vortices is assumed to be small compared to that of the background. We show that the leading order dynamics of the the point vortices is equivalent to that of point vortices inside a circular free-slip boundary. However, this equivalence ends in finite time since nonlinear interactions cause the contour of the background to filament and wave break. The time required for the filamentation to occur is determined analytically, and compared to the contour dynamics simulation.

In the third section, we examine the formation process of the vortex crystals in more detail. In the first section, the vortex crystal equilibrium could only be predicted if the number of the strong vortices in the final state was given. In this section, a theory is advanced that allows us to predict from the initial conditions the approximate number N_c of the strong vortices in the final state. A relation is found between N_c and quantities associated with the flow in the early times of the turbulent relaxation, such as the number of the strong vortices, their total circulation, the area of the flow, and the exponents of the power laws associated with the strong vortices. This relation is confirmed by the experiments and vortex-in-cell simulations.

Chapter 1

General Introduction

In this thesis we present a theory for vortex crystal formation in the free relaxation of turbulence in inviscid, incompressible, two-dimensional (2D) Euler flows. In this chapter, we review briefly 2D Euler flow, 2D turbulence, and the experiments on vortex crystals. We also give an overview of the thesis.

1.1 Two-Dimensional Euler Flow

Two-dimensional Euler flows are the high-Reynolds-number limit of 2D incompressible Naiver-Stokes flows. They are often used as simple models for large scale geophysical and astrophysical flows, such as the polar vortex, tropical cyclones, and the Great Red Spot of Jupiter[1, 2, 3, 4, 5]. They are also applicable to many experimental systems[6], including strongly magnetized plasmas [39], thin layers of electrolyte[62], and flows in soap films[7].

The equation of motion for a 2D Euler flow is

$$\partial_t \omega + \mathbf{u} \cdot \nabla \omega = 0, \tag{1.1}$$

where $\mathbf{u}(\mathbf{r}, t)$ is the velocity field, and

$$\omega(\mathbf{r}, t) = \hat{\mathbf{z}} \cdot \nabla \times \mathbf{u} \tag{1.2}$$

is the vorticity field. Here $\hat{\mathbf{z}}$ is the unit vector perpendicular to the plane of the flow, and $\mathbf{r} = (x, y)$ is the position vector in the plane. The flow is incompressible:

$$\nabla \cdot \mathbf{u} = 0; \tag{1.3}$$

therefore, a stream function $\psi(\mathbf{r}, t)$ can be related to the velocity field:

$$\mathbf{u} = \nabla \times \psi \hat{\mathbf{z}}. \tag{1.4}$$

Substituting Eq.(1.4) into Eq.(1.2), we get

$$\nabla^2 \psi = -\omega. \tag{1.5}$$

Two-dimensional Euler flows can be unbounded, or bounded in domains of various shapes. When bounded, they can be subject to free-slip or periodic boundary conditions. In this thesis, we will focus on the flows bounded in a circular domain with the free-slip boundary condition:

$$\psi = 0, \quad \text{or} \quad \hat{\mathbf{n}} \cdot \mathbf{u} = 0 \quad \text{on the circular boundary,} \tag{1.6}$$

where $\hat{\mathbf{n}}$ denotes the radial unit vector of the circular domain.

From the above equations one can verify that the total circulation

$$\Gamma = \int d\mathbf{r}^2 \omega, \tag{1.7}$$

the total angular momentum,

$$L = -\frac{1}{2} \int d\mathbf{r}^2 \omega r^2, \tag{1.8}$$

and the total energy

$$H = \frac{1}{2} \int d\mathbf{r}^2 \omega \psi \tag{1.9}$$

of the flow are conserved.

Besides Γ, L and H, there are infinite number of conserved quantities in 2D Euler equations. For any closed path $C(t)$ moving with the flow in time t, and whose interior is contained in the fluid, the generalized enstrophy

$$Z = \int_{C(t)} d\mathbf{r}^2 f(\omega), \tag{1.10}$$

where f is an arbitrary function, is conserved by the flow since

$$\frac{d}{dt}\int_{C(t)} d\mathbf{r}^2 f(\omega) = \int_{C(t)} d\mathbf{r}^2 f'(\omega)\left(\partial_t\omega + \mathbf{u}\cdot\nabla\omega\right) = 0. \tag{1.11}$$

For the case that $f(\omega) = \omega^2$ and $C(t)$ is the boundary of the circular domain,

$$Z = \int d\mathbf{r}^2\omega^2 \equiv Z_2 \tag{1.12}$$

is called enstrophy.

1.2 The Free Relaxation of 2D turbulence

With the initial vorticity distribution and the boundary condition specified, the evolution of 2D Euler flow is completely determined by Eqs. (1.1)-(1.5). Except for a few cases, the evolution involves highly complicated velocity and vorticity fields. This is called the free relaxation of 2D turbulence. Note that Eq.(1.1) implies that vorticity is neither created nor destroyed, but is merely carried along the streamlines. The equation implicitly assumes that there are no external sources or sinks of vorticity, therefore describes freely relaxing turbulence rather than forced turbulence.

Over the years, both statistical and dynamical theories have been proposed to describe the free relaxation of 2D turbulence, and many numerical simulations and experiments have been performed to test them.

The statistical theory of 2D turbulence was initiated by Onsager[8], who considered the final state of relaxed turbulence in the inviscid limit. Onsager described 2D turbulence with the statistical mechanics of a finite number of point vortices. Observing that the statistics allows negative temperature solutions in which point vortices with same sign clump together, he suggested that this might offer an explanation for observations of large vortices in nature. Onsager's approach was further developed by Joyce and Montgomery[9]. Approximating the continuous vorticity field as the mean field of a large number of point vortices and assuming that the dynamics of the point vortices is ergodic, they predicted a relation between the stream function and the vorticity in the final state of the turbulent relaxation by maximizing the Boltzman entropy associated with the average density of the point vortices, under constraints that the total circulation, energy, and angular momentum (when the flow is unbounded or subject to circular free-slip boundary) are conserved. Numerical simulations performed in a square domain with periodic boundary conditions seems to agree with the theory[10, 11]. The theory has also been further developed by others[12]. However, the applicability of the point vortex statistics to 2D turbulence is limited, since the theory does not include the incompressibility of the Euler flow and hence can not include the conservation of the generalized enstrophy.

This issue was resolved by the works of Miller[13], Robert and Sommeria [14], who rediscovered the results of Lynden-Bell[15] and Kuz'min[16]. The theory distinguishes a microscopic state of the flow, which specifies the vorticity level at each spatial point, from a macroscopic state of the flow, which only specifies the coarse-grained (*i.e.* averaged over a small area) vorticity near each spatial point. A macroscopic state corresponds to many microscopic states; therefore, a fluid entropy can be associated with it. Assuming that 2D turbulent flow ergodically mixes the vorticity field, the theory predicts that the turbulence relaxes into a macroscopic state with maximum fluid entropy, with the constraints that not only the total circulation, energy, and angular momentum (when applicable), but also the generalize enstrophy, are conserved. The point vortex statistics is recovered when the coarse grained vorticity is much less than the (microscopic) vorticity levels[17]. However, the determination of the microscopic vorticity levels from any real experimental flow (which is necessarily coarse grained by the experimental diagnostics) is an outstanding issue. In this thesis, we call the theory as global maximum fluid entropy (GMFE) theory. We will discuss the theory in more detail in chapter 2. The GMFE theory has been applied to the statistical interpretation of the Jupiter's Great Red Spot[17, 18], merger of two vortices[19], and coherent vortical structures in domains of various shapes [20, 21, 22, 23, 24].

The dynamical description of the freely relaxing 2D turbulence originated from the work of Batchelor. Inspired by the success of Kolmogorov theory of three-dimensional homogeneous turbulence[2], Batchelor proposed a cascade theory for the freely relaxing 2D turbulence[25]. (Kraichnan proposed a similar theory for forced 2D homogeneous turbulence[26].) Observing that stretching of the constant vorticity lines increases the gradient of vorticity, Batchelor conjectured that the enstrophy is transfered towards find scales with nonzero rate in the inviscid limit of 2D turbulence. Through dimensional analysis he deduced that the enstrophy spectrum $|\omega(k,t)|^2$, where $\omega(k,t)$ is the spatial Fourier coefficient of the vorticity distribution, depends on the wave number k as k^{-1} for fine scales.

A logical consequence of the enstrophy cascade is that the coarse grained final state of the turbulent flow is a state of minimum enstrophy. Therefore, it should be possible to predict this structure from the initial condition by minimizing the enstrophy while keeping total circulation, energy, and angular momentum (when applicable) constant. This was pointed out by Bretherton and Haidvogel[27]. Matthaeus and Montgomery called this procedure "selective decay", and performed numerical simulations to verify it[28]. Leith used this procedure to describe isolated vortices[29]. Experiments done by Huang and Driscoll have shown that, from some initial conditions, observed final states are close to the minimum enstrophy states as predicted by the selective decay principle[30].

Many high resolution numerical simulations have been done to test the Batchelor-Kraichnan theory. Brachet *et al* observed in their simulations that stretching of the constant vorticity lines does create high vorticity gradients by forming vorticity filaments (or vorticity sheets). As these filaments are packed to form layers, the k^{-1} enstrophy spectrum is observed for small scales[31]. However, simulations by Santangelo, Benzi, and Legras, which are similar to those of Brachet *et al* but much longer in time, have revealed that the k^{-1} spectrum is only transient. Eventually the spectrum gets much steeper because of the formation of a large number of small scale coherent vortices as a consequence of the fragmentation of the vorticity filaments. They found that the long time behavior of the turbulent flow strongly depends on the initial conditions.

Numerical simulations also revealed that strong vortices (coherent patches of vorticity that are small in radius, intense in vorticity, and almost axially symmetric) can form from a large variety of initial conditions. These strong vortices are often formed around the maxima of the initial vorticity distribution, and they dominate the subsequent evolution of the turbulent flow[32, 33, 34]. Benzi *et al* also showed that the dynamics of the strong vortices can be understood in terms of the dynamics of point vortices[33]. Like sign strong vortices can merge when they come close to each other. The emergence of the strong vortices stops enstrophy cascade to small scales. Also, since the vorticity trapped in the strong vortices does not mix with the rest of the flow (except during mergers, when a small fraction of the circulation is torn away from the strong vortices via thin filaments), the ergodicity of the vorticity field is not fulfilled. Therefore, these simulations have shown that the evolution of 2D turbulence from a large variety of initial conditions can not be predicted from either Bachelor-Kraichnan theory (and its consequence – selective decay theory) or the GMFE theory.

To describe the flows dominated by strong vortices, Carnevale *et al* proposed a punctuated scaling theory, which states that the dynamics of the strong vortices can be thought of as the Hamiltonian dynamics of point vortices punctuated by occasional dissipative merger events[35]. Based on a merger model that conserves the energy of the strong vortices and the maximum vorticity of the flow, the theory proposes a power law decay of the number of the strong vortices, and predicts power law increase of the average radius and the average circulation of the strong vortices, as well as power law decay of the total circulation of the strong vortices. This power law decay of the number of the strong vortices is believed, with support of some numerical simulations, to lead to a single vortex or a pair of opposite-signed strong vortices in the final state of the turbulence[36]. Experiment with a thin layer of electrolyte have obtained results that agree well with the theory[37].

However, in recent experiments with pure electron plasmas, Fine *et al* have found that 2D turbulence can relax into strikingly ordered equilibrium states – "vortex crystals", in which a number of strong vortices arrange themselves into symmetric, stable arrays in a low vorticity background [38]. In the next section, these experiments are described in detail.

1.3 Experiments on Vortex Crystals

The experiments are performed on a strongly magnetized pure electron plasma column confined in a Penning-Malmberg trap, as shown in Fig. 1.1. Electrons emitted from a spiral tungsten filament are contained axially by the negative voltages on the two ends of the trap, and confined radially by a uniform axial magnetic field. Individual electrons bounce rapidly in the axial direction ($f_z \approx 0.4MHz$) , and have small cyclotron orbits ($\approx 5\mu m$) perpendicular to the magnetic field. The electric fields of the plasma cause the electron guiding centers to $\mathbf{E} \times \mathbf{B}$ drift across the magnetic field as effectively incompressible, inviscid, 2D Euler flow with free-slip boundary in a circular domain. The axially averaged electron density is proportional to the flow vorticity, and the axially averaged electrostatic potential of the plasma is proportional to the stream function. Since the plasma consists of only electrons, the flow has the somewhat unusual characteristic of having the same sign vorticity everywhere and non-zero total circulation. The vorticity of the flow is measured by dumping the plasma onto the phosphor screen and taking an image with a CCD camera [38, 39].

Two separate sequences of vorticity evolutions taken from the experiments are shown in Fig.1.2. The vorticity is initially distributed in a spiral, resembling the shape of the tungsten filament. Within one rotation time τ_R ($\approx 170\mu s$) of the flow, $50 \sim 100$ strong vortices form due to a Kelvin-Helmholtz instability. Subse-

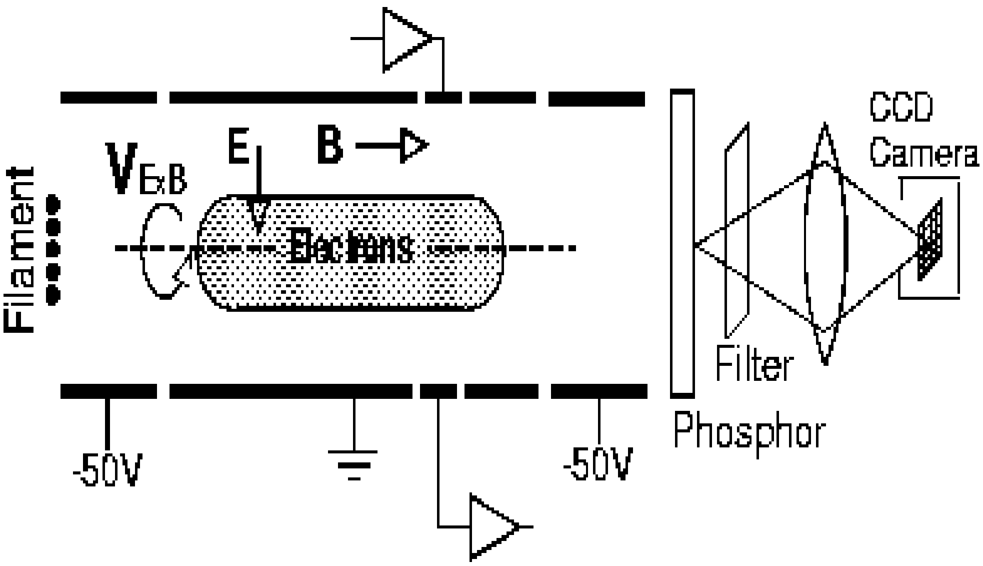

Figure 1.1: The Penning-Malmberg trap with phosphor screen/CCD camera diagnostics.

quently, the strong vortices move chaotically and merge occasionally, their number decreasing according to a power law as proposed in the punctuated scaling theory. A low vorticity background is generated from the thin filaments ejected during the mergers of the strong vortices and from the low vorticity part of the initial flow that becomes progressively more filamented and entangled. From some initial conditions, a single strong vortex is formed as the result of the vortex mergers, as shown in the top row of Fig.1.2. However, from slightly different initial conditions, $5 \sim 20$ strong vortices remain in the final states, as shown in the bottom row of Fig.1.2. Moreover, the strong vortices "cool" into symmetric lattice patterns that co-rotate with the background. These equilibria are called vortex crystals. The vortex crystals last over $10^4\tau_R$, until individual strong vortices are eroded away by non-ideal effects in the experiments that are not included in the 2D Euler equations, such as electron-electron collisions, electron-background neutral gas collisions, etc. Vortices with smaller radii and circulations are observed to be eroded away first.

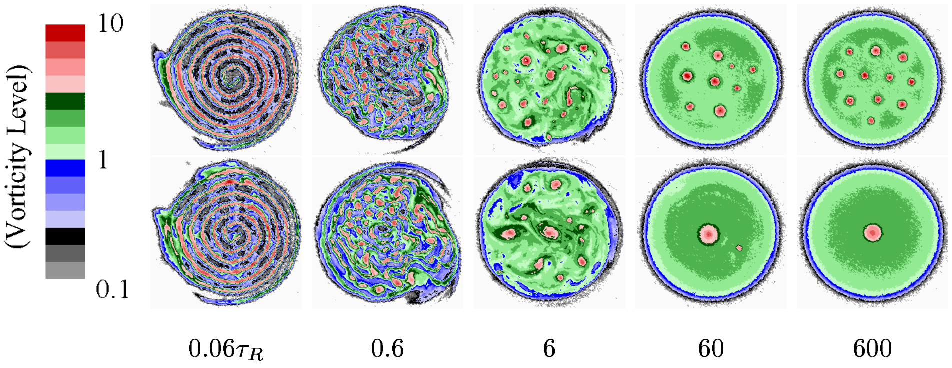

Figure 1.2: Images of vorticity at five different times for two sequences of turbulent relaxation from similar initial conditions. False color contour plots of vorticity are displayed.

The remaining strong vortices adjust into new equilibrium patterns. The time evolution of the number of the strong vortices for the two sequences presented in Fig.1.2 are shown in Fig.1.3. Also shown in the figure are the time evolutions of the total circulation of the strong vortices normalized with the circulation of the flow and the average radius of the strong vortices normalized with the radius of the circular boundary. For the sequence that forms no vortex crystal, the evolution of these quantities qualitatively agree with the punctuated scaling theory. For the sequence that forms vortex crystals,however, the agreement holds only for the early stage of the turbulent relaxation; at later times, the mergers are stopped and a finite number of the strong vortices are arrested into equilibrium patterns, and these quantities do not change much, until individual strong vortices are eroded away due to non-ideal effects.

1.4 Overview of the Thesis

The discovery of vortex crystals challenges both the global maximum fluid entropy theory and the punctuated scaling theory. The existence of isolated strong vortices clearly indicates that the flow is not globally ergodic, since the vorticity elements trapped in the strong vortices do not mix with the rest of the flow. The

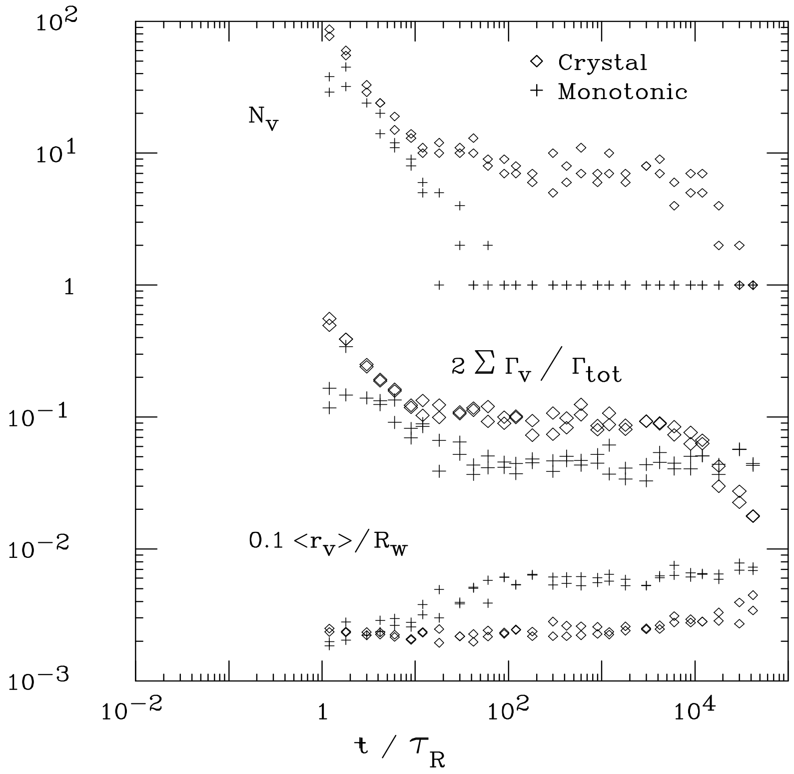

Figure 1.3: Evolution of number of vortices, vortex circulation, and average vortex size for two sequences of flow evolution.

global maximum fluid entropy theory predicts a smooth vorticity distribution[17], which leaves no room for the strong vortices. On the other hand, although the power law behaviors of the quantities associated with the strong vortices in the early stage of the flow evolution qualitatively agree with the punctuated scaling theory[38], the theory fails to explain why several strong vortices remain and fall into equilibrium patterns in the final state of the turbulent relaxation.

In this thesis, we propose that these two theories should work together to explain the formation of vortex crystals. The main idea is to recognize that some regions of the flow are well mixed, while other regions are not. The strong vortices ergodically mix the background to a state of maximum fluid entropy. This mixing, in return, perturbs the otherwise punctuated Hamiltonian dynamics of the strong vortices, cooling their chaotic motions and driving them into equilibrium positions. The strong vortices maintain themselves in the turbulent background flow, keeping their internal vorticity from mixing with the rest of the flow. Therefore, as in the punctuated scaling theory, the strong vortices can be treated as distinctive units that are dynamically preserved in between successive mergers.

This physical picture of vortex crystal formation is supported by the quantitative agreement between the observed vortex crystals and corresponding "regional" maximum fluid entropy (RMFE) states. A RMFE state differs from the global maximum entropy state by the inclusion of the strong vortices as additional dynamical constraints. To calculate the RMFE state corresponding to an observed vortex crystal, we first isolate the strong vortices and determine their number and the vorticity distributions in each of them. Then we obtain the total circulation, the total angular momentum, and the total energy of the flow. We also need to know the microscopic vorticity levels of the background flow; however, they can not be obtained from the observed flow since the measured vorticity is coarse-grained. We therefore assume that the microscopic vorticity of the background flow has a a single level, and infer its value from the observed flow. With these experimental inputs, the fluid entropy of the background is maximized via variational method using the technique of Lagrange multipliers. The maximization predicts the coarse-grained vorticity distribution of the background and the equilibrium positions of the strong vortices, which agree quite well with those of the corresponding vortex crystals. The RMFE theory of vortex crystals is presented in Chapter 2.

To understand the interaction between the strong vortices and the background, we study a simple model of vortex crystals. The strong vortices are modeled as point vortices, and the background as a vortex patch with constant vorticity and approximately circular boundary. In the limit that the total circulation of the point vortices is small compared to that of the background, the dynamics can be solved perturbatively with two time scale analysis. On the fast time scale, which is on the order of the rotation time of the vortex patch, the fast-time-averaged positions of the strong vortices do not change in the rotating frame of the vortex patch. The distortion of the boundary of the vortex patch consists of two parts: one is an "image charge" part, which is slaved by the fast-time-averaged positions of the point vortices, and the other is free-streaming Kelvin waves, which are the same as those on a circular vortex patch without the point vortices. The free-streaming Kelvin waves oscillate the point vortices around their fast-time-averaged positions. On the slow time scale, which involves many rotations of the vortex patch, the fast-time-averaged positions of the point vortices move in the rotating frame because of their mutual interactions and the influence of the image charge part of the vortex patch distortion. The resulting motions of the point vortices are the same as those of the point vortices inside a circular free-slip boundary, with the radius of the boundary equal to that of the vortex patch. The free-streaming Kelvin waves interact nonlinearly with the image charge part and the fast-time oscillations of the point vortices. This nonlinear interaction eventually causes filamentation and wave breaking of the Kelvin waves on the slow time scale. These predictions are compared to the contour dynamics simulations. The dynamics of this simple model of the vortex crystals is explained in Chapter 3.

Experimentally, slightly different initial conditions lead to vortex crystals with different numbers of strong vortices. For some initial conditions, no vortex crystal forms, as shown in the top row of Fig.1.2. It is important to know why this is so. From the vortex-in-cell simulations, we find that the number of the strong vortices N_c in the vortex crystals relates closely to the number N of the strong vortices in the early evolution of the turbulent flow. This relation can be expressed quantitatively by equating the mean time between merger events τ_m with the time scale τ_c of "cooling" the strong vortices into the equilibrium positions of the RMFE states. To merge, the strong vortices must come close to each other and their motions must be out of equilibrium and chaotic; therefore, if $\tau_c < \tau_m$, the mergers of the strong vortices stop since the strong vortices are arrested into equilibrium positions and the necessary condition for the merger is removed. We estimate τ_m from the power law decay of N that follows from the punctuated scaling theory. We estimate τ_c from the mixing time (inverse of the Lyapunov exponent) of the background, treating the background as passive scalars in the field of the strong vortices (weak background approximation). The prediction of N_c agrees with the results of the simulations and the experiments. The relation between N_c and the characteristics of the flow in the early stage of turbulent evolution is discussed in Chapter 4.

Chapter 2

Regional Maximum Fluid Entropy Theory of Vortex Crystal Formation

2.1 Introduction

In this chapter we show that vortex crystals are well described as regional maximum fluid entropy (RMFE) states. We derive the equations for RMFE states, discuss the zero temperature solutions, solve the finite temperature solutions numerically, and compare the predictions of RMFE states with the experiments.

2.2 Equations for RMFE states

2.2.1 Dynamical Constraints

As discussed in chapter 1, 2D turbulent flows conserve the total circulation Γ, angular momentum L, energy H, and the generalized enstrophy Z.

The conservation of Z can be conveniently parameterized in the following way[17]. For each real number σ, define $A(\sigma)$ as the area of the region of the flow on which $\omega < \sigma$. From the conservation of Z, Eqs.(1.10) and (1.11), it follows that the area of any curve moving with the flow is conserved. [1] Therefore, $A(\sigma)$ is conserved. Furthermore,

$$a(\sigma) = \frac{dA(\sigma)}{d\sigma} \tag{2.1}$$

is conserved. The quantity $a(\sigma)d\sigma$ is the area of the region of the flow on which $\sigma < \omega < \sigma + d\sigma$. The conservation of $a(\sigma)$ is equivalent to the conservation of Z[17].

From a large variety of initial conditions, many isolated strong vortices form [34, 33]. A strong vortex is a coherent patch of intense vorticity. It moves as a distinctive unit, and the vorticity distribution inside is often nearly axisymmetric and independent of time, until a close encounter with another strong vortex causes a merger[40]. Therefore, in between two consecutive mergers of the strong vortices, the number N and the vorticity distributions in each of them are additional (approximate) dynamical constraints on the 2D turbulent flow. We further assume that the vorticity distributions inside each strong vortices are described by axisymmetric functions $\zeta_i(|\mathbf{r} - \mathbf{R}_i|)$, where $\mathbf{R}_i, i = 1, ..., N$ are the positions of the strong vortices.

2.2.2 Fluid Entropy

During the formation of the vortex crystals, the background flow is mixed in an intricate way by the strong vortices and the random vorticity fluctuations of the background. This causes chaotic transport and complicated distribution of the microscopic vorticity field of the flow.

A microscopic state of the background flow is a particular distribution of the microscopic vorticity. Introducing a uniform grid with a microscopic grid size Δ, a microscopic state is specified by assigning appropriate vorticity level on each unit cell. The accuracy of this description is guaranteed as along as $\Delta \to 0$.

However, description of the chaotic background flow down to the micro-

---

[1] Take $f(\omega) = 1$ in Eq.(1.11).

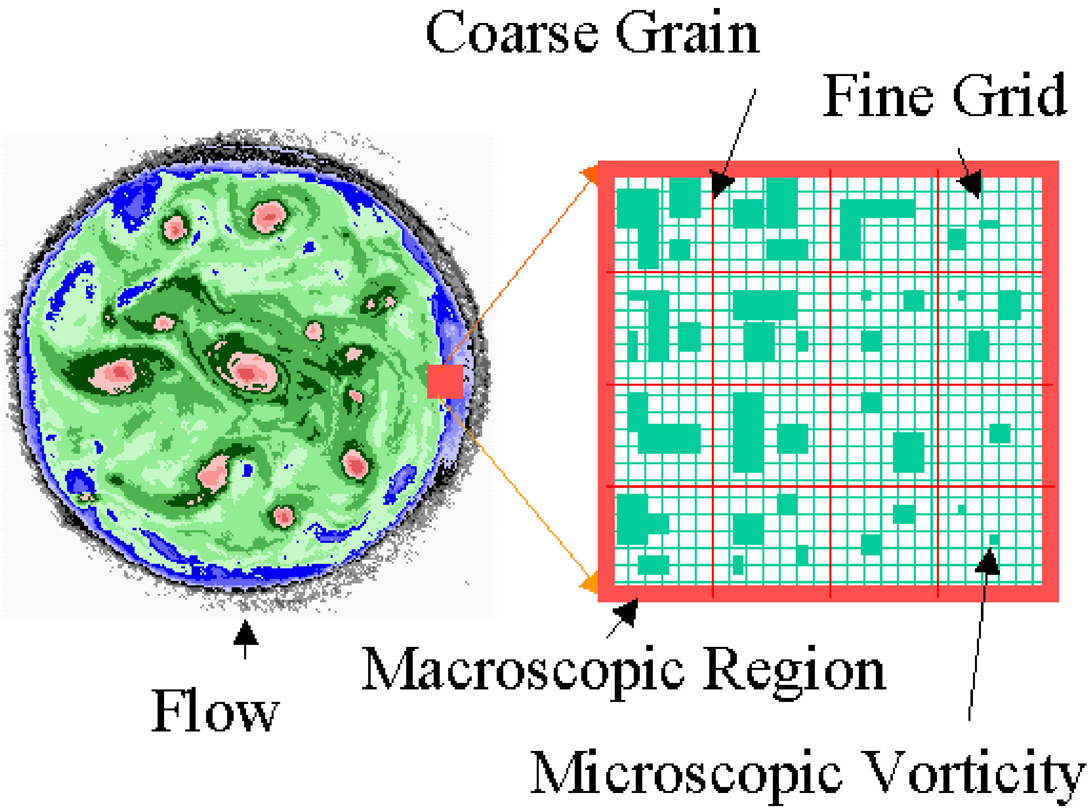

Figure 2.1: Illustration of macroscopic and microscopic descriptions of 2D turbulent flow.

scopic scales is not necessary since only the large scale structure, or the macroscopic state of the flow, is of concern. To determine the macroscopic state corresponding to a microscopic state, we sub-divide the uniform grid into a union of coarse grains of macroscopic sizes, and obtain the coarse-grained distribution function $n(\mathbf{r},\sigma)$ of the background (see Fig.2.1). Here, $n(\mathbf{r},\sigma)d\sigma$ is equal to the number of the unit cells of the coarse grain at $\mathbf{r}$ assigned to vorticity level in the interval $(\sigma, \sigma + d\sigma)$, divided by the total number of the unit cells in the coarse grain. Obviously,

$$\mathcal{N} = \int d\sigma n(\mathbf{r},\sigma) = 1, \tag{2.2}$$

and

$$a(\sigma) = \int d\mathbf{r}^2 n(\mathbf{r},\sigma). \tag{2.3}$$

A macroscopic state of the background specified by the distribution functions $n(\mathbf{r}, \sigma)$ corresponds to a large number $W[n(\mathbf{r}, \sigma)]$ of the microscopic states. Therefore, a fluid entropy of the background can be defined as

$$S[n(\mathbf{r}, \sigma)] = k_B \ln W, \tag{2.4}$$

where k_B is the Boltzman constant.

The number $W[n(\mathbf{r}, \sigma)]$ can be calculated in a combinatorial way. Consider the coarse grain at $\mathbf{r}$ with an area $d\mathbf{r}^2$. The number of the unit cells in this coarse grain is

$$N_{uc} = \frac{d\mathbf{r}^2}{\Delta^2}, \tag{2.5}$$

and the number of the cells assigned to the vorticity level $\sigma \sim \sigma + d\sigma$ is

$$N_\sigma = n(\mathbf{r}, \sigma) d\sigma N_{uc}. \tag{2.6}$$

Permutations of the assignments within the coarse grain does not change the distribution function, or the macroscopic state. Since the number of permutations within the coarse grains is

$$\frac{N_{uc}!}{\prod_\sigma N_\sigma!}, \tag{2.7}$$

the total number of the permutations in all of the coarse grains is

$$W = \prod_{\mathbf{r}} \left(\frac{N_{uc}!}{\prod_\sigma N_\sigma!} \right), \tag{2.8}$$

and therefore, the fluid entropy is

$$S = k_B \sum_{\mathbf{r}} \left(\ln N_{uc}! - \sum_\sigma \ln N_\sigma! \right), \tag{2.9}$$

according to Eq.(2.4). Since the coarse grains are macroscopic in size, we have

$$N_{uc} \gg 1, \quad N_\sigma \gg 1, \tag{2.10}$$

hence the Stirling formula is applicable:

$$\begin{aligned} \ln N_{uc}! &= N_{uc} \ln N_{uc}, & (2.11) \\ \ln N_\sigma! &= N_\sigma \ln N_\sigma. & (2.12) \end{aligned}$$

Substituting above equations into Eq.(2.9), we obtain, after throwing away an unimportant constant,

$$S = -\frac{k_B}{\Delta^2} \int d\mathbf{r}^2 \int d\sigma n(\mathbf{r},\sigma) \ln n(\mathbf{r},\sigma), \tag{2.13}$$

where we have used

$$\sum_{\mathbf{r}} d\mathbf{r}^2 \to \int d\mathbf{r}^2, \quad \sum_{\sigma} d\sigma \to \int d\sigma, \tag{2.14}$$

as well as Eqs.(2.2), (2.5) and (2.6). For other derivations and more detailed explanations of the fluid entropy, see Ref. [13, 14, 17].

2.2.3 RMFE States

During the formation of the vortex crystals, the background vorticity is chaotically mixed. If we assume that the mixing is ergodic, *i.e.* the flow has equal probability of going into any one of the microscopic states that are dynamically accessible, the flow will relax into the macroscopic state that has the maximal number of corresponding microscopic states – the maximum fluid entropy state of the background, or "regional" maximum fluid entropy (RMFE) state. The RMFE state is distinguished from the global maximum fluid entropy (GMFE) state in that only part of the flow, the background, is ergodically mixed.

As discussed previously, the microscopic states of the flow conserve the total circulation Γ, the total angular momentum L, the total energy H, the total area $a(\sigma)d\sigma$ of the region with vorticity in the interval $(\sigma, \sigma + d\sigma)$, as well as the number N of the strong vortices and the vorticity distributions $\zeta_i(|\mathbf{r} - \mathbf{R}_i|)$ in each of them. Accordingly, the distribution function $n(\mathbf{r},\sigma)$ that defines the macroscopic states of the background is subject to a number of constraints.

The conservation of the $a(\sigma)$ is expressed by Eq.(2.3). The constraints provided by the strong vortices can be put in the following forms:

$$\Phi_i = \int d\mathbf{r}^2 n(\mathbf{r},\sigma) \phi_i(\mathbf{r} - \mathbf{R}_i) = 0, \quad i = 1, ..., N \tag{2.15}$$

where the auxiliary fields ϕ_i are defined as

$$\phi_i(\mathbf{r}-\mathbf{R}_i) = \begin{cases} \infty & , \text{ if } \mathbf{r} \text{ is inside the } i\text{-th strong vortex}, \\ 0 & , \text{ otherwise.} \end{cases} \tag{2.16}$$

Eq.(2.15) guarantees that the background vorticity is zero inside the strong vortices. Therefore, the coarse-grained vorticity field of the whole flow is

$$\bar{\omega}(\mathbf{r}) = \begin{cases} \zeta_i(|\mathbf{r}-\mathbf{R}_i|) & , \text{ if } \mathbf{r} \text{ is inside the } i\text{-th strong vortex}, \\ \int d\sigma\sigma n(\mathbf{r},\sigma) & , \text{ if } \mathbf{r} \text{ is inside the background.} \end{cases} \tag{2.17}$$

The coarse-grained vorticity distribution $\bar{\omega}$ is the link between $n(\mathbf{r},\sigma)$ of the background and conservations of Γ, L, and H. Replacing the vorticity distribution ω in Eqs.(1.7), (1.8), and (1.9) with the coarse-grained vorticity $\bar{\omega}$, we obtain

$$\Gamma = \int d\mathbf{r}^2\bar{\omega}, \tag{2.18}$$

$$L = -\frac{1}{2}\int d\mathbf{r}^2\bar{\omega}r^2, \tag{2.19}$$

and

$$H = \frac{1}{2}\int d\mathbf{r}^2\bar{\omega}\bar{\psi}, \tag{2.20}$$

where

$$\nabla^2\bar{\psi} = -\bar{\omega}. \tag{2.21}$$

This replacement is justified since Γ and L depend linearly on the vorticity, and H depends on long range interactions between the vorticity fields. In addition to the constraints above, $n(\mathbf{r},\sigma)$ has to satisfy the normalization condition, Eq.(2.2).

To obtain the RMFE state under the constraints, we use the variational method with the Lagrange multipliers. The independent variables in the variation are the distribution function $n(\mathbf{r},\sigma)$ and the positions of the strong vortices $\mathbf{R}_i, i = 1, ..., N$. The constrained maximization of the fluid entropy of the background is done by the unconstrained maximization of the functional S', defined as

$$\begin{aligned} S' = S \quad &- \quad \frac{1}{T}\Big[(H-H_0) - \Omega(L-L_0) + \mu(\Gamma-\Gamma_0) \\ &+ \quad \int d\sigma\gamma(\sigma)\,(a(\sigma)-a_0(\sigma)) + \sum_i \int d\sigma\alpha_i(\sigma)(\Phi_i - 0) \\ &+ \quad \int d\mathbf{r}^2\kappa(\mathbf{r})(\mathcal{N}-1)\Big], \end{aligned} \tag{2.22}$$

where $T, \Omega, \mu, \gamma(\sigma), \alpha_i(\sigma)$, and $\kappa(\mathbf{r})$ are Lagrange multipliers, and Γ_0, L_0, H_0, and $a_0(\sigma)$ are values of the conserved quantities Γ, L, H, and $a(\sigma)$, respectively.

Variation of S' with respect to $n(\mathbf{r}, \sigma)$ gives

$$\begin{aligned} \delta S' = & - \int d\mathbf{r}^2 \int d\sigma \delta n \Bigg\{ \frac{k_B}{\Delta^2} (1 + \ln n) + \frac{1}{T} \Big[\bar{\psi}\sigma + \frac{1}{2}\Omega r^2 \sigma + \mu\sigma \\ & + \gamma(\sigma) + \sum_i \alpha_i(\sigma)\phi_i + \kappa(\mathbf{r}) \Big] \Bigg\}. \end{aligned} \tag{2.23}$$

At the maximum of S', we have $\delta S' = 0$ for arbitrary δn, therefore,

$$n(\mathbf{r}, \sigma) = n_0(\mathbf{r}) \exp\left[-\beta \left(\sigma\psi_c(\mathbf{r}) + \gamma(\sigma) + \sum_i \alpha_i(\sigma)\phi_i(\mathbf{r}) \right) \right], \tag{2.24}$$

where

$$\psi_c(\mathbf{r}) \equiv \bar{\psi}(\mathbf{r}) + \frac{1}{2}\Omega r^2 \tag{2.25}$$

is the coarse-grained stream function in the rotating frame of angular frequency Ω,

$$\beta \equiv \frac{\Delta^2}{k_B T} \tag{2.26}$$

is the renormalized inverse temperature, [2] and

$$n_0(\mathbf{r}) \equiv e^{-1-\beta\kappa(\mathbf{r})} \tag{2.27}$$

is the normalization factor. Together with the auxiliary functions ϕ_i, the Lagrange multipliers $\alpha_i(\sigma)$, which can be any number that is same sign as β, merely ensure that the background is excluded from the regions of the strong vortices. With the understanding that $n(\mathbf{r}, \sigma) = 0$ inside the regions of the strong vortices, we shall from now on omit $\sum_i \alpha_i(\sigma)\phi_i$ in the expression of $n(\mathbf{r}, \sigma)$ for convenience.

Using the normalization condition, Eq.(2.2), we obtain

$$n_0(\mathbf{r}) = \frac{1}{\int d\sigma \exp\left[-\beta\left(\sigma\psi_c + \gamma(\sigma)\right)\right]}. \tag{2.28}$$

Therefore, Eq.(2.24) becomes

$$n(\mathbf{r}, \sigma) = \frac{\exp\left[-\beta\left(\sigma\psi_c + \gamma(\sigma)\right)\right]}{\int d\sigma \exp\left[-\beta\left(\sigma\psi_c + \gamma(\sigma)\right)\right]}. \tag{2.29}$$

---

[2] Although in principle the temperature can be positive or negative, in this work only positive temperature is considered.

The Lagrange multipliers β, Ω, μ, and $\gamma(\sigma)$ can be determined indirectly from H_0, L_0, Γ_0, and $a_0(\sigma)$.

Since in Eq.(2.22) only H and L change as $\mathbf{R}_i$ change, maximization of S' with respect to the positions of the strong vortices yields

$$\frac{\partial S'}{\partial \mathbf{R}_i} = -\frac{1}{T}\frac{\partial}{\partial \mathbf{R}_i}(H - \Omega L) = 0, \tag{2.30}$$

or

$$\frac{\partial}{\partial \mathbf{R}_i}(H - \Omega L) = 0. \tag{2.31}$$

Furthermore, since $H - \Omega L$ is the total energy of the flow in the rotating frame of angular velocity Ω, the above equations are equivalent to the requirement that the strong vortices are in equilibrium positions in the rotating frame, *i.e.*, their velocities are zero in the rotating frame.

Equations (2.29) and (2.31) are necessary conditions for the RMFE states. However, to ensure that a solution of these equations is indeed at least a local maximum of the fluid entropy of the background, the stability of the solution must be checked. This is done in two steps. First we show that, for given positions of the strong vortices, the distribution function given by Eq.(2.29) maximizes S', and hence S under the constraints. To do this, we take the second variation of S' with respect to $n(\mathbf{r}, \sigma)$:

$$\begin{aligned} \delta^{(2)} S' &= -\int d\mathbf{r}^2 \int d\sigma \left[\frac{k_B}{\Delta^2}\frac{\delta n^2}{n} + \frac{1}{T}\sigma \delta n \delta\bar{\psi}\right] \\ &= -\int d\mathbf{r}^2 \int d\sigma \frac{k_B}{\Delta^2}\frac{\delta n^2}{n} - \frac{1}{T}\int d\mathbf{r}^2 \delta\bar{\omega}\delta\bar{\psi} \\ &= -\int d\mathbf{r}^2 \int d\sigma \frac{k_B}{\Delta^2}\frac{\delta n^2}{n} - \frac{1}{T}\int d\mathbf{r}^2 \left(\nabla\delta\bar{\psi}\right)^2 \\ &< 0. \end{aligned} \tag{2.32}$$

In the last step of the derivation above, we have used

$$\nabla^2 \delta\bar{\psi} = -\delta\bar{\omega}, \quad \text{and} \quad \delta\bar{\psi} = 0 \quad \text{on} \quad \partial D, \tag{2.33}$$

which follow Eq.(2.21) and the free-slip boundary condition. Obviously, S' is a concave functional of $n(\mathbf{r}, \sigma)$; therefore, the stationary point given by Eq.(2.29) is also the maximum point of S'. Second, we calculate S for given positions of the strong vortices with the background given by Eq.(2.29), and obtain S as a function of the positions of the strong vortices, $S(\{\mathbf{R}_i\})$. To ensure that the equilibrium positions given by Eqs.(2.31) indeed maximize S, we calculate the Jacobian

$$J = \left(\frac{\partial^2 S}{\partial \mathbf{R}_i \partial \mathbf{R}_j} \right)_{ij} \tag{2.34}$$

at the equilibrium positions. If all of the eigenvalues of the matrix J are non-positive, the equilibrium positions maximize S.

An observed vorticity field of a flow is necessarily coarse grained. Therefore, it is impossible to obtain the conserved quantity $a(\sigma)$ from the observed vorticity field. Different forms of $a(\sigma)$ can correspond to the same coarse grained vorticity distribution. For example, consider

$$a(\sigma) = (A - \Gamma/\omega_f)\delta(\sigma) + \Gamma/\omega_f \delta(\sigma - \omega_f), \tag{2.35}$$

where A is the area of the circular domain and ω_f is a positive number. This corresponds to a flow whose microscopic vorticity has only single value ω_f and total area Γ/ω_f. For any value of ω_f that is greater than the maximum of an observed vorticity distribution, there is a way of distributing the microscopic vorticity with vorticity level ω_f and total area Γ/ω_f which, when coarse grained, gives the observed vorticity distribution. [3]

The difficulty of obtaining $a(\sigma)$ from the observed vorticity distribution limits the predicting power of the maximum fluid entropy theory. For the theory to be useful, assumptions about the form of $a(\sigma)$ must be supplied. In this work, we assume that the microscopic vorticity of the background has only single value ω_f, which is the simplest assumption one can make. The value of ω_f is chosen from physical considerations (see section 2.5.2).

With the simple assumption about $a(\sigma)$, the background of the RMFE

---

[3] Here we assume that the flow has single sign (taken as positive) of vorticity, which is true for the experimental flows discussed in this work.

state is given by the Fermi distribution of the coarse-grained vorticity:

$$\bar{\omega}(\mathbf{r}) = \frac{\omega_f}{\exp[\beta \omega_f \psi_c] + 1}, \tag{2.36}$$

which is derived from Eqs.(2.29) and (2.17) for this simple case. Here

$$\psi_c \equiv \bar{\psi} + \frac{1}{2}\Omega r^2 - \mu. \tag{2.37}$$

2.3 Zero Temperature Solutions

Equations for the RMFE states contain solutions similar to the observed vortex crystals. This can be illustrated for the case of zero temperature, *i.e.* $\beta \to \infty$. To simplify the analysis, we assume that the strong vortices can be treated as point vortices with circulations $\Gamma_i, i = 1, ..., N$. We also assume that the radius of the circular boundary is much larger than the size of the flow so that we can neglect the influence of the boundary and think of the flow as being placed in the free space.

From Eq.(2.36), we see that there are two possibilities for getting nonzero background vorticity distribution for $\beta \to \infty$. One possibility is $\psi_c = 0$ inside the background, and $\psi_c > 0$ outside. In this case, since $\beta\psi_c$ is undetermined in the background, $\bar{\omega}$ can take any constant value that is less than ω_f. The microscopic vorticity fields are uniformly mixed with the void, and the velocity of the background flow is zero in the rotating frame of angular frequency Ω. We call this possibility a shear-free equilibrium. The other possibility is $\psi_c = 0$ only on the boundaries of the background. Inside the background, $\psi_c < 0$, outside, $\psi_c > 0$. In this case, $\bar{\omega} = \omega_f$ inside the background, and the microscopic vorticity fields are all clustered together. We call this possibility a Fermi degenerate equilibrium.

2.3.1 Shear-Free Equilibrium

For shear-free equilibrium, the solution of the equations for the RMFE state is easily found. The coarse-grained vorticity of the background can be any positive number $\omega_0 < \omega_f$. The outer boundary of the background is a circle with radius

$$\rho_0 = \sqrt{\frac{\Gamma}{\pi\omega_0}}. \tag{2.38}$$

Around each strong vortex, there is a circular hole with radius

$$\rho_i = \sqrt{\frac{\Gamma_i}{\pi\omega_0}}. \tag{2.39}$$

Here, ρ_i is chosen such that, if the circulation of the strong vortex is uniformly distributed in the circular hole, the vorticity will be ω_0. The strong vortex sits on the center of the hole. The hole shields the influence of the strong vortex. This can be understood by thinking of the hole as filled with vorticity ω_0 and $-\omega_0$. The circulation of the negative vorticity in the hole is $-\Gamma_i$. At a point in the background, the stream function due to the strong vortex and that due to the negative vorticity filled cancel each other because of the symmetry. The net stream function of the hole-strong vortex system is hence due to the positive vorticity filled. Therefore, the stream function inside the background is the same as that of a uniform circular vortex patch without the strong vortices and the holes, which is

$$\bar{\psi} = -\frac{1}{4}\omega_0 r^2. \tag{2.40}$$

From $\psi_c = 0$ we obtain

$$\Omega = \frac{\omega_0}{2} \tag{2.41}$$

and

$$\mu = 0 \tag{2.42}$$

in the background.

Since the strong vortices are shielded and the background flow is at rest in the rotating frame, the velocities of the strong vortices are zero as long as their shielding holes do not overlap. Therefore, no unique patterns for the strong vortices are required to satisfy Eq.(2.31) for the positions of the strong vortices. Shear-free equilibrium does not require solutions similar to the vortex crystals.

2.3.2 Fermi-Degenerate Equilibrium

The Fermi-degenerate solution requires $\Omega > \frac{1}{2}\omega_f$. Equation (2.37) yields

$$\nabla^2\psi_c = \nabla^2\bar{\psi} + 2\Omega = -\omega_f + 2\Omega, \tag{2.43}$$

in which we have used Eqs.(2.21) and $\bar{\omega}(\mathbf{r}) = \omega_f$. Therefore,

$$(-\omega_f + 2\Omega)A_{D_b} = \int_{D_b} d\mathbf{r}^2\nabla^2\psi_c = \oint_{\partial D_b} d\ell\hat{\mathbf{n}}\cdot\nabla\psi_c, \tag{2.44}$$

where D_b is the domain occupied by the background, ∂D_b its boundary, A_{D_b} its area, and $\hat{\mathbf{n}}$ the unit vector normal to ∂D_b and pointing out of D_b. Since $\psi_c > 0$ outside the background and $\psi_c < 0$ inside,

$$\hat{\mathbf{n}}\cdot\nabla\psi_c > 0. \tag{2.45}$$

Therefore

$$(-\omega_f + 2\Omega)A_{D_b} > 0, \tag{2.46}$$

i.e.

$$\Omega > \frac{1}{2}\omega_f. \tag{2.47}$$

Near a strong vortex, which we approximate as a point vortex, $\psi_c \to \infty$; therefore, $\bar{\omega} = 0$ near the strong vortex, *i.e.* there is a shielding hole around it. However, unlike the shear-free equilibrium, the radius of the hole is smaller than that required by complete shielding. The argument is as follows.

Denote $D_{h,i}$ as the domain of the hole around the i-th strong vortex, $\partial D_{h,i}$ as its boundary, $A_{D_{h,i}}$ as its area, and $\hat{\mathbf{n}}_i$ as the unit vector perpendicular to $\partial D_{h,i}$ and pointing out of $D_{h,i}$. Then in $D_{h,i}$,

$$\nabla^2\psi_c = \nabla^2\bar{\psi} + 2\Omega = -\Gamma_i\delta(\mathbf{r} - \mathbf{R}_i) + 2\Omega, \tag{2.48}$$

and

$$-\Gamma_i + 2\Omega A_{D_{h,i}} = \int_{D_{h,i}} d\mathbf{r}^2\nabla^2\psi_c = \oint_{\partial D_b} d\ell\hat{\mathbf{n}}_i\cdot\nabla\psi_c. \tag{2.49}$$

Since $\psi_c > 0$ in the hole and $\psi_c < 0$ in the background,

$$\hat{\mathbf{n}}_i \cdot \nabla \psi_c < 0. \tag{2.50}$$

Therefore,

$$-\Gamma_i + 2\Omega A_{D_{h,i}} < 0, \tag{2.51}$$

and

$$\Gamma_i - \omega_f A_{D_{h,i}} > \Gamma_i - 2\Omega A_{D_{h,i}} > 0, \tag{2.52}$$

where Eq.(2.47) is used. If we assume that the hole is approximately circular with radius ρ_i, then from above equation we get

$$\rho_i < \sqrt{\frac{\Gamma_i}{2\pi\Omega}} < \sqrt{\frac{\Gamma_i}{\pi\omega_f}}. \tag{2.53}$$

In other words, ρ_i is smaller than that required for complete shielding of the strong vortex, the rightmost quantity in the equality above.

To calculate the stream function due to the hole-strong vortex system, we again think of the hole as filled with vorticity ω_f and $-\omega_f$. At a point in the background, the net stream function due to the strong vortex and the negative vorticity filled will be that of a point vortex with circulation

$$\Gamma_i^{'} = \Gamma_i - \pi\rho_i^2\omega_f, \tag{2.54}$$

provided that the hole is approximately circular. The positive vorticity filled can be combined with the background. Therefore, the stream function at any point in the background is due to the background with constant vorticity ω_f (no holes) and point vortices with circulations $\Gamma_i^{'}, i = 1, ..., N$.

Since the strong vortices are only partially shielded, they must take nontrivial positions to satisfy Eq.(2.31). We can estimate the scale d of the distance between the strong vortices when $\Gamma_i^{'}, i = 1, ..., N$, are much smaller than the circulation of the background. In this case, the outer boundary of the background is distorted only slightly from the circle, and the stream function due to the background without holes is approximately given by

$$\bar{\psi} \approx -\frac{1}{4}\omega_f r^2. \tag{2.55}$$

Therefore, in the rotating frame, ψ_c at a strong vortex is of order

$$\psi_c \sim \left(\frac{1}{2}\Omega - \frac{1}{4}\omega_f\right) d^2 - \frac{\Gamma'}{2\pi} \ln d, \tag{2.56}$$

where Γ' is a typical value of $\Gamma'_i, i = 1, ..., N$. Since the velocity of the strong vortex must be zero in the rotating frame, we have

$$\frac{\partial \psi_c}{\partial d} \sim \left(\Omega - \frac{1}{2}\omega_f\right) d - \frac{\Gamma'}{2\pi d} \sim 0, \tag{2.57}$$

therefore,

$$d \sim \sqrt{\frac{\Gamma'}{\pi\left(2\Omega - \omega_f\right)}}. \tag{2.58}$$

The details of the Fermi-degenerate solution can be worked out for the case of Γ' much smaller than the total circulation of the background. The outer contour of the background is described by a function

$$\rho(\theta) = \rho_0 + \delta\rho(\theta), \tag{2.59}$$

where ρ_0 is the radius of the unperturbed circular contour, and $\delta\rho(\theta)$ is the small deviation. The stream function of the background can be thought of as composed of the stream function of the unperturbed circular patch,

$$\bar{\psi}_0 = \begin{cases} -\frac{1}{4}\omega_f r^2 & , \quad r < r_0, \\ \frac{1}{4}\omega_f r_0^2 - \frac{1}{2}\omega_f r_0^2 \ln\left(\frac{r}{r_0}\right) & , \quad r \geq r_0, \end{cases} \tag{2.60}$$

and the correction $\delta\bar{\psi}$ due to the distortion. On the outer boundary of the background, the stream function in the rotating frame is

$$\psi_c(\rho, \theta) = \bar{\psi}_0(\rho_0 + \delta\rho, \theta) + \delta\bar{\psi} + \bar{\psi}_v(\rho_0 + \delta\rho, \theta) + \frac{1}{2}\Omega(\rho_0 + \delta\rho)^2 - \mu = 0, \tag{2.61}$$

where $\bar{\psi}_v$ is the stream function due to the point vortices with effective circulations Γ'_i. Correct to the order of Γ',

$$\bar{\psi}_0(\rho_0 + \delta\rho, \theta) \approx -\frac{1}{4}\omega_f \rho_0^2 - \frac{1}{2}\omega_f \rho_0 \delta\rho, \tag{2.62}$$

$$\delta\bar{\psi}(\rho_0 + \delta\rho, \theta) \approx \delta\bar{\psi}(\rho_0, \theta), \tag{2.63}$$

$$\bar{\psi}_v(\rho_0 + \delta\rho, \theta) \approx \bar{\psi}_v(\rho_0, \theta), \tag{2.64}$$

and

$$\frac{1}{2}\Omega(\rho_0 + \delta\rho)^2 \approx \frac{1}{2}\Omega\rho_0^2 + \Omega\rho_0\delta\rho. \tag{2.65}$$

Therefore, Eq.(2.61) becomes

$$\delta\bar{\psi}(\rho_0, \theta) + \bar{\psi}_v(\rho_0, \theta) + \left(\Omega - \frac{1}{2}\omega_f\right)\rho_0\delta\rho \approx \mu + \frac{1}{4}(\omega_f - 2\Omega)\rho_0^2. \tag{2.66}$$

From Eq.(2.57) we know that

$$\Omega - \frac{1}{2}\omega_f \sim \frac{\Gamma'}{2\pi d^2}, \tag{2.67}$$

hence

$$\left(\Omega - \frac{1}{2}\omega_f\right)\rho_0\delta\rho \sim \frac{\Gamma'\rho_0\delta\rho}{2\pi d^2} \tag{2.68}$$

is in fact of order ${\Gamma'}^2$. Therefore, we have

$$\delta\bar{\psi}(\rho_0, \theta) + \bar{\psi}_v(\rho_0, \theta) = 0 \tag{2.69}$$

correct to the order of Γ'. Here we have taken

$$\mu = \frac{1}{4}(2\Omega_f - \omega_f)\rho_0^2. \tag{2.70}$$

Equation (2.69) shows that the stream function $\delta\bar{\psi}$ due to the deformation of the background from the circular shape is the same as that due to the image charges of the point vortices with effective circulations $\Gamma_i', i = 1, ..., N$. The stream function inside the background, therefore, is the same as that of the classical problem of point vortices inside a circular boundary of radius ρ_0 with free-slip boundary:

$$\begin{aligned} \bar{\psi}(\mathbf{r}) &= \bar{\psi}_0 + \delta\bar{\psi} + \bar{\psi}_v \\ &= -\frac{1}{4}\omega_f r^2 + \sum_{i=1,N}\frac{\Gamma_i'}{2\pi}\ln\left(\frac{\rho_0^4 + r^2R_i^2 - 2\rho_0^2 rR_i\cos\Theta_i}{\rho_0^2\left(r^2 + R_i^2 - 2rR_i\cos\Theta_i\right)}\right), \end{aligned} \tag{2.71}$$

where Θ_i is the angle between $\mathbf{r}$ and $\mathbf{R}_i$. Consequently, the equilibrium positions of the strong vortices in the rotating frame is the same as the equilibrium positions of the point vortices in the classical problem, which has been investigated by

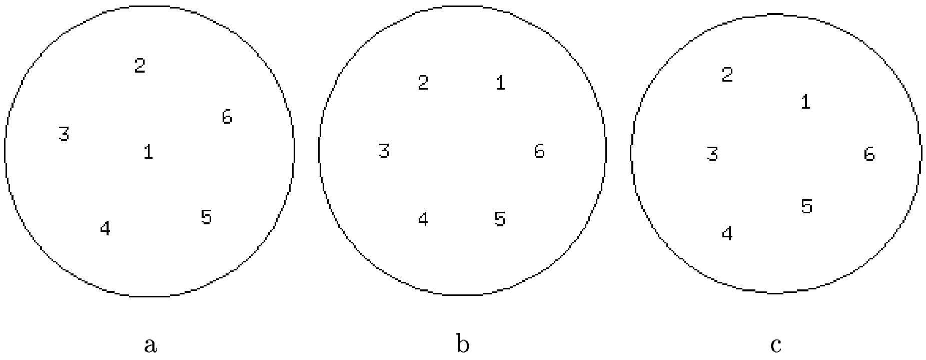

Figure 2.2: Equilibrium patterns of six point vortices of the same circulations. The triangular pattern (c), which is not previously discovered, comes from the deformation of the hexagonal pattern (b) when it becomes unstable.

Havelock[46], Campbell and Ziff[47], and others. When the point vortices all have the same circulations, the equilibrium patterns are symmetric, as shown in Fig.2.2, and are quite similar to the observed patterns of the vortex crystals. Therefore, the Fermi-degenerate solutions of the RMFE states are similar to the vortex crystals.

Previous studies of the equilibrium patterns of six point vortices with the same circulations have found only two stable equilibrium patterns: a pentagon plus one central vortex, and a hexagon, as shown in Fig.2.2.a and 2.2.b[47]. However, we find that there is another stable pattern – triangular pattern. As pointed out by Havelock, a stable pattern becomes unstable as its size becomes too large and the vortices are too close to the circular boundary[46]. The hexagon pattern becomes unstable if the radial position of the point vortices is greater than $0.54\rho_0$. The triangular pattern emerges from the hexagon pattern as it becomes unstable. If we label the six point vortices of the hexagon pattern in anti-clockwise direction with numbers from 1 to 6, we find that the even (or odd) numbered vortices are pulled towards the boundary, whereas the odd (or even) numbered vortices are pushed towards the center. The triangular pattern is stable until the radial position of the outer three point vortices is greater than $0.664\rho_0$. In Fig.2.2.c we show a triangular pattern. In this pattern, the radial position of the even numbered point vortices is $0.661446\rho_0$, and the radial position of the odd numbered point vortices is $0.486147\rho_0$.

2.4 Finite Temperature Solutions

To compare quantitatively the RMFE theory with the experiments, we must solve numerically the RMFE state for given total energy H_0, total angular momentum L_0, total circulation Γ_0, the vorticity level ω_f, and the number N of the strong vortices and the vorticity distributions ζ_i in each of them.

The numerical method consists of two steps. First, for given values of the parameters β, Ω, μ and the positions $\mathbf{R}_i, i = 1, ..., N$, we solve the stream function $\bar{\psi}$ from Eqs.(2.21) and (2.36), which are combined into a nonlinear elliptic equation for $\bar{\psi}$:

$$\nabla^2\bar{\psi} = -\bar{\omega} = \begin{cases} -\zeta_i(|\mathbf{r} - \mathbf{R}_i|) & , \quad \text{if } \mathbf{r} \text{ is in the } i\text{-th strong vortex,} \\ -\omega_f / \left(e^{\beta\omega_f\left(\bar{\psi} + \frac{1}{2}\Omega r^2 - \mu\right)} + 1\right) & , \quad \text{if } \mathbf{r} \text{ is in the background.} \end{cases} \tag{2.72}$$

We solve this nonlinear elliptic equation using Brandt's Full Storage Algorithm (FAS), a nonlinear multi-grid method[48], on 513 × 513 uniform grids. With $\bar{\psi}$ solved, $\bar{\omega}$ is obtained using the right half of the above equation. Then H, L, Γ, and the velocities of the strong vortices

$$\mathbf{V}_i = \frac{\partial\bar{\psi}}{\partial\mathbf{R}_i} \times \hat{\mathbf{z}} \tag{2.73}$$

are calculated.

Second, we search for the appropriate values of β, Ω, μ, and $\mathbf{R}_i, i = 1, ..., N$, such that $H = H_0$, $L = L_0$, $\Gamma = \Gamma_0$, and $\mathbf{V}_i = 0, i = 1, ..., N$. The searching is done with the Broyden's Method, a multi-dimensional secant method [49].

To ensure that the positions of the strong vortices obtained as above indeed maximize the fluid entropy of the background, we calculate the Jacobian matrix as defined in Eq.(2.34), and calculate its eigenvalues using the Jacobi method[50]. For stable configurations, the eigenvalues of the Jacobian matrix are all non-negative.

The background of the finite temperature solutions has the following features: the edge falls off gradually, since the vorticity elements near the edge can fluctuate in energy by an amount of order $1/\beta$; also, near a strong vortex the background is slightly depressed, since $\bar{\psi}$ tend to increase because of the strong vortex. The length scale over which the edge falls off depends all of the parameters of the RMFE state. Qualitatively, the length scale decrease as β, Ω, or the radius of the background increases.

2.5 Comparison with the Experiments

In the comparison of the RMFE theory with the experiments, we use the following units for the physical quantities: length – the radius ρ_w of the circular boundary, vorticity – Γ_0/ρ_w^2, so that the total circulation of the flow is 1.

2.5.1 Survey of the Strong Vortices and Measurement of the Conserved Quantities

In the vortex crystals, the strong vortices are well separated. We use a simplified version of the algorithm proposed by McWilliams[40] for isolating the strong vortices from the background. The simplified algorithm is based on the observation that a strong vortex has an axially symmetric vorticity distribution around its maximum vorticity, which is $3 \sim 4$ times larger than the average vorticity of the background, and has a steep radial vorticity drop near its boundary. To get the i-th strong vortex, we first identify a local maximum of the vorticity that is larger than a threshold ζ_{th} (we use $\zeta_{th} = 4.0$), and take its position as $\mathbf{R}_i$ of the strong vortex. We then calculate the angle-averaged vorticity $\zeta_i(|\mathbf{r} - \mathbf{R}_i|)$ at a distance $\rho = |\mathbf{r} - \mathbf{R}_i|$. If ζ_i is larger than ζ_{th}, we calculate ζ_i at a larger ρ; otherwise, we calculate $d\zeta_i/d\rho$. This process is continued until $d\zeta_i/d\rho$ is greater than a critical value δ (we use $\delta = -15.0$). The value of ρ at which the process is terminated is taken as the radius of the strong vortex. In this process, the vorticity distribution $\zeta_i(|\mathbf{r} - \mathbf{R}_i|)$ inside the strong vortex is determined.

In the calculations of Γ_0, L_0, and H_0 from the observed vorticity field, it is important to exclude the low vorticity field beyond the region of the main flow. This low vorticity field consists of experimental noise and, possibly, thin filaments that are ejected early in the flow evolution and since detached from the mixing of the background flow. Although the vorticity level of of this field is small (about 10^{-2}), it can affect the value of the conserved quantities, especially L_0, if not excluded.

2.5.2 Choice of ω_f

The value of ω_f is determined by the following considerations:(1) ω_f must be larger than or equal to ω_{max}, the maximum of the observed background vorticity, which is coarse grained by the experimental imaging system; (2) since the observed vortex crystals appear to be close to the Fermi degenerate solution of the zero temperature case, in some macroscopic region of the background the coarse grained vorticity should approach ω_f. We therefore take $\omega_f = \omega_{max}$. Furthermore, we find that all of the observed vortex crystals have $\omega_{max} = 2.15 \pm 0.05$, apparently because their initial conditions are similar, as shown in Fig.2.3. Therefore, $\omega_f = 2.15$ is used in all of the calculations.

2.5.3 Results

For each observed vortex crystal, we measure the conserved quantities Γ_0, L_0, and H_0, and obtain the number N of the strong vortices and vorticity distribution ζ_i in each of them. With $\omega_f = 2.15$, we numerically calculate the corresponding RMFE state.

The RMFE solutions reproduce the observed vortex crystal patterns, as shown in Fig.2.4. Also, the observed background vorticity is close to that of the

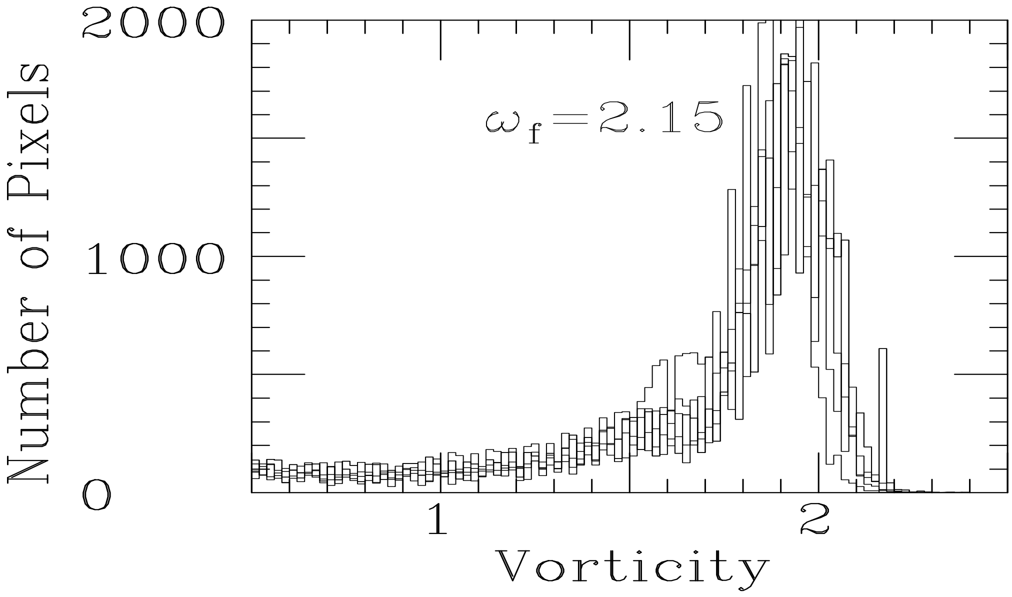

Figure 2.3: The graph presents the number of CCD camera pixels corresponding to the observed coarse-grained vorticity of the background. Several curves corresponding to different vortex crystals are plotted.

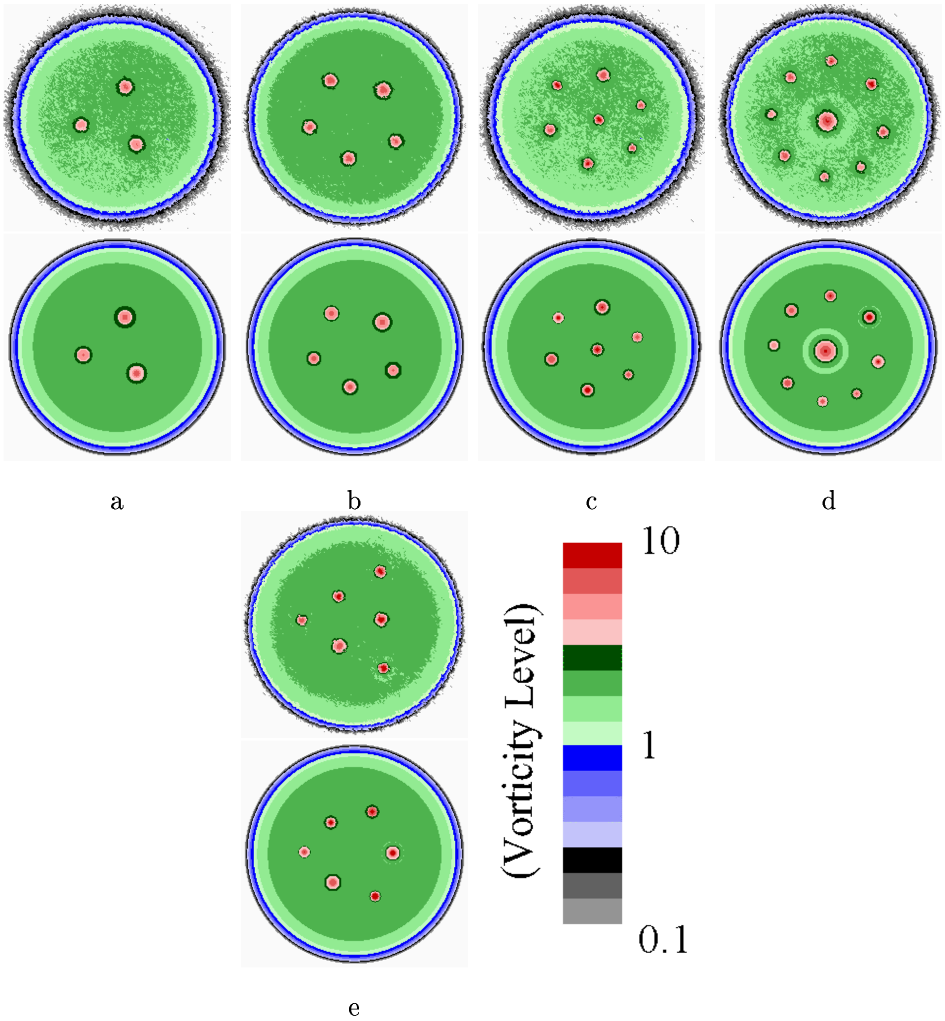

Figure 2.4: Row 1 and 3: examples of experimental images of vortex crystal states (taken from Ref.[38]). Row 2 and 4: corresponding regional maximum fluid entropy states. False color contour plots of vorticity are displayed.

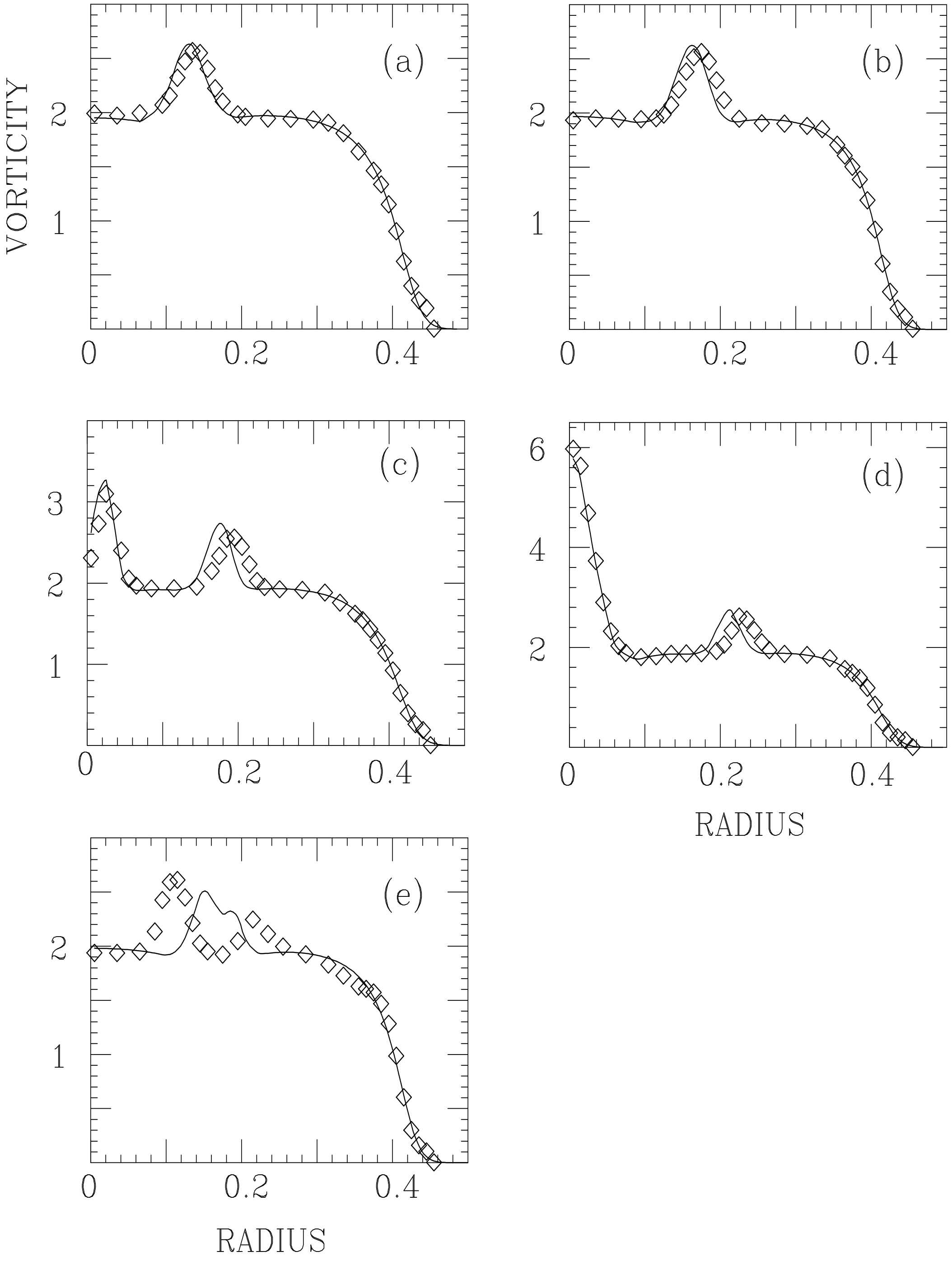

Figure 2.5: Comparison between theory (solid line) and experiment (symbol ◇) for the θ-averaged vorticity profiles of the vortex crystal states in Fig.2.4

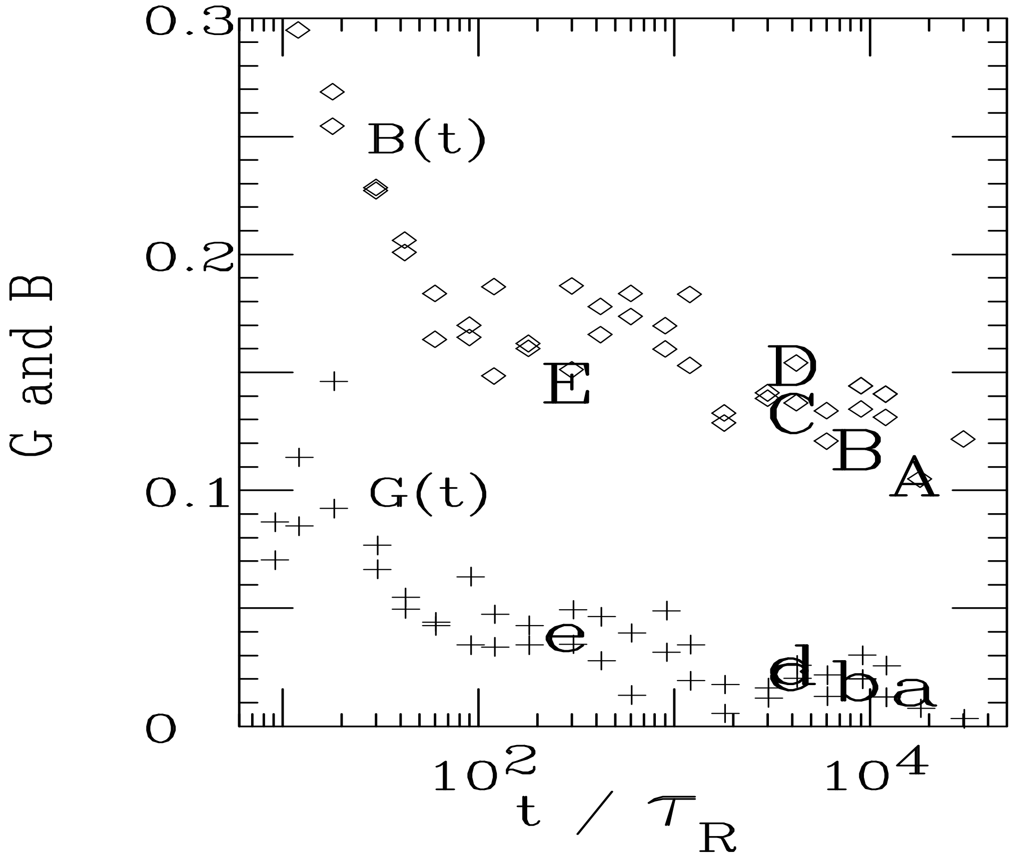

Figure 2.6: The evolution of the geometry deviation G (symbol +) and the background deviation B (symbol ⋄) for the flow discussed in Ref.[38]. Symbols a,b,c,d,e (for geometry deviations), and A,B,C,D,E (for background deviations) correspond to the states shown in Fig.2.4.

corresponding RMFE state, as can be seen in the angle-averaged vorticity profiles, Fig.2.5. Some of the patterns appear to agree more closely with the theory than others. There are two natural ways of quantitatively measuring this accuracy: the deviation of the crystal geometry and the deviation of the background vorticity. The geometry deviation G is defined as

$$G = \sqrt{\frac{\sum_{i \neq j}(d_{ij}^{exp} - d_{ij}^{th})^2}{N(N-1)}}, \tag{2.74}$$

where d_{ij}^{exp} and d_{ij}^{th} are the distances between the i-th and the j-th strong vortices in experiment and in theory, respectively. The background deviation B is defined as

$$B = \sqrt{\frac{\int_{D_b} d\mathbf{r}^2 \bar{\omega}(\mathbf{r})(\bar{\omega}^{exp}(\mathbf{r}) - \bar{\omega}(\mathbf{r}))^2}{\int_{D_b} d\mathbf{r}^2 \bar{\omega}(\mathbf{r})}}, \tag{2.75}$$

where $\bar{\omega}^{exp}(\mathbf{r})$ and $\bar{\omega}(\mathbf{r})$ are the vorticity distributions of the background in experiment and in theory, respectively. Here the region of integration excludes regions occupied by the strong vortices both in experiment and in theory. The average is weighted by $\bar{\omega}(\mathbf{r})$ in order to reduce the effects of the experimental noise from the regions of low vorticity.

The values of these deviations for the vortex crystals displayed in Fig.2.4 and Fig.2.5 are indicated in Fig.2.6 at the times when the patterns were observed. Here $\tau_R = 170\mu s$ is the bulk rotation time of the flow as in Ref.[38]. The deviations in Fig.2.4e and Fig.2.5e are relatively large. We argue that this is because this data was taken at an early time, and the flow has not yet settled into the RMFE state. To justify this claim, we have analyzed the time evolution of the flow that led to vortex crystals discussed in Ref.[38]. For each experimental image of this flow after strong vortices have formed, geometry and background deviations from the corresponding RMFE state were calculated. The results are shown in Fig.2.6, which clearly show that the deviations decrease as time elapses. The dynamics leads the system towards RMFE states.

2.6 Discussion

2.6.1 Maximization of the Boltzman Entropy

Over the years, the Boltzman statistics has been applied to describe the free relaxation of 2D turbulence[12, 10, 11]. This approach assumes that the microscopic vorticity distribution of the flow can be represented as a distribution of point vortices. The incompressibility of the Euler flow is therefore ignored. Assuming the ergodic mixing of these point vortices in the relaxed state of the turbulent flow, the Boltzman entropy

$$S_B = -\int d\mathbf{r}^2 \bar{\omega} \ln \bar{\omega} \tag{2.76}$$

is maximized with the constraints of the conservations of Γ, L, and H. Compared with the fluid entropy, Eq.(2.13), the Boltzman entropy is much simpler; however, it does not conserve the generalized enstrophy. This approach can be justified only if the incompressibility of the microscopic vorticity is not important. When the temperature is high ($i.e.$ $\beta \to 0$) or the microscopic vorticity levels are much lager than the coarse-grained vorticity, the microscopic vorticity are spread out and do not congregate in macroscopic domain. In these cases, the relaxed state obtained by maximizing the fluid entropy is the same as that by maximizing the Boltzman entropy[13].

An interesting question is whether we can explain the observed vortex crystals by maximizing the Boltzman entropy, instead of the fluid entropy, of the background. Following a procedure similar to the derivation of RMFE equations, we find that the maximization of the Boltzman entropy, Eq.(2.76), of the background yields the Boltzman distribution for the coarse-grained vorticity distribution $\bar{\omega}$ in the background:

$$\bar{\omega}(\mathbf{r}) = e^{-1-\beta(\bar{\psi}+\frac{1}{2}\Omega r^2-\mu)} = \omega_0 e^{-\beta(\bar{\psi}+\Omega r^2/2)}, \tag{2.77}$$

where

$$\omega_0 \equiv e^{\beta\mu-1} \tag{2.78}$$

is a constant, β the inverse temperature, and Ω the angular frequency of the rotating frame of the equilibrium. The positions of the strong vortices are still determined by Eq.(2.31).

The maximization of the Boltzman entropy of the background can not explain the observed vortex crystals we have been discussed so far. As shown in the radial profiles, Fig.2.5, the edges of the angle averaged background vorticity distributions of the vortex crystals fall off quite steeply, which indicates that a low

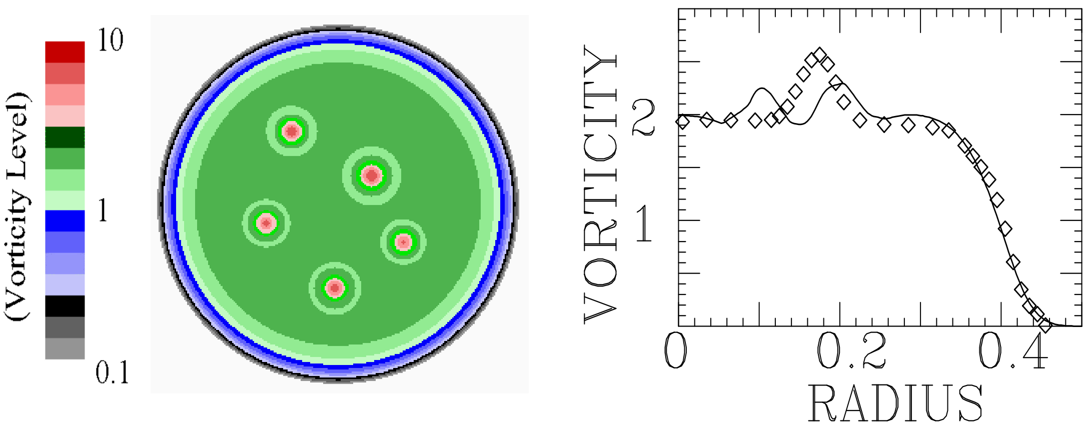

Figure 2.7: Left: RMFE state corresponding to the vortex crystal shown in Fig.II.3.b, with $\omega_f = 1000$. Right: Comparison of the angle averaged radial profiles. The solid line is for RMFE state, and the symbol $\diamond$ is for the observed vortex crystal.

temperature (or large β) is necessary for matching the Boltzman distribution with the observed background. We can understand the the low temperature Boltzman distributions by studying the zero temperature case. From Eq.(2.77), we see that for $\beta = \infty$,

$$\bar{\psi} + \frac{1}{2}\Omega r^2 - \mu = 0 \tag{2.79}$$

in the background. This is exactly the same as the shear-free equilibrium solution for zero temperature RMFE state, therefore, the strong vortices are completely shielded and the strong vortices can take arbitrary positions as long as the shielding holes do not overlap. No solutions similar to the vortex crystals are required.

To quantitatively show the importance of the incompressibility of the microscopic vorticity elements, we compare the observed vortex crystals with corresponding RMFE states, taking ω_f arbitrarily large. In Fig.2.7, we show the RMFE state corresponding to the vortex crystal shown in Fig.2.4.b, with $\omega_f = 1000$. Since ω_f is large, the maximization of the fluid entropy is equivalent to the maximization of the Boltzman entropy. The result is reminiscent of the shear-free equilibrium at

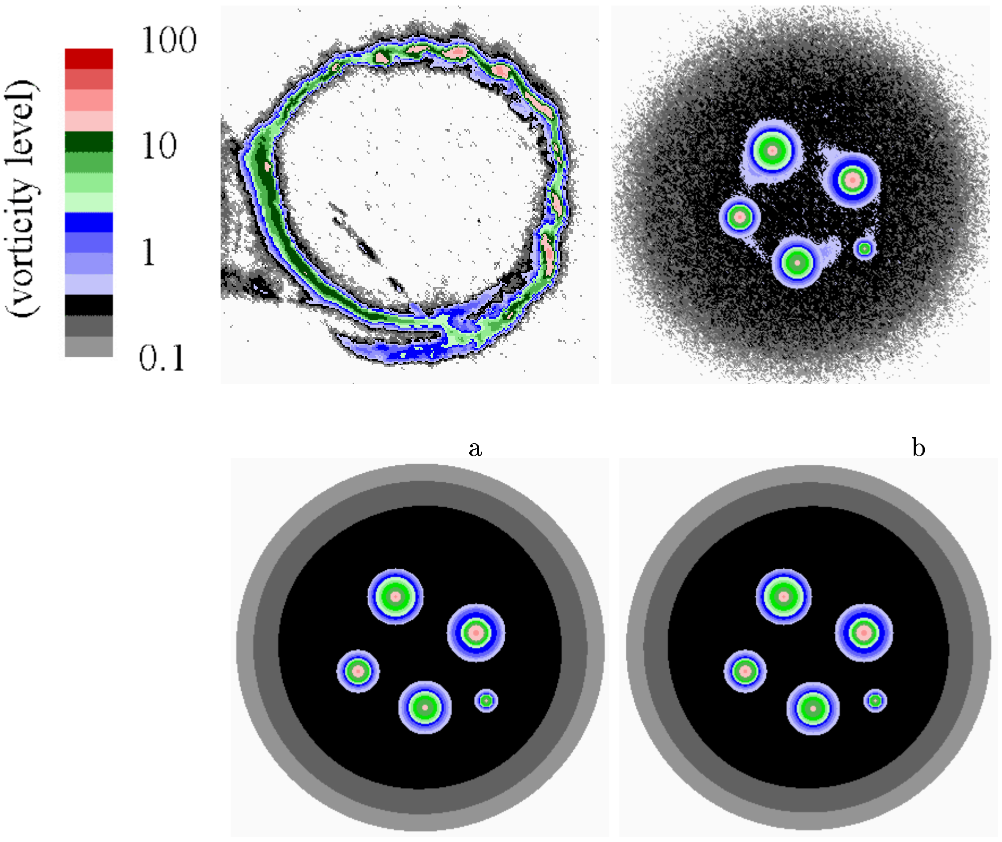

a b

c d

Figure 2.8: Vortex crystal formed from a ring initial condition. (a) Initial condition in the experiment. (b) Observed vortex crystal state. (c) Corresponding RMFE state with $\omega_f = 2.15$. (d) Corresponding RMFE state with $\omega_f = 100$.

zero temperature: the background vorticity is deeply depressed around the strong vortices, and the strong vortices take irregular patterns.

Recently, experiments and simulations have found that vortex crystals can also form from initial vorticity distributions that form a single ring[51]. However, the vortex crystals are quite different from those observed in Ref.[38] and have been discussed so far. The background flow is spread out, and its vorticity is low, as shown in Fig.2.8 and Fig.2.9. As we can see in Fig.2.9, the edge of the angle averaged vorticity profile of the background falls off gradually, indicating that the background is in a high temperature state. For these vortex crystals, we expect the incompressibility of the vorticity elements is not important. Indeed, as shown

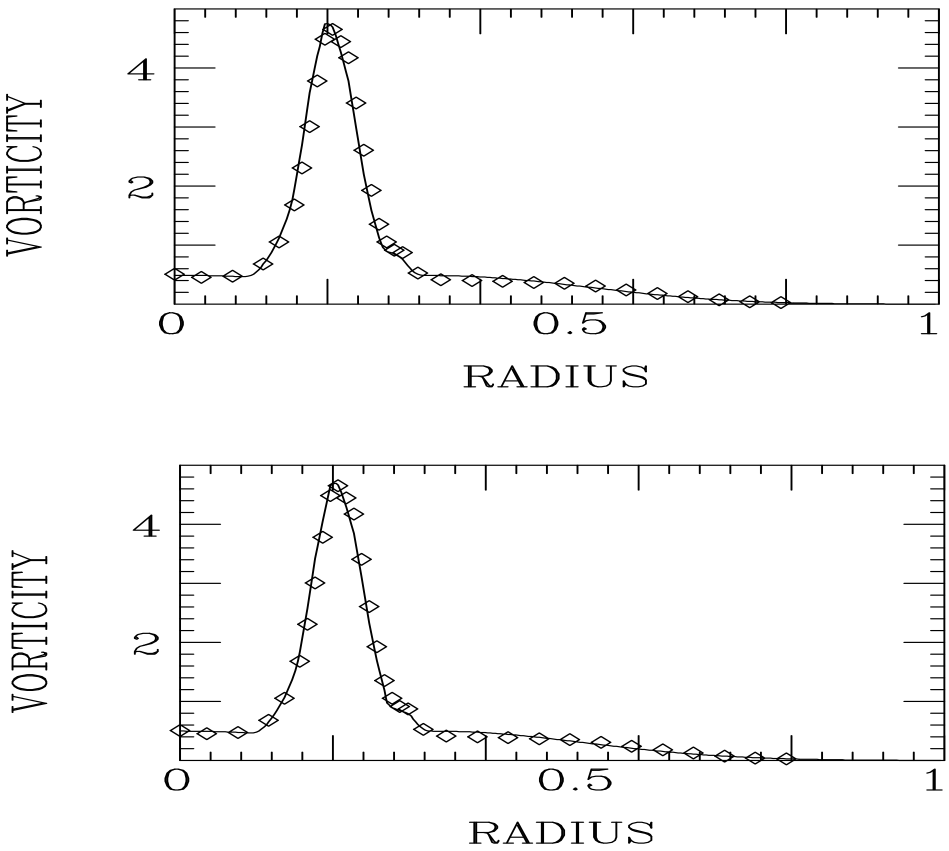

Figure 2.9: Comparison of the θ-averaged vorticity profile of the vortex crystal from ring initial condition (symbol $\diamond$) with those of the corresponding RMFE states (solid line) with $\omega_f = 2.15$ (upper graph) and $\omega_f = 100$ (lower graph). The images are shown in Fig.2.8.

in Fig.2.8 and Fig.2.9, the RMFE state, with both $\omega_f = 2.15$ and $\omega_f = 100$, agrees with the observation. [4] In this case, the predictions based on the Boltzman entropy are the same as those based on the fluid entropy. Also, unlike the low temperature case, the Boltzman statistics does not lead to shielding of the strong vortices since the temperature is high; therefore, the strong vortices can form vortex crystal patterns.

---

[4] Previously we have taken ω_f as the maximum of the observed background vorticity in the vortex crystal states, ω_{max} (see section 2.5.2). Here the situation is different. The background is in a high temperature state and is far from the Fermi degenerate solution of the zero temperature case. Therefore, we do not expect that in any macroscopic region ω_f should approach ω_{max}, which is about 0.5.

2.6.2 Minimization of Enstrophy

The minimum enstrophy principle is another statistical approach besides the maximum entropy principle for describing the free relaxation of 2D turbulence. Based on a selective decay hypothesis, this principle states that the coarse-grained enstrophy of the 2D flow,

$$\bar{Z}_2 = \int d\mathbf{r}^2 \bar{\omega}^2, \tag{2.80}$$

which is the enstrophy Z_2 with the vorticity coarse-grained, is minimized subject to the constraints that Γ, L and H are conserved [27, 28, 29]. Experiments have found that, from some initial conditions, the 2D turbulent flow indeed relax towards minimum enstrophy states[30].

Naturally, one may wonder if we can explain the vortex crystals as the minimum enstrophy states, instead of the maximum fluid entropy states, of the background. To answer this question, we do the constrained minimization of $\bar{Z}_2$, following a procedure similar to the derivation of the RMFE theory. This gives the equation for the coarse-grained vorticity of the background as follows:

$$\bar{\omega} = \beta\left(\bar{\psi} + \frac{1}{2}\Omega r^2 - \mu\right), \tag{2.81}$$

where β, Ω and μ are Lagrange multipliers. The equation for the positions of the strong vortices is the same as in the RMFE theory, Eq.(2.31).

The background vorticity distribution given by the minimum enstrophy principle, Eq.(2.81), can not explain the observed vortex crystal states. As shown in the angle-averaged vorticity profiles, Fig.2.5, the vorticity of the background is approximately constant inside the flow and falls off quickly at the edge. To obtain the approximately constant vorticity with Eq.(2.81), one needs $\beta >> 1$ and $0 < \bar{\psi} + \frac{1}{2}\Omega r^2 - \mu << 1$. However, outside of the flow, the the contribution from the term $\frac{1}{2}\Omega r^2$ dominates and $\bar{\psi} + \frac{1}{2}\Omega r^2 - \mu \sim 1$. This, in return, gives large vorticity distribution according to Eq.(2.81), which is not true in reality.

2.7 Acknowledgements

Part of this chapter has been published in Physical Review Letters, D. Z. Jin and D. H. E. Dubin, **80**, 4434 (1998). The thesis author was the primary investigator and single author of this paper.

Chapter 3

Dynamics of Vortex Crystals

3.1 Introduction

In the previous chapter, we have shown that the vortex crystals are well described as regional maximum fluid entropy states. In this chapter, we study the interaction between the strong vortices and the background using a simple model of the vortex crystals. The model consists of several point vortices, which model the strong vortices, and a vortex patch (region with constant vorticity), which models the low vorticity background. The point vortices are inside the vortex patch, and the flow of the model is subject to a free-space boundary condition (*i.e.* there are no surrounding boundaries).

We study in particular the perturbation limit of the model, in which the contour of the vortex patch is nearly circular, and the total circulation of the point vortices is much smaller than that of the vortex patch. This is a reasonable model, since in the observed vortex crystal the background often has nearly constant vorticity within an approximately circular region, and the strong vortices often have intense vorticity, small radii, and small total circulation compared to that of the background. With this model, we study how the point vortices and the vortex patch affect each other, and in particular, the possibility of generating chaotic mixing in the vortex patch. [1]

---

[1] Lansky *et al* have studied a similar model in which one point vortex is placed outside of the nearly

Our model relates to two important problems in 2D vortex dynamics: the dynamics of a collection of point vortices, and the dynamics of a vortex patch. For a collection of point vortices, the equilibrium patterns have been exhaustively searched, and their stability properties have been determined[46, 47]. The dynamics of the system is Hamiltonian and is chaotic in most cases[53].

A vortex patch is the simplest example of an extended vortex. It has many rotating equilibria, among which the circular shape (so called Rankine patch) is the most fundamental one[54]. The circular patch supports steadily propagating infinitesimal perturbations, or Kelvin waves, on its boundary. Contour dynamics has been used extensively to study the evolution of small disturbances added to equilibrium vortex patches[55]. Filamentation, or the formation of filaments of vorticity drawn off the vortex patch, often results from the growth of linearly unstable Kelvin waves[56]. Numerical-analytical evidence is also present for long time filamentation of arbitrarily small, linearly stable disturbances[57].

Our model combines these two problems. In the perturbation limit, which is the main topic of this work, the dominant dynamics of the model is the rotation of the vortex patch. To describe the dynamics of the point vortices as well as the disturbance on the vortex patch, it is useful to go to the rotating frame that rotates with the vortex patch. The following description of the dynamics of the perturbation limit is in this rotating frame.

There are fast and slow time scales in the dynamics. The fast time scale is on order of a rotation period of the vortex patch, whereas the slow time scale is on order of the rotation period of the vortex patch multiplied by $1/\lambda$, where λ is the ratio between the average circulation of the point vortices and the circulation of the vortex patch.

The disturbance on the vortex patch can be decomposed into two parts: an "image charge" part, which is determined by the point vortices and changes in

---

circular vortex patch. They showed that the point vortex can merge into the vortex patch through successive resonances[52].

slow time scale; and free-streaming Kelvin waves, the same waves supported by a circular patch, which is essentially fast time scale phenomenon and is affected by the point vortices only in the slow time scale.

In the fast time scale, the point vortices oscillate with amplitudes of order λ times the radius of the vortex patch due to the influence of the free-streaming Kelvin waves. In the slow time scale, however, the point vortices move over distances comparable to the radius of the vortex patch under the influence of other point vortices and the image charge part of the disturbance on the vortex patch. Moreover, the effect of the image charge part on the slow time dynamics of the point vortices is exactly the same as that of a circular free-slip boundary, with radius equal to that of the vortex patch. In other words, the slow time dynamics of the point vortices is the same as the dynamics of point vortices subject to a free-slip circular boundary, with the radius of the boundary equal to that of the vortex patch. Therefore, all results of the point vortex dynamics in a circular boundary can be readily applied to the slow time dynamics of the point vortices. For example, we know right away the equilibrium patterns of the point vortices; we know that the Havelock instability[46] applies to these equilibrium patterns: the point vortices can not be too close to the contour of the vortex patch, otherwise they will be attracted towards the contour, and the equilibrium pattern will be unstable; we also know that the dynamics of the point vortices is in general chaotic.

The disturbance on the vortex patch also evolves in the slow time scale. The image charge part follows the change of the positions of the point vortices in the slow time scale. The Kelvin waves, on the other hand, interact with the image charge part and the point vortices in the slow time scale. This interaction, especially that with the image charge part, often leads to filamentation of the Kelvin waves. The filamentation time is on the order of $\lambda^{-1} \ln \lambda^{-1}$ times the rotation period of the vortex patch. Our calculation can not be carried over the time beyond the filamentation. To follow the subsequent evolution of the system, we use vortex-in-cell simulation. The simulation results suggests that the filamentation often introduces "holes" into the vortex patch and starts a chaotic mixing of the vortex patch. This supports the idea presented by the regional maximum fluid entropy theory of vortex crystal formation.

3.2 The Model

The model consists of M point vortices and a vortex patch. The point vortices are inside the vortex patch. The flow is subject to a free-space boundary condition. The positions of the point vortices are $\mathbf{R}_m(t)$, and their circulations are Γ_m, with $m = 1, ..., M$. The vortex patch has a constant vorticity ω_0, and its shape is specified by a smooth single valued function $r_c(\theta, t)$, which is the radial position of the boundary point at polar angle θ at time t. A generic point in the plane is denoted as $\mathbf{r} = (r, \theta)$, where r is the radial position of the point, and θ is the polar angle.

The perturbation limit of the model, which is the main subject of this work, is defined by two conditions. One condition is that the average circulation of the point vortices, $\Gamma_v = \frac{1}{M}\sum_m \Gamma_m$, is much smaller than the circulation of the vortex patch, $\Gamma = \int d\mathbf{r}^2 \omega_0$, where the region of integration is inside the vortex patch. This defines a small parameter

$$\lambda = \frac{\Gamma_v}{\Gamma}, \tag{3.1}$$

which we refer as the perturbation strength. The other condition is that the shape of the vortex patch deviates from the circular patch with constant vorticity ω_0 and circulation Γ by a small amount $\epsilon(\theta, t)$; furthermore, this deviation compared to the radius of the circular patch, r_b, is of order λ, *i.e.*

$$\left| \frac{\epsilon}{r_b} \right| \sim \lambda. \tag{3.2}$$

The circular patch is referred as the unperturbed patch, and its radius r_b is determined by $\Gamma = \pi \omega_0 r_b^2$.

3.3 Units of the physical quantities

In the perturbation limit, there are natural units for the physical quantities. The unit of the length is r_b, and the unit of time is $t_0 = 4\pi/\omega_0$, which is the rotation period of the unperturbed patch. Consequently, the unit of the velocity is $r_b/t_0 = r_b\omega_0/4\pi$, that of vorticity is $1/t_0 = \omega_0/4\pi$. Also, the unit of the circulation is $\omega_0 r_b^2/4\pi$, and that of the stream function ψ is $\omega_0 r_b^2/4\pi$.

In theses units, the unperturbed patch has radius 1, vorticity 4π, and circulation $4\pi^2$. In the rest of the chapter, these units will be used for the physical quantities and all of the equations will be dimensionless.

3.4 Equations of Motion

3.4.1 General Equations

The evolution equation for the contour of the vortex patch, defined by function $r_c(\theta, t)$, can be derived by considering the motion of a contour point at $\mathbf{r}_c = (r_c, \theta)$. After a infinitesimal time interval dt, the point moves to a new position $\mathbf{r}_c^{'} = (r_c^{'}, \theta^{'})$, where $\theta^{'} = \theta + v_\theta dt/r_c$, and $r_c^{'} = r_c + v_r dt$. Here v_r and v_θ are the radial and azimuthal components of the velocity of the boundary point. Therefore,

$$r_c^{'} = r_c(\theta^{'}, t + dt) = r_c(\theta + \frac{v_\theta dt}{r_c}, t + dt) = r_c(\theta, t) + v_r dt. \tag{3.3}$$

Taylor expanding the above equation to the first order in dt, we obtain

$$\frac{\partial r_c}{\partial t} + \frac{v_\theta}{r_c}\frac{\partial r_c}{\partial \theta} = v_r. \tag{3.4}$$

The boundary condition for this nonlinear partial differential equation is

$$r_c(\theta + 2\pi, t) = r_c(\theta, t). \tag{3.5}$$

The equations of motion for the point vortices are simply given by

$$\frac{d\mathbf{R}_m}{dt} = \mathbf{V}_m, \tag{3.6}$$

where $\mathbf{V}_m$ is the velocity of the m-th point vortex.

To complete the equations of motion, the velocities of the point vortices and the contour points must be calculated. This is done by calculating the stream function ψ and applying the relation between the stream function and the velocity, Eq.(1.4). The stream function can be calculated from Eq.(1.5), recognizing that the vorticity distribution of the flow of the model is

$$\omega(\mathbf{r}) = \omega_b(\mathbf{r}) + \sum_m \Gamma_m \delta(\mathbf{r} - \mathbf{R}_m), \tag{3.7}$$

where

$$\omega_b(\mathbf{r}) = \begin{cases} 4\pi \quad , & \mathbf{r} \text{ inside the vortex patch} \\ 0 \quad , & \mathbf{r} \text{ outside the vortex patch} \end{cases} \tag{3.8}$$

is the vorticity distribution of the vortex patch. The free-space Green's function

$$G(\mathbf{r} - \mathbf{r}') = -\frac{1}{2\pi} \ln |\mathbf{r} - \mathbf{r}'| \tag{3.9}$$

satisfies

$$\nabla^2 G(\mathbf{r} - \mathbf{r}') = -\delta(\mathbf{r} - \mathbf{r}'). \tag{3.10}$$

Therefore, the stream function is given by

$$\psi = \int d\mathbf{r}'^2 \omega(\mathbf{r}') G(\mathbf{r} - \mathbf{r}') = \psi_b + \psi_v, \tag{3.11}$$

where ψ_b and ψ_v are contributions from the vortex patch and the point vortices, respectively:

$$\psi_b = \int d\mathbf{r}'^2 \omega_b(\mathbf{r}') G(\mathbf{r} - \mathbf{r}'), \tag{3.12}$$

$$\psi_v = \sum_m \Gamma_m G(\mathbf{R}_m - \mathbf{r}). \tag{3.13}$$

The velocity at point $\mathbf{r}$, then, is

$$\mathbf{v} = \nabla \times \psi \hat{\mathbf{z}} = \mathbf{v}_b + \mathbf{v}_v, \tag{3.14}$$

where $\mathbf{v}_b = \nabla \psi_b \times \hat{\mathbf{z}}$ is the velocity induced by the vortex patch, and $\mathbf{v}_v = \nabla \psi_v \times \hat{\mathbf{z}}$ is the velocity induced by the point vortices.

It is convenient to explicitly work out the radial and azimuthal components of the velocities. Denoting V_r and V_θ as the radial and and azimuthal components of the velocity induced by the point vortices, $\mathbf{v}_v$,we have

$$\begin{aligned} V_r(\mathbf{r}) &= \hat{\mathbf{r}} \cdot \nabla\psi_v \times \hat{\mathbf{z}} = \frac{1}{r}\frac{\partial\psi_v}{\partial\theta} \\ &= -\sum_m \left(\frac{\Gamma_m}{2\pi}\right) \frac{R_m \sin(\theta-\Theta_m)}{r^2+R_m^2-2rR_m\cos(\theta-\Theta_m)}, \end{aligned} \tag{3.15}$$

where R_m, Θ_m are radial position and polar angle of the position vector $\mathbf{R}_m$, and

$$\begin{aligned} V_\theta(\mathbf{r}) &= \hat{\theta} \cdot \nabla\psi_v \times \hat{\mathbf{z}} = -\frac{\partial\psi_v}{\partial r} \\ &= \sum_m \left(\frac{\Gamma_m}{2\pi}\right) \frac{r - R_m \cos(\theta-\Theta_m)}{r^2+R_m^2-2rR_m\cos(\theta-\Theta_m)}. \end{aligned} \tag{3.16}$$

Here $\hat{\mathbf{r}}$ and $\hat{\theta}$ are unit vectors in radial and azimuthal directions, respectively.

The velocity induced by the vortex patch, $\mathbf{v}_b$, can be reduced into a line integral along the contour of the patch as follows[58]:

$$\begin{aligned} \mathbf{v}_b &= \nabla\psi_b \times \hat{\mathbf{z}} = \int d\mathbf{r}'^2 \omega_b(\mathbf{r}')\nabla_r G(\mathbf{r}-\mathbf{r}') \times \hat{\mathbf{z}} \\ &= -\int d\mathbf{r}'^2 \omega_b(\mathbf{r}')\nabla_{r'} G(\mathbf{r}-\mathbf{r}') \times \hat{\mathbf{z}} \\ &= 4\pi \oint d\mathbf{l}' G(\mathbf{r}-\mathbf{r}'_c), \end{aligned} \tag{3.17}$$

where $d\mathbf{l}'$ is an infinitesimal vector in the anti-clockwise direction along the contour of the vortex patch, and $\mathbf{r}'_c = (r_c(\theta', t), \theta')$ is the point on the contour at angle θ'. In the last step of the derivation, integration by part is used, and the relation $\nabla_{r'}\omega_b(\mathbf{r}') = -4\pi\hat{\mathbf{n}}'\delta(\mathbf{r}'-\mathbf{r}'_c)$, where $\hat{\mathbf{n}}'$ is the unit vector normal to the contour of the vortex patch at $\mathbf{r}'_c$, is applied.

We further obtain the radial and azimuthal components of the velocity due to the vortex patch, denoted as u_r and u_θ, respectively. Using

$$d\mathbf{l}' = \hat{\mathbf{r}}'_c dr'_c + \hat{\theta}'_c r'_c d\theta' = \left(\hat{\mathbf{r}}'_c \frac{\partial r'_c}{\partial\theta'} + \hat{\theta}'_c r'_c\right) d\theta', \tag{3.18}$$

where $\hat{\mathbf{r}}'_c$ and $\hat{\theta}'_c$ are the unit vectors in the radial and azimuthal directions at the contour point $\mathbf{r}'_c$, and

$$\hat{\mathbf{r}}'_c \cdot \hat{\mathbf{r}} \;=\; \cos(\theta'-\theta), \quad \hat{\theta}'_c \cdot \hat{\mathbf{r}} = -\sin(\theta'-\theta),$$

$$\hat{\mathbf{r}}_c^{'} \cdot \hat{\theta} \;=\; \sin(\theta^{'} - \theta), \qquad \hat{\theta}_c^{'} \cdot \hat{\theta} = \cos(\theta^{'} - \theta),$$

we obtain

$$u_r(\mathbf{r}) = \hat{\mathbf{r}} \cdot \mathbf{v}_b = -2 \int_0^{2\pi} d\theta^{'} \left(\cos(\theta^{'} - \theta) \frac{\partial r_c^{'}}{\partial \theta^{'}} - \sin(\theta^{'} - \theta) r_c^{'} \right) \ln |\mathbf{r}_c^{'} - \mathbf{r}|, \qquad (3.19)$$

and

$$u_\theta(\mathbf{r}) = \hat{\theta} \cdot \mathbf{v}_b = -2 \int_0^{2\pi} d\theta^{'} \left(\sin(\theta^{'} - \theta) \frac{\partial r_c^{'}}{\partial \theta^{'}} + \cos(\theta^{'} - \theta) r_c^{'} \right) \ln |\mathbf{r}_c^{'} - \mathbf{r}|. \qquad (3.20)$$

With Eqs.(3.15),(3.16),(3.19) and (3.20) we find that the radial and azimuthal components of the velocity at the contour point $\mathbf{r}_c$ are

$$v_r = V_r(\mathbf{r}_c) + u_r(\mathbf{r}_c), \qquad v_\theta = V_\theta(\mathbf{r}_c) + u_\theta(\mathbf{r}_c), \qquad (3.21)$$

and those on the m-th point vortex are

$$V_{m,r} = V_r^{'}(\mathbf{R}_m) + u_r(\mathbf{R}_m), \qquad V_{m,\theta} = V_\theta^{'}(\mathbf{R}_m) + u_\theta(\mathbf{R}_m), \qquad (3.22)$$

where $V_r^{'}(\mathbf{R}_m)$ and $V_\theta^{'}(\mathbf{R}_m)$ are given by Eqs.(3.15) and (3.16), respectively, with the contribution from the self-field of the m-th point vortex excluded. These expressions for the velocities, together with Eqs.(3.4) and (3.6), complete the equations of motion of our model.

3.4.2 Perturbation Equations

In this section, we derive by Taylor expansion the perturbation limit of the equations of motion for the model. The small parameter in the expansion is λ, the average circulation of the point vortices compared to the circulation of the vortex patch. As we will see later, in order to obtain the leading order solutions that are valid for time scale of order $1/\lambda$, we need to derive the perturbation equation of the contour of the vortex patch correct to $O(\lambda^2)$, and those of the positions of the point vortices to $O(\lambda)$.

The contour of the vortex patch is given by

$$r_c(\theta, t) = 1 + \epsilon(\theta, t), \qquad (3.23)$$

where ϵ is a smooth, single valued function of order λ. Since ϵ is a smooth function, $\partial r_c/\partial\theta$ is of order λ; therefore, in Eq.(3.4) we need to obtain v_θ to $O(\lambda)$ and v_r $O(\lambda^2)$. This is accomplished by Taylor expanding functions $V_r(\mathbf{r}_c), u_r(\mathbf{r}_c)$ and $V_\theta(\mathbf{r}_c), u_\theta(\mathbf{r}_c)$.

Taylor expansion of $V_r(\mathbf{r}_c)$ is straight forward, and the result is

$$V_r(\mathbf{r}_c) = \lambda V_r^{(1)}(\theta,t) + \lambda\epsilon(\theta,t)V_r^{(2)}(\theta,t) + O(\lambda^3), \tag{3.24}$$

where

$$V_r^{(1)}(\theta,t) = -\sum_m \left(\frac{\Gamma_m}{2\pi\lambda}\right)\frac{R_m(t)\sin(\theta-\Theta_m(t))}{1+R_m(t)^2-2R_m(t)\cos(\theta-\Theta_m(t))}, \tag{3.25}$$

and

$$V_r^{(2)}(\theta,t) = \sum_m \left(\frac{\Gamma_m}{\pi\lambda}\right)\frac{R_m(t)\sin(\theta-\Theta_m(t))(1-R_m(t)\cos(\theta-\Theta_m(t)))}{(1+R_m(t)^2-2R_m(t)\cos(\theta-\Theta_m(t)))^2}. \tag{3.26}$$

In the right hand side of Eq.(3.24), the first term is the radial velocity induced by the point vortices evaluated along the contour of the unperturbed circular patch, and the second term is the correction due to the deformation of the contour from the circle.

Taylor expansion of $u_r(\mathbf{r}_c)$ needs a little more care, since it involves an integration of function $\ln|\mathbf{r}_c^{'}-\mathbf{r}_c|$, which is singular when $\mathbf{r}_c^{'}\to\mathbf{r}_c$. Nevertheless, we can prove that

$$\ln|\mathbf{r}_c^{'}-\mathbf{r}_c|^2 = \ln[2(1-\cos(\theta^{'}-\theta))] + (\epsilon^{'}+\epsilon) + \frac{(\epsilon^{'2}+\epsilon^2)\cos(\theta^{'}-\theta)-2\epsilon^{'}\epsilon}{2(1-\cos(\theta^{'}-\theta))} + O(\lambda^3), \tag{3.27}$$

where $r_c^{'} = 1+\epsilon(\theta^{'},t)$ and $\epsilon^{'}\equiv\epsilon(\theta^{'},t)$, is valid even near the singular point $\mathbf{r}_c^{'}=\mathbf{r}_c$ (see appendix 1 at the end of the chapter). With this expansion, we obtain

$$u_r(\mathbf{r}_c) = \int_0^{2\pi} d\theta^{'}\left(\epsilon^{'}-\epsilon\epsilon^{'}+\frac{\epsilon^{'2}}{2}\right)\cot\left(\frac{\theta^{'}-\theta}{2}\right) + O(\lambda^3). \tag{3.28}$$

(Remember that $\epsilon=\epsilon(\theta,t)$ is not a function of $\theta^{'}$.) Combining Eq.(3.24) and (3.28) we arrive at the total radial velocity of the contour point:

$$v_r(\theta,t) = \lambda V_r^{(1)} + \lambda\epsilon V_r^{(2)} + \int_0^{2\pi} d\theta^{'}\left(\epsilon^{'}-\epsilon\epsilon^{'}+\frac{\epsilon^{'2}}{2}\right)\cot\left(\frac{\theta^{'}-\theta}{2}\right) + O(\lambda^3). \tag{3.29}$$

Taylor expansion of $V_\theta(\mathbf{r}_c)$ to $O(\lambda)$ gives

$$V_\theta(\mathbf{r}_c) = \lambda V_\theta^{(1)} + O(\lambda^2), \tag{3.30}$$

where

$$V_\theta^{(1)}(\theta, t) \equiv \sum_m \left(\frac{\Gamma_m}{2\pi\lambda}\right) \frac{1 - R_m(t)\cos(\theta - \Theta_m(t))}{1 + R_m(t)^2 - 2R_m(t)\cos(\theta - \Theta_m(t))}. \tag{3.31}$$

Quantity $\lambda V_\theta^{(1)}$ is the azimuthal velocity due to the point vortices evaluated along the contour of the unperturbed circular patch.

Taylor expansion of $u_\theta(\mathbf{r}_c)$ to $O(\lambda)$ is done with the help of Eq.(3.27). The result is quite simple:

$$u_\theta(\mathbf{r}_c) = 2\pi + O(\lambda^2). \tag{3.32}$$

In the equation above there is no $O(\lambda)$ term. This is related to the fact that the area of the vortex patch is equal to that of the unperturbed circular patch, π, *i.e.*

$$\pi = \int_0^{2\pi} d\theta' \int_0^{r(\theta', t)} dr r = \int_0^{2\pi} d\theta' \frac{r(\theta', t)^2}{2} = \int_0^{2\pi} d\theta' \frac{(1 + \epsilon')^2}{2}, \tag{3.33}$$

which yields

$$\int_0^{2\pi} d\theta' \epsilon' = -\frac{1}{2}\int_0^{2\pi} d\theta' \epsilon'^2 \sim O(\lambda^2). \tag{3.34}$$

Combining Eqs.(3.30) and (3.32), we obtain

$$v_\theta(\theta, t) = 2\pi + \lambda V_\theta^{(1)} + O(\lambda^2). \tag{3.35}$$

Substituting Eqs.(3.23), (3.29) and (3.35) in the evolution equation for the contour of the vortex patch, Eq.(3.4), we arrive at the perturbation equation

$$\frac{\partial \epsilon}{\partial t} + (2\pi - 2\pi\epsilon + \lambda V_\theta^{(1)})\frac{\partial \epsilon}{\partial \theta} = \lambda V_r^{(1)} + \lambda\epsilon V_r^{(2)} + \int_0^{2\pi} d\theta' \left(\epsilon' - \epsilon\epsilon' + \frac{\epsilon'^2}{2}\right) \cot\left(\frac{\theta' - \theta}{2}\right), \tag{3.36}$$

which is correct to $O(\lambda^2)$.

To obtain the perturbation equations correct to $O(\lambda)$ for the motions for the point vortices, we need to Taylor expand the radial and azimuthal velocities of the m-th point vortex, $V_{m,r}$ and $V_{m,\theta}$, to $O(\lambda)$. This is straight forward, and we arrive at

$$V_{m,r} = V_r^{'}(\mathbf{R}_m) + u_r^{(1)}(\mathbf{R}_m, t) + O(\lambda^2), \tag{3.37}$$

where

$$u_r^{(1)}(\mathbf{R}_m, t) = \int_0^{2\pi} d\theta^{'} \frac{2\epsilon(\theta^{'}, t)\sin(\theta^{'} - \Theta_m)}{1 + R_m^2 - 2R_m\cos(\theta^{'} - \Theta_m)} \tag{3.38}$$

is the radial velocity of the m-th point vortex due to the change in the shape of the vortex patch, and

$$V_{m,\theta} = V_\theta^{'}(\mathbf{R}_m) + u_\theta^{(1)}(\mathbf{R}_m, t) + 2\pi R_m + O(\lambda), \tag{3.39}$$

where

$$u_\theta^{(1)}(\mathbf{R}_m, t) = \int_0^{2\pi} d\theta^{'} \frac{2\epsilon(\theta^{'}, t)(R_m - \cos(\theta^{'} - \Theta_m))}{1 + R_m^2 - 2R_m\cos(\theta - \Theta_m)} \tag{3.40}$$

is the azimuthal velocity due to the change in the contour of the vortex patch. Therefore, correct to $O(\lambda)$, the perturbation equations for the point vortices are

$$\frac{dR_m}{dt} = V_r^{'}(\mathbf{R}_m) + u_r^{(1)}(\mathbf{R}_m, t), \tag{3.41}$$

$$R_m\frac{d\Theta_m}{dt} = V_\theta^{'}(\mathbf{R}_m) + u_\theta^{(1)}(\mathbf{R}_m, t) + 2\pi R_m. \tag{3.42}$$

Equations (3.36), (3.41), and (3.42) provide a closed set of perturbation equations describing the evolution of the boundary of the vortex patch, and the motions of the point vortices inside the patch.

3.4.3 Rotating Frame

In the perturbation limit, the dominant dynamics of the model is the rotation of the vortex patch. To see the effects of the perturbations, it is convenient to work in the rotating frame that rotates with the vortex patch. More precisely, we go the frame that rotates with angular frequency 2π, the angular frequency of the rotation of the unperturbed circular patch. When transforming from the lab frame to the rotating frame, the angles of the polar coordinates change as $\theta \to \theta - 2\pi t$ and $\Theta_m \to \Theta_m - 2\pi t$. Accordingly,

$$\frac{\partial\epsilon}{\partial t} \to \frac{\partial\epsilon}{\partial t} - 2\pi\frac{\partial\epsilon}{\partial\theta}, \qquad \frac{d\Theta_m}{dt} \to \frac{d\Theta_m}{dt} - 2\pi. \tag{3.43}$$

Here the quantities on the right hand side of the arrows are measured in the rotating frame. With these transformations, the perturbation equations in the rotating frame can be derived. Equation (3.36) becomes

$$\frac{\partial \epsilon}{\partial t} + (-2\pi\epsilon + \lambda V_\theta^{(1)})\frac{\partial \epsilon}{\partial \theta} = \lambda V_r^{(1)} + \lambda\epsilon V_r^{(2)} + \int_0^{2\pi} d\theta' \left(\epsilon' - \epsilon\epsilon' + \frac{\epsilon'^2}{2}\right) \cot\left(\frac{\theta' - \theta}{2}\right), \tag{3.44}$$

and Eqs.(3.41) and (3.42) become

$$\frac{dR_m}{dt} = V_r'(\mathbf{R}_m) + u_r^{(1)}(\mathbf{R}_m, t), \tag{3.45}$$

$$R_m\frac{d\Theta_m}{dt} = V_\theta'(\mathbf{R}_m) + u_\theta^{(1)}(\mathbf{R}_m, t). \tag{3.46}$$

In these equations, all quantities are measured in the rotating frame. The definitions of $V_\theta^{(1)}, V_r^{(1)}, V_r^{(2)}$ and $u_r^{(1)}, u_\theta^{(1)}$ involve only differences of the angles; therefore, they do not change under the transformation to the rotating frame.

3.4.4 Mode Equations

The evolution equation for ϵ in the rotating frame can be decomposed into the equations for the Fourier modes. Let

$$\epsilon(\theta, t) = \sum_k \epsilon_k(t) e^{ik\theta}, \tag{3.47}$$

where $\epsilon_k(t)$ is the amplitude of the k-th mode. Because of the periodic boundary condition $\epsilon(\theta + 2\pi, t) = \epsilon(\theta, t)$, k must be an integer. Moreover, since ϵ is real, we have

$$\epsilon_k^* = \epsilon_{-k}. \tag{3.48}$$

We also know that

$$\epsilon_0 \sim O(\lambda^2). \tag{3.49}$$

This is obtained by substituting the Fourier expansion, Eq.(3.47), into Eq.(3.34), which is the consequence of the fact that the area of the vortex patch is equal to that of the unperturbed patch.

With Eq.(3.47), we can obtain the Fourier series of Eq.(3.44). It is useful to define the following quantities:

$$V_k = \sum_m \frac{\Gamma_m}{4\pi} R_m^{|k|} e^{-ik\Theta_m}, \tag{3.50}$$

a sum related to the driven response of the contour of the vortex patch to the point vortices, and

$$s_k = \begin{cases} 1 & , \quad k > 0 \\ 0 & , \quad k = 0 \\ -1 & , \quad k < 0 \end{cases} . \tag{3.51}$$

The Fourier series for the terms in the left hand side of Eq.(3.44) are

$$\frac{\partial \epsilon}{\partial t} = \sum_k \frac{d\epsilon_k}{dt} e^{ik\theta}, \tag{3.52}$$

$$-2\pi\epsilon \frac{\partial \epsilon}{\partial \theta} = \sum_k \left(-2\pi i \sum_q q\epsilon_q \epsilon_{k-q} \right) e^{ik\theta}, \tag{3.53}$$

and

$$\begin{aligned} \lambda V_\theta^{(1)} \frac{\partial \epsilon}{\partial \theta} &= \sum_k \left[\sum_m \frac{\Gamma_m}{4\pi} \sum_q iq\epsilon_q \left(\delta_{k,q} + R_m^{|k-q|} e^{i(q-k)\Theta_m} \right) \right] e^{ik\theta} \\ &= \sum_k \left[ik\epsilon_k \sum_m \frac{\Gamma_m}{4\pi} + \sum_q iq\epsilon_q V_{k-q} \right] e^{ik\theta} \\ &= \sum_k \left[ik\epsilon_k \sum_m \frac{\Gamma_m}{4\pi} + \sum_q i(k-q)\epsilon_{k-q} V_q \right] e^{ik\theta}. \end{aligned} \tag{3.54}$$

The Fourier series for the terms in the right hand side of Eq.(3.44) are

$$\int_0^{2\pi} d\theta' \epsilon' \cot\left(\frac{\theta' - \theta}{2} \right) = \sum_{k \neq 0} 2\pi i \frac{k}{|k|} \epsilon_k e^{ik\theta} = \sum_k 2\pi i s_k \epsilon_k e^{ik\theta}, \tag{3.55}$$

$$\begin{aligned} -\int_0^{2\pi} d\theta' \epsilon' \epsilon \cot\left(\frac{\theta' - \theta}{2} \right) &= \sum_k \left(-2\pi i \sum_{q \neq 0} \frac{q}{|q|} \epsilon_q \epsilon_{k-q} \right) e^{ik\theta} \\ &= \sum_k \left(-2\pi i \sum_q s_q \epsilon_q \epsilon_{k-q} \right) e^{ik\theta}, \end{aligned} \tag{3.56}$$

and

$$\begin{aligned} \int_0^{2\pi} d\theta' \frac{\epsilon'^2}{2} \cot\left(\frac{\theta' - \theta}{2} \right) &= \sum_{k \neq 0} \left(i\pi \frac{k}{|k|} \sum_q \epsilon_q \epsilon_{k-q} \right) e^{ik\theta} \\ &= \sum_k \left(i\pi s_k \sum_q \epsilon_q \epsilon_{k-q} \right) e^{ik\theta}. \end{aligned} \tag{3.57}$$

We also have

$$\lambda V_r^{(1)} = -\sum_{k\neq 0}\left(\sum_m \frac{\Gamma_m}{4\pi}\frac{ik}{|k|}R_m^{|k|}e^{-ik\Theta_m}\right)e^{ik\theta} = -\sum_k is_k V_k e^{ik\theta} \tag{3.58}$$

and

$$\begin{aligned}\lambda\epsilon V_r^{(2)} &= \sum_k\left[\sum_m\left(-i\frac{\Gamma_m}{4\pi}\right)\sum_{q\neq 0}\left(q+\frac{q}{|q|}\right)R_m^{|q|}e^{-iq\Theta_m}\epsilon_{k-q}\right]e^{ik\theta}\\ &= \sum_k\left[-i\sum_q\left(q+s_q\right)V_q\epsilon_{k-q}\right]e^{ik\theta}. \end{aligned}\tag{3.59}$$

Collecting terms of the same Fourier mode number k, we arrive at the following equation for the mode amplitudes:

$$\begin{aligned}\frac{d\epsilon_k}{dt} &= i2\pi s_k\epsilon_k + is_kV_k\\ &+2\pi i\sum_q \epsilon_q\epsilon_{k-q}(q-s_q+\frac{s_k}{2}) - ik\epsilon_k\sum_m\frac{\Gamma_m}{4\pi} - i\sum_q\epsilon_{k-q}(k+s_q)V_q.\end{aligned}\tag{3.60}$$

The first term on the right hand side of the above equation represents the restoring force for the oscillation of the k-th mode, the second term represents driving by the point vortices, the third term represents mode-mode coupling, and the fourth and the last terms represent nonlinear interactions between modes and the point vortices.

Equation (3.60) is correct to $O(\lambda^2)$. The nonlinear terms on the right hand side are of order λ^2 except when ϵ_0, the amplitude of the zeroth mode, is involved, in which case the nonlinear terms are of order λ^3 since $\epsilon_0 \sim O(\lambda^2)$ (Eq.(3.49)). Therefore the nonlinear terms with ϵ_0 involved should be discarded.

Integrals useful for deriving these results are listed in the appendix 2 at the end of this chapter.

3.5 Solutions

3.5.1 Kelvin Waves

If we set $\Gamma_m = 0$ for all of the point vortices, Eq.(3.60) becomes the mode equations for small disturbances on the circular patch. To the first order in the amplitude of the small disturbances, the equation for the k-th mode is

$$\frac{d\epsilon_k}{dt} = i2\pi s_k \epsilon_k, \tag{3.61}$$

and the solution is

$$\epsilon_k(t) = \epsilon_k(0)e^{2\pi i s_k t}, \tag{3.62}$$

where $\epsilon_k(0)$ is the initial amplitude of the mode. Therefore, a small disturbance on the circular patch evolves as

$$\epsilon(\theta, t) = \sum_k \epsilon_k(0)e^{i(k\theta + 2\pi s_k t)}, \tag{3.63}$$

which is the sum of the Kelvin waves. The phase velocity of the k-th Kelvin wave is

$$v_{phase} = -\frac{2\pi}{|k|}. \tag{3.64}$$

Therefore, in the rotating frame, all Kelvin waves rotate in the clockwise direction. Also notice that all Kelvin waves oscillate with a period equal to 1, which is the normalized rotation time of the rotating frame. This means that the small disturbance composed of Kelvin waves comes back to its initial shape with period 1, although in between the periods its shape changes due to the different phase velocities of the Kelvin waves.

3.5.2 Two Time Scale Analysis

As shown in Eqs.(3.45) and (3.46), the velocity of the m-th point vortex in the rotating frame is induced by other point vortices and the small disturbance $\epsilon(\theta, t)$ on the contour of the vortex patch, which are all quantities of order λ. Therefore, it takes a slow time scale of order $1/\lambda$ to move the point vortices over distances of order unity relative to the vortex patch. On the other hand, Eq.(3.44) shows that the modes on the contour of the vortex patch oscillate within a fast time scale of order unity. Clearly, there are two time scales in the dynamics of our model in the perturbation limit; therefore we need to solve the perturbed equations with two time scale analysis.

We first introduce the "slow time", defined as $\tau = \lambda t$, and accordingly call t as the "fast time". We then expand the dynamical variables in two time scale series:

$$\begin{aligned} \epsilon_k(t) &= \lambda \epsilon_k^{(1)}(t,\tau) + \lambda^2 \epsilon_k^{(2)}(t,\tau) + \cdots, & (3.65) \\ R_m(t) &= R_m^{(0)}(t,\tau) + \lambda R_m^{(1)}(t,\tau) + \cdots, & (3.66) \\ \Theta_m(t) &= \Theta_m^{(0)}(t,\tau) + \lambda \Theta_m^{(1)}(t,\tau) + \cdots, & (3.67) \end{aligned}$$

where $\epsilon_k^{(1)}$, $\epsilon_k^{(2)}$, $R_m^{(0)}$, $R_m^{(1)}$, $\Theta_m^{(0)}$ and $\Theta_m^{(1)}$ are functions of order of unity. Here $\epsilon_0^{(1)} = 0$, since ϵ_0 is of order λ^2 (see Eq.(3.49)). The time derivatives of these quantities are

$$\begin{aligned} \frac{d\epsilon_k}{dt} &= \lambda \frac{\partial \epsilon_k^{(1)}}{\partial t} + \lambda^2 \left(\frac{\partial \epsilon_k^{(1)}}{\partial \tau} + \frac{\partial \epsilon_k^{(2)}}{\partial t} \right) + \cdots, & (3.68) \\ \frac{dR_m}{dt} &= \frac{\partial R_m^{(0)}}{\partial t} + \lambda^2 \left(\frac{\partial R_m^{(0)}}{\partial \tau} + \frac{\partial R_m^{(1)}}{\partial t} \right) + \cdots, & (3.69) \\ \frac{d\Theta_m}{dt} &= \frac{\partial \Theta_m^{(0)}}{\partial t} + \lambda^2 \left(\frac{\partial \Theta_m^{(0)}}{\partial \tau} + \frac{\partial \Theta_m^{(1)}}{\partial t} \right) + \cdots. & (3.70) \end{aligned}$$

Substituting these two time scale series into the perturbation equations and collecting terms in the same order of λ, we obtain series of equations corresponding to the contributions from the terms of successively increasing order in λ. The slow time dependence of a quantity is determined in the next order equations by requiring that the sum of the resonant terms that drive unbounded fast time growth of the next order quantities should vanish (resonance condition).

For the point vortices, substitution of the two time scale series into the perturbation equations (3.45) and (3.46) yields the $O(\lambda^0)$ equations

$$\frac{\partial R_m^{(0)}}{\partial t} = 0, \qquad R_m^{(0)} \frac{\partial \Theta_m^{(0)}}{\partial t} = 0, \tag{3.71}$$

and the $O(\lambda)$ equations

$$\frac{\partial R_m^{(0)}}{\partial \tau} + \frac{\partial R_m^{(1)}}{\partial t} = A(\mathbf{R}_m^{(0)}) + C, \tag{3.72}$$

and

$$R_m^{(1)} \frac{\partial \Theta_m^{(0)}}{\partial t} + R_m^{(0)} \left(\frac{\partial \Theta_m^{(0)}}{\partial \tau} + \frac{\partial \Theta_m^{(1)}}{\partial t} \right) = B(\mathbf{R}_m^{(0)}) + D. \tag{3.73}$$

Here, $\mathbf{R}_m^{(0)} = (R_m^{(0)}, \Theta_m^{(0)})$ is the leading order approximation to the position of the m-th point vortex;

$$\lambda A(\mathbf{R}_m^{(0)}) = -\sum_{n, n\neq m} \left(\frac{\Gamma_n}{2\pi}\right) \frac{R_n^{(0)} \sin(\Theta_m^{(0)} - \Theta_n^{(0)})}{{R_m^{(0)}}^2 + {R_n^{(0)}}^2 - 2R_m^{(0)} R_n^{(0)} \cos(\Theta_m^{(0)} - \Theta_n^{(0)})} \tag{3.74}$$

and

$$\lambda B(\mathbf{R}_m^{(0)}) = \sum_{n, n\neq m} \left(\frac{\Gamma_n}{2\pi}\right) \frac{R_m^{(0)} - R_n^{(0)} \cos(\Theta_m^{(0)} - \Theta_n^{(0)})}{{R_m^{(0)}}^2 + {R_n^{(0)}}^2 - 2R_m^{(0)} R_n^{(0)} \cos(\Theta_m^{(0)} - \Theta_n^{(0)})} \tag{3.75}$$

are the leading order approximations to $V_r'(\mathbf{R}_m)$ and $V_\theta'(\mathbf{R}_m)$, respectively, and are the radial and azimuthal components of the velocity, induced by other point vortices at their leading order positions, on the m-th point vortex at its leading order position; and

$$\lambda C = \int_0^{2\pi} d\theta' \frac{2\lambda \epsilon^{(1)}(\theta', t, \tau) \sin(\theta' - \Theta_m^{(0)})}{1 + {R_m^{(0)}}^2 - 2R_m^{(0)} \cos(\theta' - \Theta_m^{(0)})}, \tag{3.76}$$

$$\lambda D = \int_0^{2\pi} d\theta' \frac{2\lambda \epsilon^{(1)}(\theta', t, \tau)(R_m^{(0)} - \cos(\theta' - \Theta_m^{(0)}))}{1 + {R_m^{(0)}}^2 - 2R_m^{(0)} \cos(\theta - \Theta_m^{(0)})} \tag{3.77}$$

are the leading order approximations to $u_r^{(1)}$ and $u_\theta^{(1)}$, respectively, and are the radial and azimuthal components of the velocity, induced by the vortex patch with the contour deformation described by

$$\lambda \epsilon^{(1)}(\theta, t, \tau) = \lambda \sum_{k\neq 0} \epsilon_k^{(1)}(t, \tau) e^{ik\theta}, \tag{3.78}$$

on the m-th point vortex in its leading order position.

For the contour of the background, substitution of the two time scale series into the perturbation equation (3.60) gives the $O(\lambda)$ equation

$$\frac{\partial \epsilon_k^{(1)}}{\partial t} = 2\pi i s_k \epsilon_k^{(1)} + i s_k V_k^{(1)}, \tag{3.79}$$

and the $O(\lambda^2)$ equation

$$\frac{\partial \epsilon_k^{(2)}}{\partial t} - 2\pi i s_k \epsilon_k^{(2)} = h_k, \tag{3.80}$$

where

$$\begin{aligned}h_k(t,\tau) \equiv & -\frac{\partial \epsilon_k^{(1)}}{\partial \tau} + is_k V_k^{(2)} \\ & +2\pi i \sum_q \epsilon_q^{(1)} \epsilon_{k-q}^{(1)} \left(q - s_q + \frac{s_k}{2} \right) \\ & -ik\epsilon_k^{(1)} \sum_m \frac{\Gamma_m}{4\pi\lambda} - i \sum_q \epsilon_{k-q}^{(1)} (k+s_q) V_q^{(1)} \end{aligned} \tag{3.81}$$

is a nonlinear forcing term, and

$$V_k^{(1)} = \sum_m \frac{\Gamma_m}{4\pi\lambda} R_m^{(0)|k|} e^{-ik\Theta_m^{(0)}}, \tag{3.82}$$

$$V_k^{(2)} = \sum_m \frac{\Gamma_m}{4\pi\lambda} R_m^{(0)|k|} e^{-ik\Theta_m^{(0)}} \left(\frac{|k| R_m^{(1)}}{R_m^{(0)}} - ik\Theta_m^{(1)} \right) \tag{3.83}$$

constitute the two time series for the quantity V_k:

$$V_k = \lambda V_k^{(1)} + \lambda^2 V_k^{(2)} + \cdots. \tag{3.84}$$

3.5.3 Leading Order Solutions in Fast Time Scale

In the leading order, the positions of the point vortices change according to Eq.(3.71). The solution is simply

$$R_m^{(0)} = R_m^{(0)}(\tau), \quad \Theta_m^{(0)} = \Theta_m^{(0)}(\tau), \tag{3.85}$$

which means that in the leading order, the point vortices are stationary in the rotating frame in the fast time scale, as we have discussed in the previous section.

In the leading order, the amplitudes of the modes of the vortex patch evolve according to Eq.(3.79). Since $V_k^{(1)}$ only depends on the leading order positions of the point vortices, which have no fast time dependence, the solution of the equation is

$$\epsilon_k^{(1)} = b_k(\tau) e^{2\pi i s_k t} - \frac{V_k^{(1)}}{2\pi}, \tag{3.86}$$

where $b_k(\tau)$ is the constant of integration that depends on slow time. Therefore,

$$\epsilon^{(1)}(\theta, t, \tau) = \beta(\theta, \tau) + \sum_{k \neq 0} b_k(\tau) e^{2\pi i s_k t}, \tag{3.87}$$

where

$$\begin{aligned}\beta(\theta,\tau) &= -\sum_{k\neq 0}\frac{V_k^{(1)}}{2\pi}e^{ik\theta} \\ &= \sum_m\left(\frac{\Gamma_m}{4\pi^2\lambda}\right)\frac{{R_m^{(0)}}^2 - R_m^{(0)}\cos(\theta-\Theta_m^{(0)})}{1+{R_m^{(0)}}^2-2R_m^{(0)}\cos(\theta-\Theta_m^{(0)})}. \end{aligned}\qquad (3.88)$$

Notice that $\lambda\beta(\theta,\tau)$ is the same as the image charge distribution induced by the point vortices at $\mathbf{R}_m^{(0)}$ on a circular free-slip boundary of radius 1. From Eq.(3.87) we see that in the leading order, the contour of the vortex patch consists of two parts: one part is $\beta(\theta,\tau)$, the "image charge", which is determined by the leading order positions of the point vortices; the other part is the free-streaming Kelvin waves which are not affected in fast time by the point vortices.

3.5.4 Leading Order Solutions in Slow Time Scale

The slow time evolution of the leading order approximations to the positions of the point vortices, $\mathbf{R}_m^{(0)}$, and the contour of the vortex patch, $\epsilon^{(1)}(\theta,t,\tau)$, must be determined with the resonant conditions in the next order equations, Eqs.(3.72), (3.73) and (3.80).

Substituting the leading order solutions Eqs.(3.85) and (3.87) into Eq.(3.72), we obtain

$$\frac{\partial R_m^{(1)}}{\partial t} = \left\{-\frac{dR_m^{(0)}}{d\tau} + A(\mathbf{R}_m^{(0)}) + C_\beta\right\} + \sum_{k\neq 0} 2\pi i s_k b_k(\tau) {R_m^{(0)}}^{|k|-1} e^{ik\Theta_m^{(0)}} e^{2\pi i s_k t}, \quad (3.89)$$

where C_β is obtained from replacing $\epsilon^{(1)}$ with its fast-time average β (see Eq.(3.87)) in the definition of C, Eq.(3.76), which yields

$$\lambda C_\beta = \int_0^{2\pi} d\theta' \frac{2\lambda\beta(\theta',\tau)\sin(\theta'-\Theta_m^{(0)})}{1+{R_m^{(0)}}^2 - 2R_m^{(0)}\cos(\theta'-\Theta_m^{(0)})}. \qquad (3.90)$$

The quantity λC_β is the radial component of the velocity on the point vortex due to the image charge part of the contour deformation of the vortex patch. Substituting the Fourier series of $\beta(\theta',\tau)$, Eq.(3.88), into the above equation and using the definition of $V_k^{(1)}$, Eq.(3.82), we obtain

$$\begin{aligned}\lambda C_\beta &= -\sum_{k\neq 0}\frac{\lambda V_k^{(1)}}{\pi}\int_0^{2\pi} d\theta' e^{ik\theta'}\frac{\sin(\theta'-\Theta_m^{(0)})}{1+R_m^{(0)2}-2R_m^{(0)}\cos(\theta'-\Theta_m^{(0)})}\\ &= -\sum_{k\neq 0} i\lambda\frac{k}{|k|}V_k^{(1)}e^{ik\Theta_m^{(0)}}R_m^{(0)|k|-1}\\ &= -\sum_n\left(-\frac{\Gamma_n}{2\pi}\right)\frac{\left(\frac{1}{R_n^{(0)}}\right)\sin(\Theta_m^{(0)}-\Theta_n^{(0)})}{\left(\frac{1}{R_n^{(0)}}\right)^2+R_m^{(0)2}-2\left(\frac{1}{R_n^{(0)}}\right)R_m^{(0)}\cos(\Theta_m^{(0)}-\Theta_n^{(0)})}.\end{aligned} \quad (3.91)$$

Comparing the above equation with Eq.(3.74), we find that λC_β is equivalent to the radial velocity induced by point vortices with circulations $-\Gamma_n$ and positions $\mathbf{R}_n^{(0)}/R_n^{(0)}$ $(n=1,...,M)$, which are the image point vortices that would arise if the point vortices in our model at their leading order positions were enclosed by a free-slip circular boundary of radius 1.

Quantities in the curly bracket in Eq.(3.89) depends only on the slow time. They must add up to zero; otherwise the solution for $R_m^{(1)}$ will have a term that is linear in t, and will grow unbounded in the fast time scale. Therefore, we have

$$\frac{dR_m^{(0)}}{d\tau} = A(\mathbf{R}_m^{(0)}) + C_\beta, \quad (3.92)$$

and

$$R_m^{(1)} = \sum_{k\neq 0} b_k(\tau)R_m^{(0)|k|-1}e^{ik\Theta_m^{(0)}}e^{2\pi i s_k t} + c_m(\tau), \quad (3.93)$$

where $c_m(\tau)$ is a constant of integration.

Similarly, substituting the leading order solutions Eqs.(3.85) and (3.87) into Eq.(3.73), we obtain

$$R_m^{(0)}\frac{d\Theta_m^{(0)}}{d\tau} = B(\mathbf{R}_m^{(0)}) + D_\beta, \quad (3.94)$$

and

$$\Theta_m^{(1)} = \sum_{k\neq 0} i s_k b_k(\tau)R_m^{(0)|k|-2}e^{ik\Theta_m^{(0)}}e^{2\pi i s_k t} + d_m(\tau), \quad (3.95)$$

where $d_m(\tau)$ is a constant of integration, and D_β is obtained by replacing $\epsilon^{(1)}$ by β in Eq.(3.77):

$$\lambda D_\beta = \int_0^{2\pi} d\theta' \frac{2\lambda\beta(\theta', \tau)(R_m^{(0)} - \cos(\theta' - \Theta_m^{(0)}))}{1 + {R_m^{(0)}}^2 - 2R_m^{(0)}\cos(\theta - \Theta_m^{(0)})}. \tag{3.96}$$

The quantity λD_β is the azimuthal component of the velocity of the point vortex due to the image charge part of the contour deformation of the vortex patch. Substituting the Fourier series of $\beta(\theta', \tau)$, Eq.(3.88), into the above equation and using the definition of $V_k^{(1)}$, Eq.(3.82), we obtain

$$\begin{aligned} \lambda D_\beta &= -\sum_{k \neq 0} \frac{\lambda V_k^{(1)}}{\pi} \int_0^{2\pi} d\theta' e^{ik\theta'} \frac{R_m^{(0)} - \cos(\theta' - \Theta_m^{(0)})}{1 + {R_m^{(0)}}^2 - 2R_m^{(0)}\cos(\theta' - \Theta_m^{(0)})} \\ &= \sum_{k \neq 0} \lambda V_k^{(1)} e^{ik\Theta_m^{(0)}} {R_m^{(0)}}^{|k|-1} \\ &= \sum_n \left(-\frac{\Gamma_n}{2\pi}\right) \frac{R_m^{(0)} - \left(\frac{1}{R_n^{(0)}}\right)\cos(\Theta_m^{(0)} - \Theta_n^{(0)})}{{R_m^{(0)}}^2 + \left(\frac{1}{R_n^{(0)}}\right)^2 - 2R_m^{(0)}\left(\frac{1}{R_n^{(0)}}\right)\cos(\Theta_m^{(0)} - \Theta_n^{(0)})}. \end{aligned} \tag{3.97}$$

Comparing the above equation with Eq.(3.75), we find that λD_β is equivalent to the azimuthal velocity induced by the image vortices, as in the case for λC_β.

Equations (3.92) and (3.94) show that the leading order positions of the point vortices evolve in the rotating frame in the slow time scale with the velocity induced by other point vortices at their leading order positions and the image charge part of the contour deformation of the vortex patch. Therefore, the leading order dynamics of the point vortices is the same as that of the point vortices under a circular free-slip boundary with the radius equal to that of the vortex patch. Also, equations (3.93) and (3.95) show that the free-streaming Kelvin waves excite oscillations of the point vortices in fast time scale with period 1 around their leading order motions.

To test this conclusion, we have compared the leading order solutions with the results of a contour dynamics simulation[58] for the case of $M = 2$ and $\Gamma_1 = \Gamma_2 = 0.05 \times 4\pi = 0.2\pi$ (*i.e.* $\lambda = 0.05$), initially placed at $\mathbf{R}_1 = (0.2, 0)$ and $\mathbf{R}_2 = (0.4, \pi)$. The evolution of the radial position of the first point vortex is

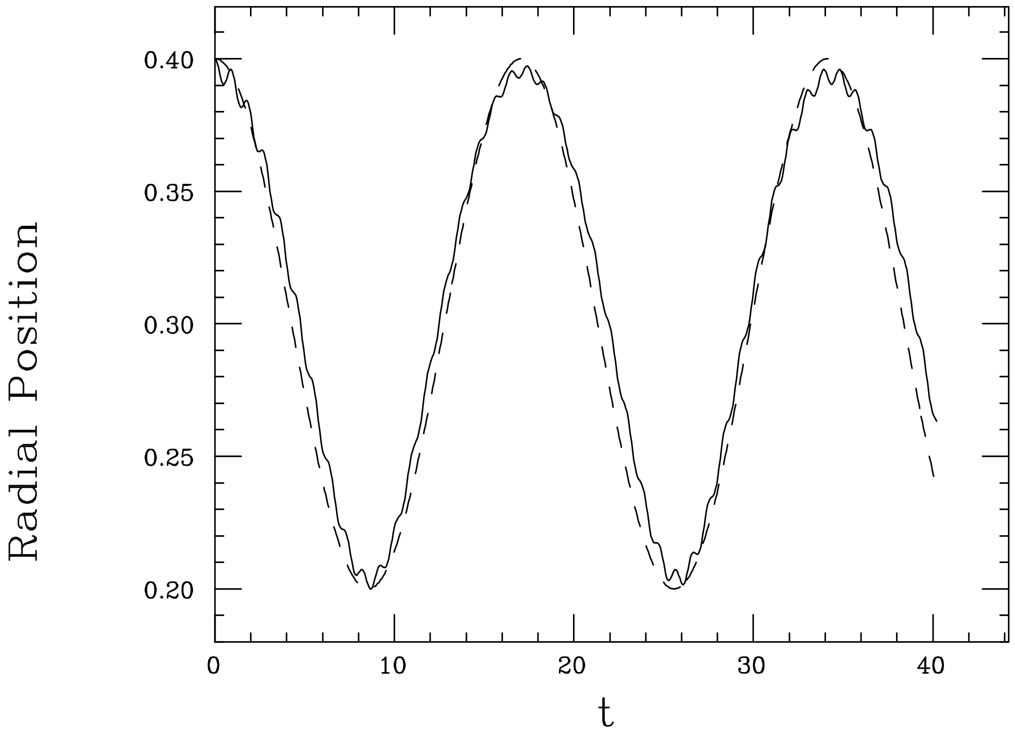

Figure 3.1: Time evolution of the radial positions one of the two point vortices, initially placed at $\mathbf{R}_1 = (0.4, \pi)$ and $\mathbf{R}_2 = (0.2, 0)$. The unit of time is the rotation period of the unperturbed circular patch, and that of the length is the radius of the unperturbed circular patch. The circulations of the point vortices are $\Gamma_1 = \Gamma_2 = 0.2\pi$ (*i.e.* $\lambda = 0.05$). The dotted line is the result of the leading order solutions. The solid line is the result of the contour dynamics, in which the shape of the vortex patch is initially circular. At $t = 40.22$, the contour of the vortex patch filaments.

plotted in Fig.3.1. As shown in the figure, the leading order solution agrees well with the result of the contour dynamics.

The difference between the leading order solution and the result of the contour dynamics is of order $\lambda = 0.05$, and has two features that can be understood from the solutions of the $R_m^{(1)}$ and $\Theta_m^{(1)}$, Eqs.(3.93) and (3.95). First, there is a fast time scale oscillation with period 1. This comes from the terms involving the free-streaming Kelvin waves in Eqs.(3.93) and (3.95). Second, there is a deviation that evolves in slow time scale. This comes from the constants of integration $c_m(\tau)$ and

$d_m(\tau)$ in Eqs.(3.93) and (3.95). The slow time evolutions of these quantities can not be determined by the perturbative calculations that we have carried out so far. To determine them, the two time scale analysis must be carried on further, which is quite complicated.

The equivalence of the dynamics of the point vortices with the classical problem of point vortex inside circular free-slip boundary enables us to apply all of the results in the classical problem to our model. For example, we know the equilibrium patterns of the point vortices and their stabilities from the works of Havelock[46], Campbell and Ziff[47], and others. We also know that the dynamics of the point vortices is Hamiltonian and in general chaotic[53].

The slow time evolution of the image charge part of the contour deformation is simply determined by the leading order positions of the point vortices, as in Eq.(3.88). The slow time evolution of the Kelvin waves, on the other hand, is obtained by the resonant condition of the second order term $\epsilon_k^{(2)}$ in Eq.(3.80). Since the right hand side of the equation, h_k, does not depends on $\epsilon_k^{(2)}$, we have

$$\epsilon_k^{(2)} = e^{2\pi i s_k t} \int_0^t dt' h_k(t', \tau) e^{-2\pi i s_k t'} + f_k(\tau) e^{2\pi i s_k t}, \tag{3.98}$$

where $f_k(\tau)$ is the constant of integration. Furthermore, since the fast time behavior of h_k is determined by $\epsilon^{(1)}$, $R_m^{(1)}$ and $\Theta_m^{(1)}$, which are all periodic functions of the fast time t with period 1, we can express h_k in terms of the Fourier transformation

$$h_k = \sum_n \hat{h}_k(n, \tau) e^{2\pi i n t}, \tag{3.99}$$

where the n-th Fourier coefficient is defined as

$$\hat{h}_k(n, \tau) = \int_0^1 dt h_k(t, \tau) e^{-2\pi i n t}. \tag{3.100}$$

Substituting this transformation into Eq.(3.98), we find that

$$\epsilon_k^{(2)} = e^{2\pi i s_k t} \hat{h}_k(s_k, \tau) t + e^{2\pi i s_k t} \sum_{n \neq s_k} \frac{\hat{h}_k(n, \tau)(e^{2\pi i (n - s_k) t} - 1)}{2\pi i (n - s_k)} + f_k(\tau) e^{2\pi i s_k t}. \tag{3.101}$$

To avoid the unbounded growth of $\epsilon_k^{(2)}$ in fast time, we need

$$\hat{h}_k(s_k, \tau) = 0, \tag{3.102}$$

or in other words, the resonant driving term in Eq.(3.80) must vanish.

Substituting Eq.(3.81) along with Eqs.(3.82) and (3.83) into Eq.(3.100), and using Eqs.(3.86), (3.93) and (3.95), we find that the above resonant condition leads to the slow time evolution equations for the amplitudes of the Kelvin waves:

$$\frac{db_k}{d\tau} = ik \sum_{q,kq>0} W_{k,q} b_q, \tag{3.103}$$

where the coupling matrix $W_{k,q}$ is defined as

$$W_{k,q} = \sum_m \frac{\Gamma_m}{2\pi\lambda} \left(R_m^{(0)}{}^{|k|+|q|-2} - R_m^{(0)}{}^{|k-q|} \right) e^{i(q-k)\Theta_m^{(0)}}. \tag{3.104}$$

The details of the derivation is in appendix 3 at end of this chapter. Notice that in Eq.(3.103), only modes with the same sign of wave numbers are coupled. The form of $W_{k,q}$ cab be understood by examining the forcing term h_k, defined in Eq.(3.81). There are three interactions: interaction between the Kelvin waves and the oscillations of the point vortices, the interaction between the Kelvin waves and the image charge part, and the interaction between the Kelvin waves with other Kelvin waves. The first interaction contributes to the first term in Eq.(3.104), and the second interaction contributes to the second term in Eq.(3.104). The third interaction does not contribute to the resonant condition, since the sum of the oscillation frequencies of two Kelvin waves does not equal to the oscillation frequency of any other Kelvin waves.

A conserved quantity can be derived from the mode equations. From Eq.(3.104) we see that $W_{k,q}^* = W_{q,k}$. Therefore, it is easy to verify with Eq.(3.103) that

$$\frac{d}{d\tau}\left(\sum_k \frac{|b_k|^2}{|k|}\right) = \sum_k \left(\frac{b_k^*}{|k|}\frac{db_k}{d\tau} + \frac{b_k}{|k|}\frac{db_k^*}{d\tau} \right) = 0. \tag{3.105}$$

Hence, the sum $\sum_k |b_k|^2/|k|$ is a conserved quantity. We can prove that this sum multiplied by a constant $8\pi^3\lambda^2$ is the self-energy of the Kelvin waves in the rotating frame (see appendix 4 at the end of the chapter). The conservation of this quantity is not surprising. In the rotating frame, the fast-time averaged energy of the system, which is conserved in the slow time scale, is the sum of the interaction energy between the point vortices, the interaction energy between the point vortices and the image charge part, the self-energy of the image charge part, and the self-energy of the Kelvin waves. All these energies are of order λ^2. Furthermore, since in slow time scale the dynamics of the point vortices in the rotating frame under the influence of the image charge part is the same as if they are subject to a circular free-slip boundary, the fast-time averaged energy of the sub-system consisting of the point vortices and the image charge part is conserved. Therefore, the fast-time averaged self-energy of the Kelvin waves in the rotating frame is conserved in the slow time scale.

Equation(3.103) describes the slow time evolution of the amplitudes of the Kelvin waves. With the image charge part slaved by the position of the point vortices, the leading order solution for the contour deformation is completely determined. To verify that this solution is indeed correct, we again compare with contour dynamics. In particular, we study the evolution of the contour for the case of $M = 1, \Gamma_1 = 0.05 \times 4\pi = 0.2\pi$ $(i.e.\lambda = 0.05)$. Initially, the point vortex is placed at $\mathbf{R}_1 = (0.5, 0)$, and the initial shape of the contour is circular. The leading order motion of the point vortex is quite simple, since the point vortex is moving in the rotating frame only under the influence of its own image charge. The radial position $R_1^{(0)}$ of the point vortex does not change, but its angular position increases in slow time as

$$\Theta_1^{(0)} = \frac{2\tau}{1 - R_1^{(0)2}}. \tag{3.106}$$

With the position of the point vortex known, the image charge part β is determined by Eq.(3.88). The evolution of the Kelvin waves are then calculated by evaluating the mode amplitudes, Eqs.(3.103), up to $k = \pm 80$. With the image charge part and the amplitude of the Kelvin waves known, the leading order evolution of the contour of the vortex patch is obtained by Eq.(3.87). We plot the results in the rotating frame in which the point vortex is stationary in the leading order approximation. The comparison with the result of the contour dynamics is quite good at early times, as shown in Fig.3.2. However, at late times the contour of the

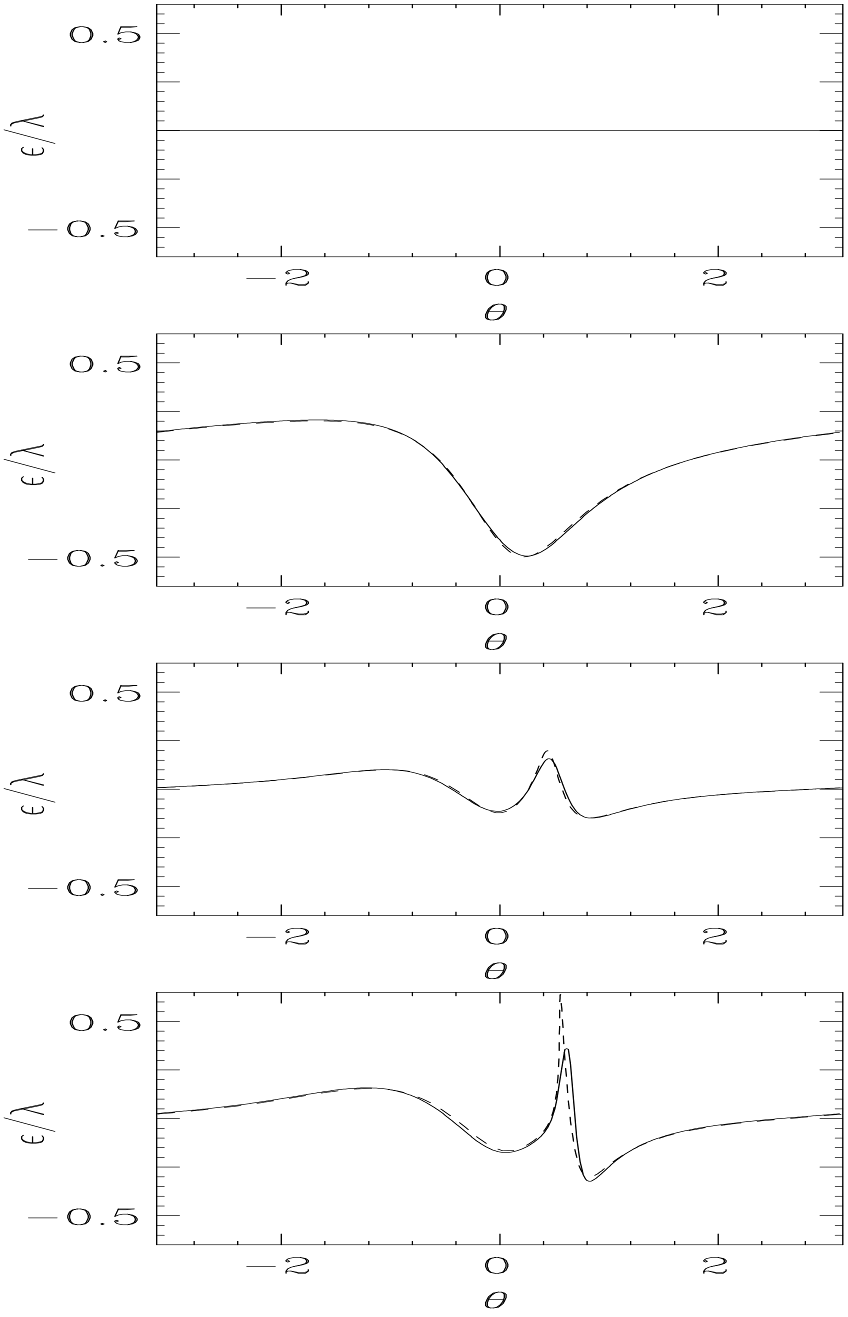

Figure 3.2: The evolution of the contour of the vortex patch for the case of one point vortex with circulation $\Gamma_1 = 0.2\pi$ (*i.e.* $\lambda = 0.05$) placed at $\mathbf{R}_1 = (0.5, 0)$. The deviation ϵ from the initial circular shape is plotted at $t = 0, 0.3, 3$, and 6. The dotted lines are the results of the contour dynamics. The solid lines are the results of the mode equations with $-80 \leq k \leq 80$.

vortex patch steepens and the approximations used in our analysis break down. This is discussed in detail in the next section.

3.5.5 Filamentation

If the leading order solutions obtained above are valid for all time, the point vortices, placed at some arbitrary positions initially, can never settle down to an equilibrium pattern, since they follow the dynamics of the point vortices inside a circular free-slip boundary, which is Hamiltonian and in general chaotic. However, for some initial positions of the point vortices, the contour of the vortex patch evolves into a shape that violates the assumptions of the perturbation limit, as seen in Fig.3.2. Subsequently, strong nonlinearity takes over and the contour filaments, leading to the breakdown of the leading order solutions. Depending on the positions of the point vortices, filamentation can take place in fast or slow time scales.

The fast time scale filamentation happens when some of the point vortices are very close to the boundary of the vortex patch. In this case, the image charge part of the contour deformation, $\lambda\beta(\theta,\tau)$, can be very large. We can estimate the maximum of $|\lambda\beta|$ from the contribution of the point vortex, denoted as the m-th point vortex, that is closest to the boundary of the vortex patch. Let Γ_m and $(R_m^{(0)}, \Theta_m^{(0)})$ be its circulation and leading order position, respectively, then its contribution to $\lambda\beta$, as evident from Eq.(3.88), is

$$\frac{\Gamma_m ({R_m^{(0)}}^2 - R_m^{(0)} \cos(\theta - \Theta_m^{(0)}))}{4\pi^2 (1 + {R_m^{(0)}}^2 - 2R_m^{(0)} \cos(\theta - \Theta_m^{(0)}))}. \tag{3.107}$$

The maximum of the absolute value of the above quantity is

$$\frac{\Gamma_m R_m^{(0)}}{4\pi^2 (1 - R_m^{(0)})}. \tag{3.108}$$

Therefore, if

$$\frac{R_m^{(0)}}{1 - R_m^{(0)}} \sim \lambda^{-\xi}, \qquad \text{or} \qquad R_m^{(0)} \sim 1 - \lambda^{\xi}, \tag{3.109}$$

where $\xi > 0$ is a constant, then the maximum of $\lambda\beta$ is of order $\lambda^{1-\xi} \gg \lambda$ since $\lambda \ll 1$. In this case, the contour deformation, which is the sum of the Kelvin waves and the image charge part, will develop a maximum deformation of order $\lambda^{1-\xi}$ within one rotation time of the vortex patch, although initially the deformation is of order λ. As a consequence, the assumption of the perturbation limit will break down within one rotation time of the vortex patch, leading to fast time scale filamentation of the contour. Equation (3.109) is the criterion for onset of the fast time scale filamentation.

We can estimate the value of the constant ξ with contour dynamics simulations for the simple case of one point vortex placed in a initially circular vortex patch. For a given circulation $\Gamma_1 = 4\pi\lambda$, the position of the point vortex, R_1, for which the contour of the vortex patch filaments at $t = 1 \pm 0.02$, is obtained. From several values of λ and the corresponding values of R_1, we find that $\xi \approx 0.566$, as shown in Fig.3.3.

If none of the point vortices is close enough to the edge of the vortex patch, the contour does not filament on the fast time scale. However, it can still filament on the slow time scale. To investigate this possibility, we study the evolution of the "envelope" of the Kelvin waves, defined as

$$\chi(\theta, \tau) = \sum_{k\neq 0} b_k(\tau) e^{ik\theta}. \tag{3.110}$$

The evolution of this envelope function is determined by the mode equations of the Kelvin waves, Eq.(3.103).

The filamentation of the Kelvin waves in the slow time scale is tied to the development of a singularity in the envelope function from a smooth initial condition. Since $\sum_k |b_k|^2/|k|$ is conserved, mode amplitudes of the Kelvin waves can not grow unbounded; therefore, the only way of developing a singularity in $\chi(\theta, \tau)$ is to excite high k modes and form a large gradient.

We argue that the nature of the singularity formation in χ is the same as that in the "pseudo-envelope" $\chi'(\theta, \tau)$, which evolves according to the following

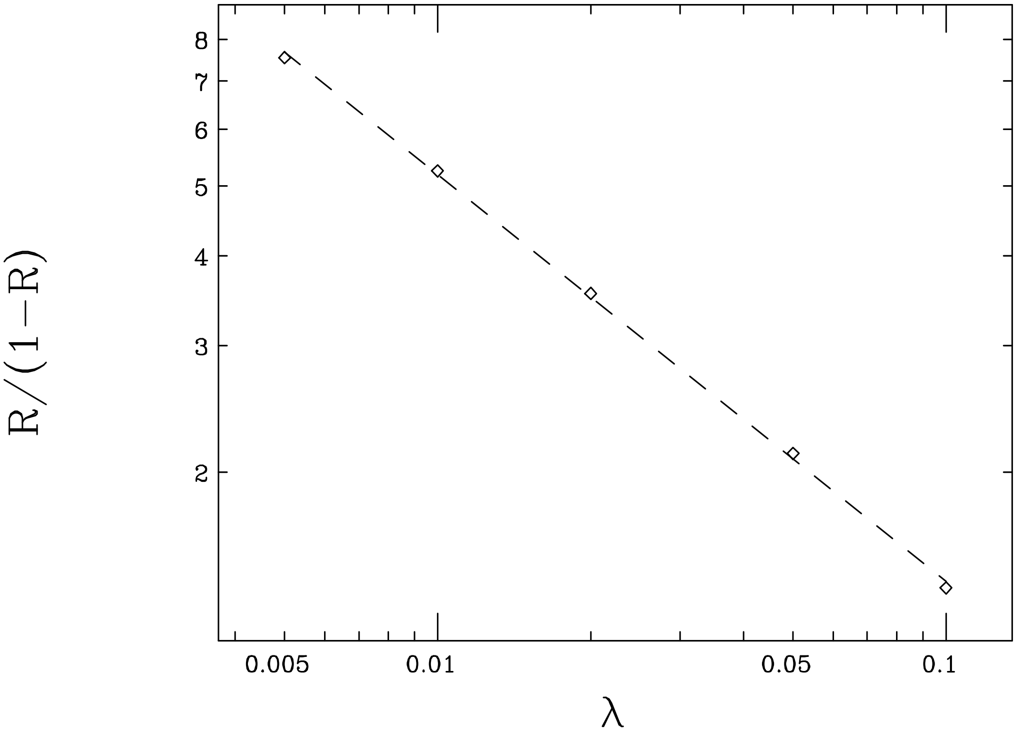

Figure 3.3: The relation between λ and $R/(1-R)$, where R is the radial position of the point vortex at which the initially circular contour of the vortex patch filaments at $t = 1 \pm 0.02$. The dotted line, which has a slope -0.566, is the best fit to the data.

simple differential equation:

$$\frac{\partial \chi'}{\partial \tau} + 2\left(U(\theta,\tau) - \sum_m \frac{\Gamma_m}{4\pi\lambda}\right)\frac{\partial \chi'}{\partial \theta} = 0, \tag{3.111}$$

where U is obtained from Eq.(3.30) by replacing the positions of the point vortices with their leading order values, *i.e.*

$$U(\theta,\tau) = \sum_m \frac{\Gamma_m(1 - R_m^{(0)}\cos(\theta - \Theta_m^{(0)}))}{2\pi\lambda(1 + R_m^{(0)2} - 2R_m^{(0)}\cos(\theta - \Theta_m^{(0)}))}. \tag{3.112}$$

The pseudo-envelope can be decomposed into Fourier modes:

$$\chi'(\theta,\tau) = \sum_k b_k'(\tau)e^{ik\theta}, \tag{3.113}$$

where b_k' is the amplitude of the k-th mode. From Eq.(3.111) we obtain

$$\frac{db_k'}{d\tau} = i\sum_q W_{k,q}' b_q', \tag{3.114}$$

where

$$W_{k,q}' = -\sum_m q\frac{\Gamma_m}{2\pi\lambda} R_m^{(0)|k-q|} e^{i(q-k)\Theta_m^{(0)}}. \tag{3.115}$$

The mode equations (3.114) are different from the mode equations (3.103), therefore, the details of the pseudo-envelope χ', described by Eq.(3.111), is different from the envelope χ for the Kelvin waves, described by mode equations (3.103). However, for $|k| \gg 1$, since $R_m^{(0)} < 1$, we have

$$W_{k,q}' = -k\sum_m \frac{q}{k}\frac{\Gamma_m}{2\pi\lambda} R_m^{(0)|k-q|} e^{i(q-k)\Theta_m^{(0)}} \approx \left\{ \begin{array}{ccc} kW_{k,q} & , & kq > 0 \\ 0 & , & kq < 0 \end{array} \right. . \tag{3.116}$$

Furthermore, in both cases modes are coupled most effectively only to nearby modes, *i.e.* $|q-k|$ must be small, hence the high $|k|$ modes are not effectively coupled to the low $|k|$ modes, which presumably behave quite differently for χ' and χ since $W_{k,q}'$ are quite different from $kW_{k,q}$ for small $|k|$. Therefore, high $|k|$ modes are excited in the same way in both χ and χ', and we can understand the development of singularity in χ by studying the behavior of χ', which is much simpler.

To illustrate these points, we numerically integrate the mode equations for χ, Eq.(3.103), and the mode equations for $\chi^{'}$, Eq.(3.114). The calculation is again for the case of one point vortex with $\Gamma_1 = 0.05 \times 4\pi = 0.2\pi$ placed at $\mathbf{R}_1 = (0.5, 0)$ in an initially circular vortex patch. We plot in Fig.3.4.a and Fig.3.4.b χ and $\chi^{'}$ at $t = 6$, right before the contour filaments, in the rotating frame in which the point vortex is stationary. As can be seen in the figures, the overall shapes of χ and $\chi^{'}$ are different. However, the way and the place that the singularity forms are quite similar. The similarity is more obvious if we plot only the high k mode contributions to χ and $\chi^{'}$. In Fig.3.4.c and Fig.3.4.d, we plot the parts of χ and $\chi^{'}$ that include only modes with $|k| \geq 30$. As can be seen in the figures, although the absolute values are different, the two curves are very similar in shape.

Equation (3.111) is amenable to the method of characteristics. Consider a point on the pseudo-envelope at angle θ. As the pseudo-envelope evolves, this point moves to another position at angle $\theta(\tau)$ and amplitude $\chi^{'}(\theta(\tau), \tau)$. Therefore, setting

$$\frac{d\theta}{d\tau} = 2\left(U(\theta, \tau) - \sum_m \frac{\Gamma_m}{4\pi\lambda}\right), \tag{3.117}$$

we get

$$\frac{d\chi^{'}}{d\tau} = \frac{\partial\chi^{'}}{\partial\tau} + \frac{\partial\chi^{'}}{\partial\theta}\frac{d\theta}{d\tau} = 0. \tag{3.118}$$

Equations (3.117) and (3.118) are differential equations that describe how a point on the pseudo-envelope moves.

We observe from Eq.(3.118) that the value of $\chi^{'}$ on a pseudo-envelope point remains constant for all time. Therefore, the singularity can form only if the pseudo-envelope points converge within arbitrarily small distances, which makes the gradient of the pseudo-envelope with respect to the angle very large. If the angular distance $\delta\theta(\tau)$ between two pseudo-envelope points, originally separated by a distance $\delta\theta_0$ of order unity, come close to each other within a distance of order $\delta\theta_0\lambda^{\eta}$, where $\eta > 0$ is a constant, then the gradient of the pseudo-envelope will be amplified by a factor of order $\lambda/\lambda^{\eta} = \lambda^{1-\eta} \gg \lambda$ since $\lambda \ll 1$. At this point, the pseudo-envelope is not smooth, and a singularity forms. Equation (3.117) shows

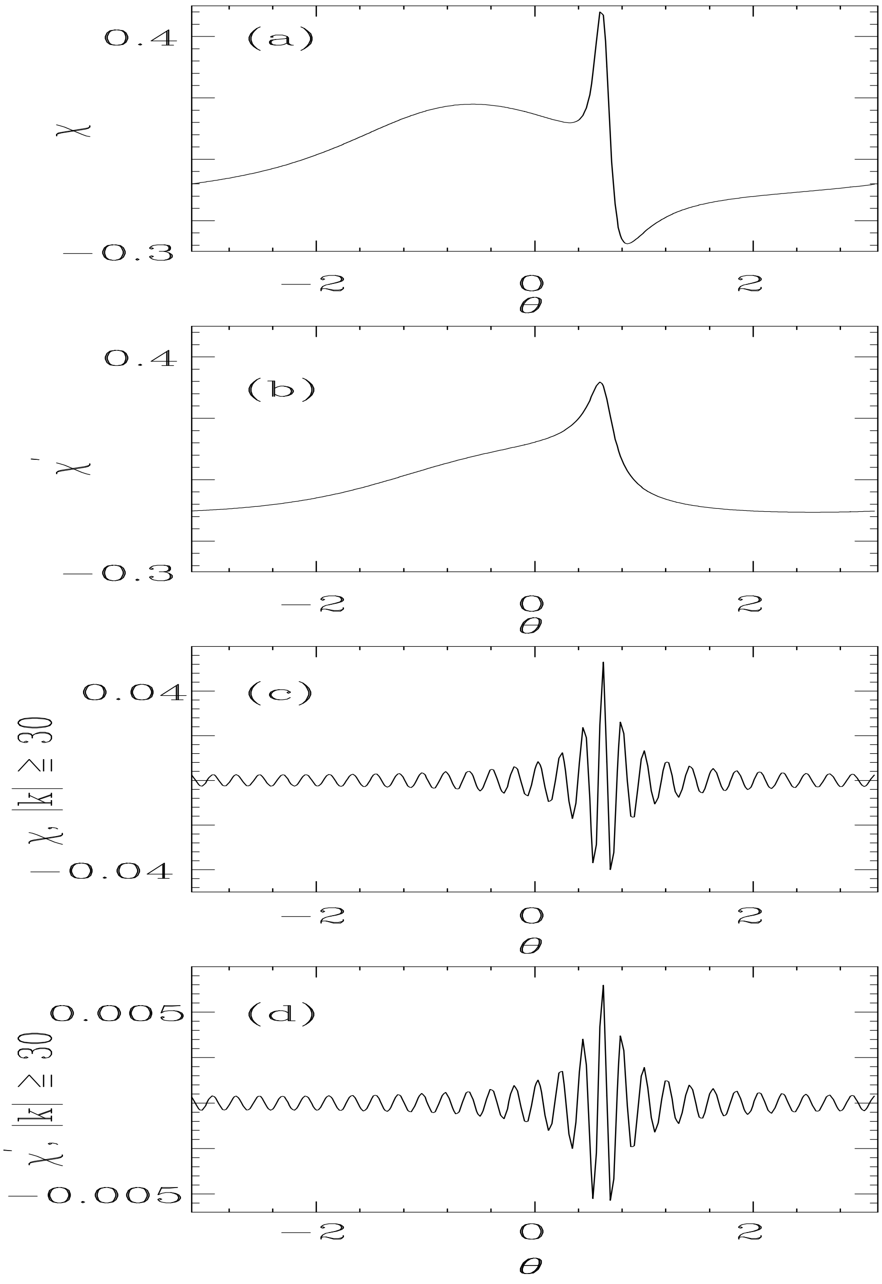

Figure 3.4: Comparison of $\chi(\theta,t)$ and $\chi'(\theta,t)$ at $t=6$ for the case of one point vortex with $\Gamma_1 = 0.2\pi$ ($i.e. \lambda = 0.05$) placed at $\mathbf{R}_1 = (0.5, 0)$. Initially the vortex patch is circular. Mode equations with $-80 \leq k \leq 80$ are integrated. (a) χ; (b) χ'; (c) Part of χ that only include contributions from modes with $|k| \geq 30$; (d) Part of χ' that only include contributions from modes with $|k| \geq 30$.

that the angular position of a point on the pseudo-envelope evolves according to a first order differential equation in slow time. Therefore, when two points on the pseudo-envelope converge, their angular distance can only decrease exponentially in slow time. Therefore, the time τ_B at which the singularity forms on the pseudo-envelope can be estimated as follows:

$$\delta\theta(\tau) \approx \delta\theta_0 e^{-\gamma\tau_B} \approx \delta\theta_0 \lambda^{\eta}, \tag{3.119}$$

or equivalently,

$$t_B \equiv \frac{\tau_B}{\lambda} \approx \frac{\eta}{\gamma}\lambda^{-1}\ln\lambda^{-1}. \tag{3.120}$$

Here γ is a constant, determined from the characteristics of Eq.(3.117) and depends on the dynamics of the point vortices.

Since the nature of singularity formation in χ is the same as that in χ', τ_B or t_B is also the time at which the singularity forms in χ. At this point, our perturbation solution for the Kelvin waves breaks down, and strong nonlinearity takes over. We can assume that filamentation follows very quickly after this point, since the gradient is already high, and strong nonlinear interaction occurs. Therefore, τ_B or t_B is also the filamentation time for the Kelvin waves in our model.

The constant η is an exponent that measures the strength of the nonlinearity needed for the break down of the perturbation equations. Since its role is similar to that of the exponent ξ we have discussed for the case of fast time scale filamentation (see the discussion that follows Eq.(3.109)), we assume that $\eta \approx \xi = 0.566$. Note that the value of η is not important for the scaling of t_B with λ.

To show that the above approach is useful for understanding the slow time scale filamentation of the Kelvin waves, we present two simple examples. In both examples, we study the formation of singularity in the pseudo-envelopes, and infer from the results the nature of filamentation of the Kelvin waves.

The first example is the case of one point vortex with circulation $\Gamma_1 = 4\pi\lambda$ placed at radial position R. The leading order solution of the point vortex is very simple, as we have shown in the previous section: the radial position of the point vortex does not change, *i.e.*, $R_1^{(0)}(\tau) = R$, and its angular position is given by Eq.(3.106). With the motion of the point vortex known, the equation of for the points on the pseudo-envelope, Eq.(3.117), becomes

$$\frac{d\theta}{d\tau} = \frac{2(1-R^2)}{1+R^2-2R\cos(\theta-\Omega\tau)}, \tag{3.121}$$

where

$$\Omega = \frac{2}{1-R^2} \tag{3.122}$$

is the angular velocity of the rotation of the point vortex in slow time in the rotating frame. Defining $\theta = \theta' + \Omega\tau$, Eq.(3.121) becomes

$$\frac{d\theta'}{d\tau} = -\Omega + \frac{2(1-R^2)}{1+R^2-2R\cos(\theta')}. \tag{3.123}$$

The fixed points of the above equation is given by $d\theta'/d\tau = 0$, and the solution is

$$\cos(\theta'_{fix}) = \frac{R(3-R^2)}{2}, \tag{3.124}$$

where θ'_{fix} denotes the angular position of the fixed point. It is easy to see that for all $0 < R < 1$, the right hand side of the above equation is always positive and smaller than 1. Therefore, the equation always has two fixed points, one is in between 0 and $\pi/2$, the other is in between $3\pi/2$ and 2π. To see the behavior of the pseudo-envelope points nearby the fixed points, we Taylor expand the right hand side of Eq.(3.123) near the fixed point and get

$$\frac{d(\theta' - \theta'_{fix})}{d\tau} = -\gamma(\theta' - \theta'_{fix}), \tag{3.125}$$

where

$$\gamma = \frac{4R\sin(\theta'_{fix})}{(1-R^2)^3}. \tag{3.126}$$

Therefore,

$$\theta'(\tau) - \theta'_{fix} = (\theta'_0 - \theta'_{fix})e^{-\gamma\tau}, \tag{3.127}$$

where θ'_0 is the initial position of the boundary point. For the fixed point in between 0 and $\pi/2$, Eq.(3.126) shows that $\gamma > 0$; therefore, the boundary points nearby will converge to this fixed point exponentially in time. This fixed point is the stable fixed point. For the other fixed point, which is in between $3\pi/2$ and 2π, Eq.(3.126) shows that $\gamma < 0$, therefore, this fixed point is unstable.

These results indicate that for the case of one point vortex placed off the center of the vortex patch, there is always one boundary point to which the other boundary points converge exponentially in slow time. Therefore, the perturbation solutions always break down in finite time t_B. We can estimate t_B using Eqs.(3.120), (3.126), and (3.124):

$$t_B \approx \frac{\eta}{\gamma}\lambda^{-1}\ln\lambda^{-1} = \frac{\eta(1-R^2)^2}{2R\sqrt{4-R^2}}\lambda^{-1}\ln\lambda^{-1}. \tag{3.128}$$

From the equation above we see that when R is small, *i.e.* the point vortex is nearby the center of the vortex patch, it takes long time to filament the Kelvin waves; on the other hand, when R approaches 1, *i.e.* the point vortex approaches the boundary of the vortex patch, the filamentation time is small.

We have tested Eq.(3.128), which is inferred from the singularity formation in the pseudo-envelope, with contour dynamics simulations. In the simulations, a point vortex is placed at R and the initial shape of the vortex patch is circular. In Fig.3.5, we plot the dependence of the filamentation time in the simulations with $R = 0.5$ on λ. The figure shows that the $\lambda^{-1}\ln\lambda^{-1}$ scaling of t_B in Eq.(3.128) is well satisfied. In Fig.3.6, we plot the dependence of the filamentation time in the simulations with $\lambda = 0.05$ (*i.e.* the circulation of the point vortex is $\Gamma_1 = 0.2\pi$) on the position R of the point vortex. The figure shows that Eq.(3.128) agrees qualitatively with the results of the contour dynamics.

The second example is the case of two point vortices, with circulations $\Gamma_1 = \Gamma_2 = 4\pi\lambda$, initially placed at $(R, 0)$ and (R, π). Evaluating Eqs.(3.92) and (3.94) for this case, we find that the leading order solution of the positions of the point vortices are given by

$$R_1^{(0)} = R, \quad R_2^{(0)} = R \tag{3.129}$$

$$\Theta_1^{(0)} = \Omega\tau, \quad \Theta_2^{(0)} = \pi + \Omega\tau, \tag{3.130}$$

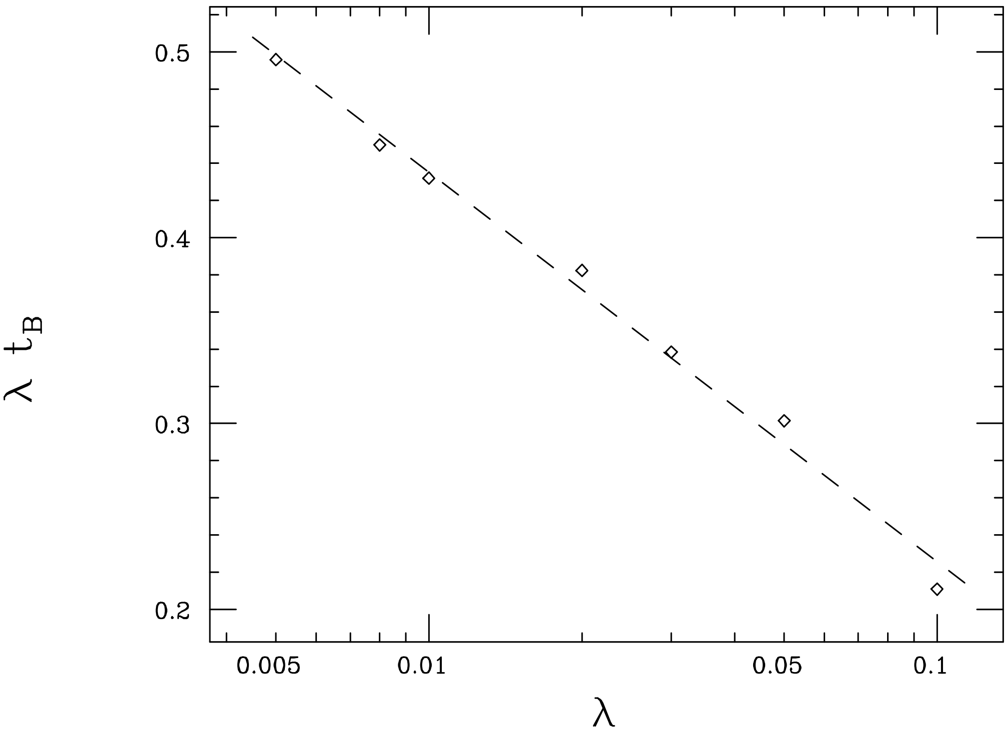

Figure 3.5: The dependence of the filamentation time t_B on λ. Initially, the point vortex is at $\mathbf{R}_1 = (0.5, 0)$, and the contour of the vortex patch is circular. The dotted line, which is for visual guide, has a slope -1.

where

$$\Omega = \frac{1+3R^4}{R^2(1-R^4)}. \tag{3.131}$$

In other words, the point vortices are in equilibrium in the rotating frame with angular frequency $2\pi + \lambda\Omega$. Therefore, the equation of motion for the envelope points, Eq.(3.117), becomes

$$\frac{d\theta'}{d\tau} = -\Omega + \frac{4(1-R^4)}{(1+R^2)^2 - 4R^2\cos^2(\theta')}, \tag{3.132}$$

where $\theta' = \theta - \Omega\tau$. The fixed point of the above equation is given by

$$\cos^2(\theta'_{fix}) = \frac{(1+R^2)^2}{4R^2} - \frac{(1-R^4)^2}{1+3R^4}. \tag{3.133}$$

For $1 > R > R_c = 0.44$, there are four solutions for θ_{fix}, two of which are stable fixed points. As in the previous example, Taylor expansion of the right hand side

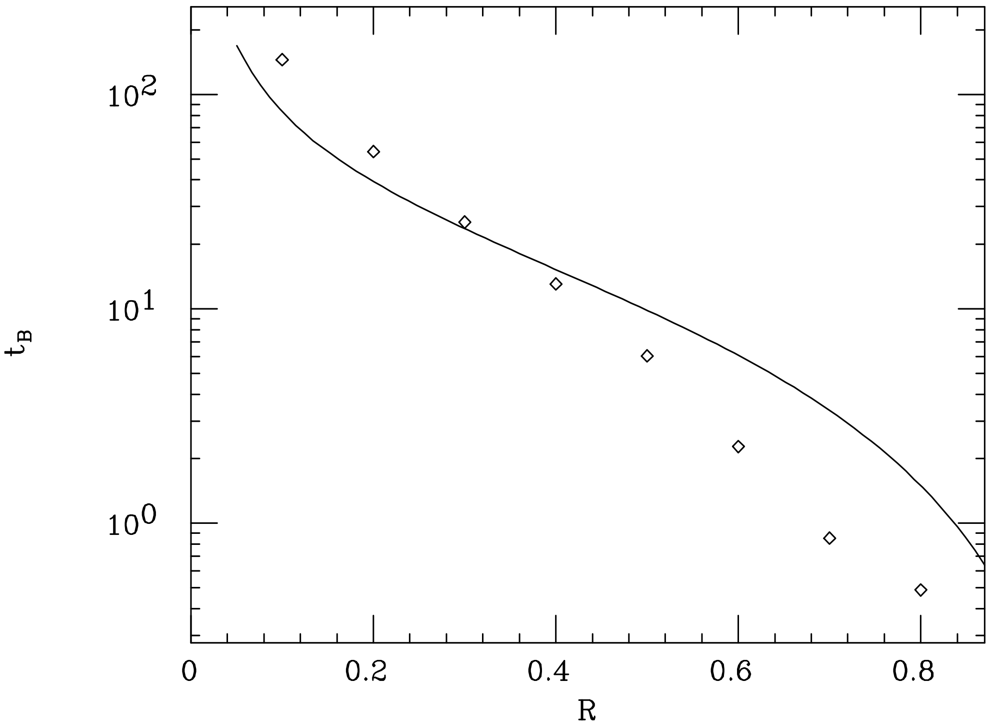

Figure 3.6: The dependence of the filamentation time t_B on the position R of the point vortex. The point vortex has a circulation $\Gamma_1 = 0.05 \times 4\pi = 0.2\pi$, and is placed initially at $\mathbf{R}_1 = (0.5, 0)$ in a circular vortex patch. The symbol ($\diamond$) indicates the results of the contour dynamics simulation, and the solid line is the prediction inferred from the evolution of the pseudo-envelope, Eq.(3.128).

of Eq.(3.132) near the stable fixed points reveals exponential convergence of the pseudo-envelope points to the fixed points with

$$\gamma = \frac{16R^2(1-R^4)\sin(2\theta'_{fix})}{\left[(1+R^2)^2 - 4R^2\cos^2(2\theta'_{fix})\right]^2}. \tag{3.134}$$

Because of symmetry, γ is the same for the two stable fixed points. As in the previous example, the pseudo-envelope develops singularity at time t_B, which can be inferred as the time at which the Kelvin waves filament. We can estimate t_B using Eqs.(3.120), (3.134) and (3.133):

$$t_B \approx \frac{\eta}{\gamma}\lambda^{-1}\ln\lambda^{-1}$$

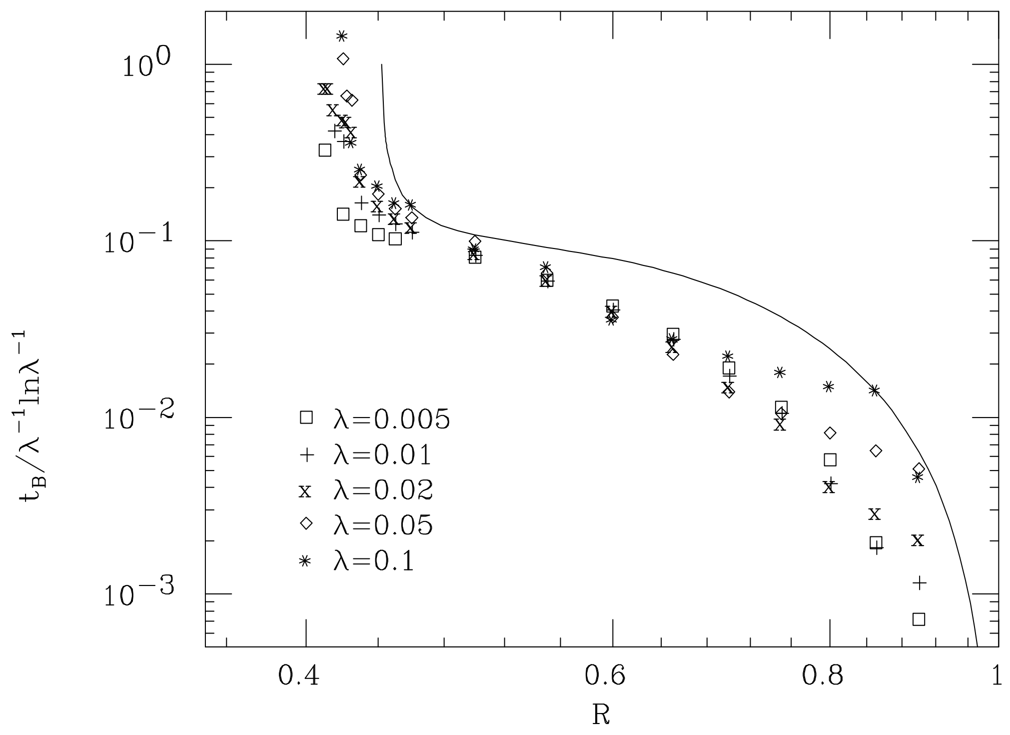

Figure 3.7: Dependence of filamentation time t_B on R for the case of two point vortices with equal circulations $4\pi\lambda$ initially placed at $\mathbf{R}_1 = (R, 0)$ and $\mathbf{R}_2 = (R, \pi)$. The shape of the vortex patch is initially circular. The data for five values of λ are presented by the symbols, with t_B scaled by $\lambda^{-1}\ln\lambda^{-1}$. The solid line is the prediction inferred from the evolution of the pseudo-envelope, Eq.(3.135), scaled by $\lambda^{-1}\ln\lambda^{-1}$.

$$= \frac{2\eta(1-R^4)^2R^4\lambda^{-1}\ln\lambda^{-1}}{(1+3R^4)\sqrt{(-1+4R^2+5R^4+4R^6)(1-4R^2+11R^4-4R^6)}} \tag{3.135}$$

For $R < R_c$, there is no solution for θ'_{fix}, and, therefore, there is no fixed point for the pseudo-envelope points to converge to. This suggests that the slow time scale filamentation of the Kelvin waves is suppressed for $R < R_c$.

Contour dynamics is again used to verify these results. In Fig.3.7 we have plotted the results of contour dynamics for the dependence of the filamentation time, scaled by a factor of $\lambda^{-1}\ln\lambda^{-1}$, on R for several λ. The initial shape of the contour is circular. As we can see, the $\lambda^{-1}\ln\lambda^{-1}$ scaling of t_B, suggested by

Eq.(3.135), works quite well for $R < 0.7$, as indicated by the coincidence of the scaled filamentation times for different values of λ. For $R > 0.7$, the scaling does not work well for relatively large λ. This is because as R goes close to the edge of the vortex patch, the fast time filamentation, as discussed in the beginning of this section, takes over, and the Kelvin waves filament within one rotation of the vortex patch. For $R < R_c$, the filamentation times increase dramatically as R decrease, indicating the suppression of the slow time filamentation of small R. The dependence of t_B on R agrees qualitatively with the formula given by Eq.(3.135), as in the first example.

The two examples we have discussed above show that dynamics of the slow time filamentation of the Kelvin waves can be understood from the singularity formation in the pseudo-envelope χ'. These examples confirm that the filamentation of the Kelvin waves happens due to the excitation of high k modes, and the filamentation time t_B scales with λ as shown in Eq.(3.120). They also show that dependence of t_B on the dynamics of the point vortices can be qualitatively deduced from the dynamics of χ'.

The use of the pseudo-envelopes greatly simplifies the study of the slow time scale filamentation of the Kelvin waves. However, when the point vortices are in generic positions, the analysis of the slow time filamentation of the Kelvin waves becomes quite complicated since the dynamics of the point vortices are chaotic in most cases. So far, we have not been able to work out the conditions for slow time filamentation for the most general initial positions of the point vortices. Contour dynamics simulations seem to suggest that the slow time filamentation of the Kelvin waves in the most general cases resembles that of a single point vortex placed off the center of the vortex patch, as studied in the first example. Also, the suppression of the slow time filamentation when the point vortices are clustered near the center of the vortex patch, as studied in the second example, seems to hold in general. These numerical results should be investigated more fully in future studies.

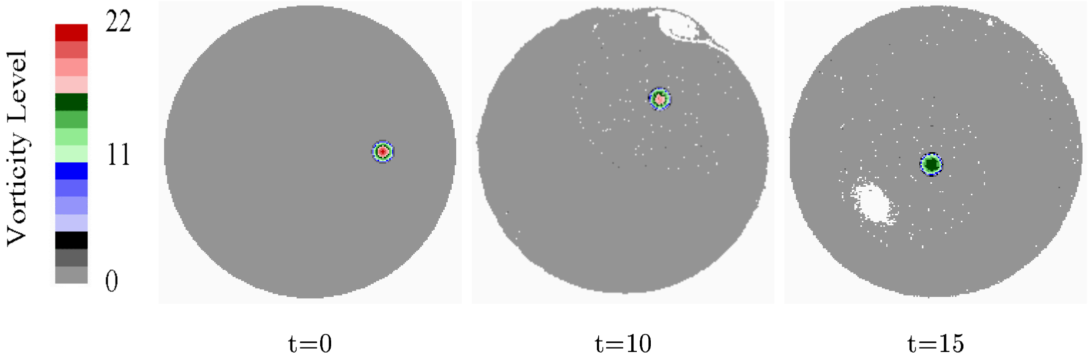

Figure 3.8: Vortex-in-cell simulation for one Gaussian vortex placed inside a vortex patch. The perturbation strength λ of the vortex is 0.0335. (a) Initial flow. The vortex is placed at the half-way to the edge of the vortex patch, and the vortex patch is circular. (b) Flow at $t = 10$ (in the unit of the rotation period of the vortex patch). Filamentation of the vortex patch is observed. (c) Flow at $t = 15$. A hole is introduced into the vortex patch.

The dynamics of the model after the filamentation of the contour of the vortex patch is beyond the scope of our analysis. To qualitatively understand the nature of the dynamics beyond filamentation, we have performed a vortex-in-cell simulation[51], in which a Gaussian vortex with a perturbation strength $\lambda = 0.0335$ is initially placed at half of the radius of a circular vortex patch, as shown in Fig.3.8.a. [2] The simulation shows that the contour vortex patch is repeatedly filamented, as can be seen in Fig.3.8.b, and the filaments introduce holes into the vortex patch that create chaotic mixing of the vorticity with the void, as can be seen in Fig.3.8.c. The simulation suggests that the dynamics of the model beyond filamentation is chaotic and mixing. This supports the idea of the regional maximum fluid entropy theory for vortex crystal formation, in which the chaotic mixing of the background flow is essential.

---

[2] The flow in the simulation is not the same as the flow of the model we have studied so far, since in the simulation the vortex is not a point vortex and the flow is subject to a free slip circular boundary with a radius 2.5 times that of the vortex patch. Nevertheless, the qualitative behavior of flow in the simulation is the same as that of the flow of the model, since the Gaussian vortex has a small radius and the circular boundary is far away from the flow.

3.6 Appendix 1

In this appendix, we prove Eq.(3.27). Remembering that $\mathbf{r}_c^{'} = (r_c^{'}, \theta^{'})$, $\mathbf{r}_c = (r_c, \theta)$, $r_c^{'} = 1 + \epsilon(\theta^{'}, t) = 1 + \epsilon^{'}$, and $r_c = 1 + \epsilon(\theta, t) = 1 + \epsilon$, we find that

$$\begin{aligned}
& \ln \frac{|\mathbf{r}_c^{'} - \mathbf{r}_c|^2}{2(1 - \cos(\theta' - \theta))} \\
= \;& \ln \frac{r_c^2 + r_c^{'2} - 2 r_c r_c^{'} \cos(\theta^{'} - \theta)}{2(1 - \cos(\theta' - \theta))} \\
= \;& \ln \left[1 + (\epsilon + \epsilon^{'}) + \frac{\epsilon^2 + \epsilon^{'2} - 2\epsilon\epsilon^{'} \cos(\theta^{'} - \theta)}{2(1 - \cos(\theta' - \theta))} \right]. \qquad (3.136)
\end{aligned}$$

The third term in the last bracket in the equation above is of order ϵ^2 for all $\theta^{'}$ excluding the isolated point $\theta^{'} = \theta$. (Remember that both $\epsilon^{'}$, $\frac{\partial \epsilon^{'}}{\partial \theta'}$, ϵ, and $\frac{\partial \epsilon}{\partial \theta}$ are of order λ.) This is easy to see except when $\theta^{'} \to \theta$, since the denominator of the term becomes singular. However, we can show that

$$\begin{aligned}
& \lim_{\theta' \to \theta} \frac{\epsilon^2 + \epsilon^{'2} - 2\epsilon\epsilon^{'} \cos(\theta^{'} - \theta)}{2(1 - \cos(\theta' - \theta))} \\
= \;& \lim_{\theta' \to \theta} \frac{2\epsilon^{'} \frac{\partial \epsilon^{'}}{\partial \theta'} - 2\epsilon \frac{\partial \epsilon^{'}}{\partial \theta'} \cos(\theta^{'} - \theta) + 2\epsilon\epsilon^{'} \sin(\theta^{'} - \theta)}{2 \sin(\theta' - \theta)} \\
= \;& \epsilon^2 + \lim_{\theta' \to \theta} \frac{\partial \epsilon^{'}}{\partial \theta'} \cdot \frac{\epsilon^{'} - \epsilon \cos(\theta^{'} - \theta)}{\sin(\theta' - \theta)} \\
= \;& \epsilon^2 + \frac{\partial \epsilon}{\partial \theta} \cdot \lim_{\theta' \to \theta} \frac{\epsilon^{'} - \epsilon \cos(\theta^{'} - \theta)}{\sin(\theta' - \theta)} \\
= \;& \epsilon^2 + \frac{\partial \epsilon}{\partial \theta} \cdot \lim_{\theta' \to \theta} \frac{\frac{\partial \epsilon^{'}}{\partial \theta'} - \epsilon \sin(\theta^{'} - \theta)}{\cos(\theta' - \theta)} \\
= \;& \epsilon^2 + \left(\frac{\partial \epsilon}{\partial \theta} \right)^2 \sim O(\lambda^2), \qquad (3.137)
\end{aligned}$$

using the L'Hospital's rule. Therefore we can Taylor expand Eq.(3.136) correct to the second order as follows:

$$\begin{aligned}
& \ln \frac{|\mathbf{r}_c^{'} - \mathbf{r}_c|^2}{2(1 - \cos(\theta' - \theta))} \qquad (3.138) \\
= \;& \ln \left[1 + (\epsilon + \epsilon^{'}) + \frac{\epsilon^2 + \epsilon^{'2} - 2\epsilon\epsilon^{'} \cos(\theta^{'} - \theta)}{2(1 - \cos(\theta' - \theta))} \right]
\end{aligned}$$

$$
\begin{aligned}
&= (\epsilon+\epsilon') - \frac{1}{2}(\epsilon+\epsilon')^2 + \frac{\epsilon^2+\epsilon'^2-2\epsilon\epsilon'\cos(\theta'-\theta)}{2(1-\cos(\theta'-\theta))} + O(\lambda^3) \\
&= (\epsilon+\epsilon') + \frac{(\epsilon'^2+\epsilon^2)\cos(\theta'-\theta)-2\epsilon'\epsilon}{2(1-\cos(\theta'-\theta))} + O(\lambda^3). \qquad (3.139)
\end{aligned}
$$

The above equation can be rewritten as

$$
\ln|\mathbf{r}_c' - \mathbf{r}_c|^2 = \ln[2(1-\cos(\theta'-\theta))] + (\epsilon'+\epsilon) + \frac{(\epsilon'^2+\epsilon^2)\cos(\theta'-\theta)-2\epsilon'\epsilon}{2(1-\cos(\theta'-\theta))} + O(\lambda^3), \qquad (3.140)
$$

which is Eq.(3.27).

3.7 Appendix 2

The following are the useful integrals in deriving the mode equations. For $0 \le a < 1$ and integer k, we have

$$
\int_{-\pi}^{\pi} dx e^{-ikx} \frac{1-a\cos x}{1+a^2-2a\cos x} = \begin{cases} \pi a^{|k|} & , \quad k \neq 0 \\ 2\pi & , \quad k = 0 \end{cases} . \qquad (3.141)
$$

For $0 \le a < 1$ and non-zero integer k, we have

$$
\int_{-\pi}^{\pi} dx e^{-ikx} \cot\frac{x}{2} = -i2\pi\frac{k}{|k|}, \qquad (3.142)
$$

$$
\int_{-\pi}^{\pi} dx e^{-ikx} \frac{\sin x}{1+a^2-2a\cos x} = -i\pi\frac{k}{|k|}a^{|k|-1}, \qquad (3.143)
$$

$$
\int_{-\pi}^{\pi} dx e^{-ikx} \frac{a-\cos x}{1+a^2-2a\cos x} = -\pi a^{|k|-1}, \qquad (3.144)
$$

and

$$
\int_{-\pi}^{\pi} dx e^{-ikx} \frac{\sin x(1-a\cos x)}{(1+a^2-2a\cos x)^2} = -i\pi\frac{k}{|k|}a^{|k|-1}\frac{1+|k|}{2}. \qquad (3.145)
$$

3.8 Appendix 3

In this appendix, we derive Eq.(3.103), which is equivalent to Eq.(3.102). Here we only derive for the case $k > 0$. The derivation for $k < 0$ is similar.

Since $k > 0$, we have $s_k = 1$. Therefore, we obtain

$$\hat{h}_k(s_k, \tau) = \hat{h}_k(1, \tau) = \int_0^1 dt h_k(t, \tau) e^{-2\pi i t}, \tag{3.146}$$

using the definition of $\hat{h}_k(n, \tau)$, Eq.(3.100). Substituting the definition of $h_k(t, \tau)$, Eq.(3.81), into above equation, we obtain

$$\hat{h}_k(1, \tau) = I_1 + I_2 + I_3 + I_4 + I_5, \tag{3.147}$$

where I_1, I_2, I_3, I_4, and I_5 are five integrals arising from the five terms in the definition of $\hat{h}_k(n, \tau)$. In the following, we calculate these integrals.

With Eqs.(3.86), (3.82) and (3.85), we obtain

$$\begin{aligned} I_1 &\equiv -\int_0^1 dt \frac{\partial \epsilon_k^{(1)}}{\partial \tau} e^{-2\pi i t} \\ &= -\int_0^1 dt \left(\frac{d b_k(\tau)}{d\tau} e^{2\pi i t} - \frac{1}{2\pi} \frac{d V_k^{(1)}(\tau)}{d\tau} \right) e^{-2\pi i t} \\ &= -\frac{d b_k(\tau)}{d\tau}. \end{aligned} \tag{3.148}$$

With Eqs.(3.83), (3.85), (3.93), and (3.95), we have

$$\begin{aligned} I_2 &\equiv i \int_0^1 dt V_k^{(2)} e^{-2\pi i t} \\ &= i \int_0^1 dt \sum_m \frac{\Gamma_m}{4\pi\lambda} R_m^{(0)\,k} e^{-ik\Theta_m^{(0)}} \left(\frac{k R_m^{(1)}}{R_m^{(0)}} - ik\Theta_m^{(1)} \right) e^{-2\pi i t} \\ &= i \int_0^1 dt \sum_m \frac{\Gamma_m}{4\pi\lambda} R_m^{(0)\,k} e^{-ik\Theta_m^{(0)}} \left[\frac{k}{R_m^{(0)}} \left(\sum_{q\neq 0} b_q(\tau) R_m^{(0)\,|q|-1} e^{iq\Theta_m^{(0)}} e^{2\pi i s_q t} + c_m(\tau) \right) \right. \\ &\left. -ik \left(\sum_{q\neq 0} i s_q b_q(\tau) R_m^{(0)\,|q|-2} e^{iq\Theta_m^{(0)}} e^{2\pi i s_q t} + d_m(\tau) \right) \right] e^{-2\pi i t} \\ &= i2k \sum_{q, q>0} b_q(\tau) \left(\sum_m \frac{\Gamma_m}{4\pi\lambda} R_m^{(0)\,k+q-2} e^{i(q-k)\Theta_m^{(0)}} \right). \end{aligned} \tag{3.149}$$

The non-vanishing contributions to this integral come from the interaction between the fast-time oscillation of the point vortices and the Kelvin waves.

With Eq.(3.86), we obtain

$$I_3 \equiv 2\pi i \int_0^1 dt \sum_q \epsilon_q^{(1)} \epsilon_{k-q}^{(1)} \left(q - s_q + \frac{1}{2} \right) e^{-2\pi i t}$$

$$
\begin{aligned}
&= 2\pi i \int_0^1 dt \sum_q \left(q - s_q + \frac{1}{2}\right)\left(b_q(\tau)e^{2\pi i s_q t} - \frac{V_q^{(1)}}{2\pi}\right) && (3.150)\\
&\left(b_{k-q}(\tau)e^{2\pi i s_{k-q} t} - \frac{V_{k-q}^{(1)}}{2\pi}\right) e^{-2\pi i t} &&\\
&= -i \sum_{q,q>0} \left(q - 1 + \frac{1}{2}\right) V_{k-q}^{(1)} b_q(\tau) &&\\
&\quad -i \sum_{q,k-q>0} \left(q - s_q + \frac{1}{2}\right) V_q^{(1)} b_{k-q}(\tau) &&\\
&= -i \sum_{q,q>0,q\neq k} (k - s_{k-q}) V_{k-q}^{(1)} b_q(\tau). && (3.151)
\end{aligned}
$$

The non-vanishing contributions to this integral come from the interaction between the image charge part and the Kelvin waves. The interaction between Kelvin waves do not contribute, since

$$
s_q + s_{k-q} = \begin{cases} 2 & , \quad q > 0, (k-q) > 0 \\ 0 & , \quad q(k-q) < 0 \end{cases} \tag{3.152}
$$

can never equal to 1. In other words, the interaction between two Kelvin waves does not resonate with another Kelvin wave.

With Eq.(3.86), we have

$$
\begin{aligned}
I_4 &\equiv -ik \int_0^1 dt \epsilon_k^{(1)} \sum_m \frac{\Gamma_m}{4\pi\lambda} e^{-2\pi i t} &&\\
&= -ik \sum_m \frac{\Gamma_m}{4\pi\lambda} \int_0^1 dt \left(b_k(\tau)e^{2\pi i t} - \frac{V_k^{(1)}}{2\pi}\right) e^{-2\pi i t} &&\\
&= -ik b_k(\tau) \sum_m \frac{\Gamma_m}{4\pi\lambda}. && (3.153)
\end{aligned}
$$

Finally, with Eq.(3.86), we obtain

$$
\begin{aligned}
I_5 &\equiv -i \int_0^1 dt \sum_q \epsilon_{k-q}^{(1)} (k + s_q) V_q^{(1)} e^{-2\pi i t} &&\\
&= -i \int_0^1 dt \sum_q (k + s_q) V_q^{(1)} \left(b_{k-q}(\tau)e^{2\pi i t} - \frac{V_{k-q}^{(1)}}{2\pi}\right) e^{-2\pi i t} &&\\
&= -ik b_k(\tau) \sum_m \frac{\Gamma_m}{4\pi\lambda} - i \sum_{q,q>0,q\neq k} b_q (k + s_{k-q}) V_{k-q}^{(1)}. && (3.154)
\end{aligned}
$$

Combining the results for I_1, I_2, I_3, I_4, and I_5 with Eqs.(3.147) and (3.102), we obtain Eq.(3.103).

3.9 Appendix 4

Here we prove that the sum $8\pi^3\lambda^2\sum_k |b_k|^2/|k|$ is the self-energy of the Kelvin waves in the rotating frame.

We first derive the angular momentum L_0 and energy H_0 of the unperturbed circular patch. It is easy to see that

$$L_0 = -\frac{1}{2}\int_{D_0} d\mathbf{r}^2 4\pi r^2 = -\frac{1}{2}\int_0^{2\pi} d\theta \int_0^1 dr 4\pi r^3 = -\pi^2, \tag{3.155}$$

where D_0 denotes the region inside the circular patch. The stream function ψ_0 of the unperturbed vortex patch is

$$\begin{aligned}\psi_0(\mathbf{r}) &= \int_{D_0} d\mathbf{r}^2 4\pi G(\mathbf{r}-\mathbf{r}^{'}) \\ &= -\int_0^{2\pi} d\theta^{'} \int_0^1 dr^{'} r^{'} \ln\left(r^2 + r^{'2} - 2rr^{'}\cos(\theta-\theta^{'})\right) \\ &= \begin{cases} \pi(1-r^2) & , \quad \mathbf{r} \text{ inside the circular patch} \\ -2\pi\ln r & , \quad \mathbf{r} \text{ outside the circular vortex patch} \end{cases} \end{aligned} \tag{3.156}$$

where the Green's function $G(\mathbf{r}-\mathbf{r}^{'})$ is defined in Eq.(3.9). Therefore, the energy of the circular patch is

$$H_0 = \frac{1}{2}\int_{D_0} d\mathbf{r}^2 4\pi\psi_0 = \frac{1}{2}\int_0^{2\pi} d\theta \int_0^1 dr 4\pi r\pi(1-r^2) = \pi^3. \tag{3.157}$$

We now derive the angular momentum L of the perturbed patch with the contour specified as in Eq.(3.23). We denote D as the region inside the the perturbed patch. We have

$$\begin{aligned} L &= -\frac{1}{2}\int_D d\mathbf{r}^2 4\pi r^2 \\ &= -\frac{1}{2}\int_0^{2\pi} d\theta \int_0^{1+\epsilon} dr 4\pi r^3 \\ &= -\pi^2 - 2\pi\int_0^{2\pi} d\theta\epsilon - 3\pi\int_0^{2\pi} d\theta\epsilon^2 + O(\lambda^3) \\ &= L_0 - 2\pi\int_0^{2\pi} d\theta\epsilon^2 + O(\lambda^3), \end{aligned} \tag{3.158}$$

where we have used Eq.(3.34). Therefore, the angular momentum L_ϵ due to the contour deformation is

$$L_\epsilon = L - L_0 = -2\pi\int_0^{2\pi} d\theta\epsilon^2 = -4\pi^2\sum_{k\neq 0}|\epsilon_k|^2 \tag{3.159}$$

correct to $O(\lambda^2)$. In the last step, the Fourier series of ϵ, Eq.(3.47) is used.

The stream function $\psi(\mathbf{r})$ of the perturbed patch can again be expressed in terms of the Green's function, Eq.(3.9):

$$\begin{aligned}\psi(\mathbf{r}) &= \int_D d\mathbf{r}^2 4\pi G(\mathbf{r}-\mathbf{r}^{'}) \\ &= -\int_0^{2\pi} d\theta^{'} \int_0^{1+\epsilon^{'}} dr^{'} r^{'} \ln\left(r^2 + r^{'2} - 2rr^{'}\cos(\theta-\theta^{'})\right). \end{aligned} \tag{3.160}$$

Therefore, the energy H of the perturbed patch is

$$\begin{aligned} H &= \frac{1}{2}\int_D d\mathbf{r}^2 4\pi\psi(\mathbf{r}) \\ &= -2\pi\int_0^{2\pi} d\theta \int_0^{2\pi} d\theta^{'} \int_0^{1+\epsilon} dr \int_0^{1+\epsilon^{'}} dr^{'} r r^{'} \\ &\quad \cdot \ln\left(r^2 + r^{'2} - 2rr^{'}\cos(\theta-\theta^{'})\right). \end{aligned} \tag{3.161}$$

To evaluate the above integral, we define

$$I(\epsilon,\epsilon^{'}) \equiv \int_0^{1+\epsilon} dr \int_0^{1+\epsilon^{'}} dr^{'} r r^{'} \ln\left(r^2 + r^{'2} - 2rr^{'}\cos(\theta-\theta^{'})\right). \tag{3.162}$$

Taylor expansion of $I(\epsilon,\epsilon^{'})$ gives

$$I(\epsilon,\epsilon^{'}) = I(0,0) + I_1\epsilon + I_2\epsilon^{'} + \frac{1}{2}I_{11}\epsilon^2 + I_{12}\epsilon\epsilon^{'} + \frac{1}{2}I_{22}\epsilon^{'2} + O(\lambda^3), \tag{3.163}$$

where

$$\begin{aligned} I_1 &= \frac{\partial I}{\partial\epsilon}(0,0) = I_2 = \frac{\partial I}{\partial\epsilon^{'}}(0,0) \\ &= \int_0^1 dr^{'} r^{'} \ln\left(1 + r^{'2} - 2r^{'}\cos(\theta-\theta^{'})\right), \end{aligned} \tag{3.164}$$

$$\begin{aligned} I_{11} &= \frac{\partial^2 I}{\partial\epsilon^2}(0,0) = I_{22} = \frac{\partial^2 I}{\partial\epsilon^{'2}}(0,0) \\ &= I_1 + \int_0^1 dr^{'} \frac{2r^{'}\left(1 - r^{'}\cos(\theta-\theta^{'})\right)}{1 + r^{'2} - 2r^{'}\cos(\theta-\theta^{'})}, \end{aligned} \tag{3.165}$$

and

$$I_{12} = \frac{\partial^2 I}{\partial\epsilon\partial\epsilon^{'}}(0,0) = \ln(2 - 2\cos(\theta-\theta^{'})). \tag{3.166}$$

Since

$$-2\pi\int_0^{2\pi}d\theta\int_0^{2\pi}d\theta^{'}I(0,0)=2\pi\int_0^{2\pi}d\theta\int_0^{1}drr\psi_0(r)=H_0, \tag{3.167}$$

and

$$\begin{aligned} -\quad & 2\pi\int_0^{2\pi}d\theta\int_0^{2\pi}d\theta^{'}\epsilon I_1=-2\pi\int_0^{2\pi}d\theta\int_0^{2\pi}d\theta^{'}\epsilon^{'}I_2 \qquad (3.168)\\ = \quad & -2\pi\int_0^{2\pi}d\theta\epsilon\psi_0(r=1)=0, \end{aligned}$$

(because $\psi_0(r=1)=0$), as well as

$$\begin{aligned} -\quad & 2\pi\int_0^{2\pi}d\theta\int_0^{2\pi}d\theta^{'}\frac{\epsilon^2}{2}I_{11}=-2\pi\int_0^{2\pi}d\theta\int_0^{2\pi}d\theta^{'}\frac{\epsilon^{'2}}{2}I_{22}\\ = \quad & \pi\int_0^{2\pi}\epsilon^2\frac{\partial\psi_0}{\partial r}(r=1)\\ = \quad & -2\pi^2\int_0^{2\pi}\epsilon^2, \qquad (3.169) \end{aligned}$$

we have the energy H_ϵ due to the contour deformation of the vortex patch as follows:

$$\begin{aligned} H_\epsilon &= H-H_0\\ &= -4\pi^2\int_0^{2\pi}\epsilon^2-2\pi\int_0^{2\pi}d\theta\int_0^{2\pi}d\theta^{'}\ln(2-2\cos(\theta-\theta^{'}))+O(\lambda^2)\\ &= -8\pi^3\sum_{k\neq 0}\left(1-\frac{1}{|k|}\right)|\epsilon_k|^2+O(\lambda^3), \qquad (3.170) \end{aligned}$$

with the substitution of the Fourier series for ϵ and $\epsilon^{'}$.

Since the angular frequency of the rotating frame is 2π, the self-energy of the contour deformation in the rotating frame is

$$H_\epsilon-2\pi L_\epsilon=8\pi^3\sum_{k\neq 0}\frac{|\epsilon_k|^2}{|k|}, \tag{3.171}$$

correct to $O(\lambda^2)$. Substituting Eqs.(3.65) and (3.86), we obtain the fast-time averaged self -energy of the contour distortion as

$$< H_\epsilon-2\pi L_\epsilon >= 8\pi^3\lambda^2\sum_{k\neq 0}\frac{|b_k|^2}{|k|}+8\pi^3\lambda^2\sum_{\neq 0}\frac{|V_k^{(1)}|^2}{4\pi^2|k|}. \tag{3.172}$$

In the equation above, the first term is the self-energy of the Kelvin waves, the second term is that of the image charge part.

3.10 Appendix 5

In this appendix, we discuss the contour dynamics simulation method developed by Zabusky *et al* [58]. The method is applicable to simulations that involve vortex patches. Here we illustrate the method as applied to the evolution of one vortex patch with vorticity 4π.

The dynamics of a vortex patch is completely determined by the evolution of its contour. The velocity at a spatial point $\mathbf{r} = (x, y)$ due to the vortex patch can be expressed in term of the line integral along the contour:

$$\mathbf{v}_b = 4\pi \oint d\mathbf{l}' G(\mathbf{r} - \mathbf{r}_c') = -2 \oint d\mathbf{l}' \ln |\mathbf{r} - \mathbf{r}_c|, \tag{3.173}$$

where we have used Eqs. (3.17) and (3.9). Here $d\mathbf{l}'$ is an infinitesimal vector along the contour in the anti-clockwise direction, and $\mathbf{r}_c$ is a point on the contour. With the equation above, the evolution of the vortex patch can be reduced into the evolution of the contour.

Numerically, the contour is represented by N node points on the contour. The contour segment between two consecutive node points is approximated as a straight line. The evolution of the contour is therefore represented by the evolutions of these N node points.

With the contour approximated as connected straight lines, the velocity integral of Eq.(3.173) becomes a sum of the contributions from each line segment. We denote the position of the n-th node point as $\mathbf{r}_n = (x_n, y_n)$. (The first node point is also labeled as the $(N+1)$-th node point for convenience.) Defining

$$l_n \equiv \sqrt{(x_{n+1} - x_n)^2 + (y_{n+1} - y_n)^2} \tag{3.174}$$

as the length of the n-th line segment (*i.e.* the line segment between the n-th and $(n+1)$-th points),

$$\theta_n \equiv \tan^{-1}\left(\frac{y_{n+1} - y_n}{x_{n+1} - x_n}\right) \tag{3.175}$$

as the angle between the n-th segment and the x-axis, (x', y') as the coordinate of a point on the n-th segment, and

$$\rho \equiv \sqrt{(x-x')^2+(y-y')^2)}, \tag{3.176}$$

we find that

$$\mathbf{v}_b = \sum_{n=1}^{N} u_n(\hat{\mathbf{x}}\cos\theta_n + \hat{\mathbf{y}}\sin\theta_n), \tag{3.177}$$

where

$$u_n = -2\int_0^{l_n} dl \ln\rho, \tag{3.178}$$

with

$$dl = \sqrt{dx'^2+dy'^2}. \tag{3.179}$$

Denoting

$$\rho_n \equiv \sqrt{(x-x_n)^2+(y-y_n)^2} \tag{3.180}$$

and

$$\phi_n \equiv \tan^{-1}\left(\frac{y-y_n}{x-x_n}\right), \tag{3.181}$$

as the length of and the angle made with the the x axis for the vector from (x_n, y_n) to (x, y), we obtain

$$\rho^2 = \rho_n^2(1+\zeta^2-2\zeta\mu_n), \tag{3.182}$$

where

$$\zeta = \frac{x' - x_n}{\rho_n\cos\theta_n}, \tag{3.183}$$

and

$$\mu_n = \cos(\phi_n - \theta_n). \tag{3.184}$$

Using Eq.(3.182) and the relation

$$dl = \frac{dx'}{\cos\theta_n} = \rho_n d\zeta, \tag{3.185}$$

the integral in Eq.(3.178) can be calculated as follows:

$$\begin{aligned} u_n &= -2\int_0^{l_n/\rho_n} d\zeta\rho_n \ln\rho \\ &= -l_n\left[\ln\rho_n^2 + \left(1-\frac{\mu_n\rho_n}{l_n}\right)\ln q_n - 2 + 2(1-\mu_n^2)^{\frac{1}{2}}\frac{\rho_n}{l_n}\tan^{-1}\beta_n\right], \end{aligned} \tag{3.186}$$

where

$$q_n = 1 - \frac{2l_n\mu_n}{\rho_n} + \left(\frac{l_n}{\rho_n}\right)^2, \tag{3.187}$$

and

$$\beta_n = \frac{l_n(1-\mu_n^2)^{\frac{1}{2}}}{\rho_n - l_n\mu_n}. \tag{3.188}$$

Special care must be paid if (x, y) coincide with the n-th node point. In this case,

$$u_n = -2\int_0^1 d\zeta l_n \ln(l_n\zeta) = -2l_n(\ln l_n - 1). \tag{3.189}$$

With Eqs.(3.177), (3.186) and (3.189), the velocities due to the approximated contour can be easily calculated. In particular, the velocities of the node points $\mathbf{v}_n$ $(n = 1, ..., N)$ are determined.

To obtain the evolution of the approximated contour, the "leap-frog" marching scheme in time is used. Let Δt as the time step, then

$$\mathbf{r}_n(t + 2\Delta t) = \mathbf{r}_n(t) + 2\Delta t\mathbf{v}_n(t + \Delta t). \tag{3.190}$$

The accuracy of this scheme is of order Δt^2.

To start the leap-frog marching scheme, one needs not only the initial positions of the node points, but also those at time Δt, so that the velocities at Δt can be calculated. This is accomplished by using the Euler scheme at the beginning with a much smaller time step $\Delta t' = \Delta t/2^m$ $(m = 10$ is typically used):

$$\mathbf{r}_n(\Delta t') = \mathbf{r}_n(0) + \Delta t'\mathbf{v}_n(0). \tag{3.191}$$

Then $\mathbf{r}_n(2\Delta t')$ can be obtained by the leap-frog scheme from $\mathbf{r}_n(\Delta t')$ and $\mathbf{r}_n(0)$. Doubling the time step and using the leap-frog scheme, we obtain $\mathbf{r}_n(4\Delta t')$ from $\mathbf{r}_n(2\Delta t')$ and $\mathbf{r}_n(0)$. This procedure is carried out until the time step becomes Δt. Then with the leap-frog scheme we can obtain $\mathbf{r}_n(2\Delta t)$ from $\mathbf{r}_n(\Delta t)$ and $\mathbf{r}_n(0)$, and then obtain $\mathbf{r}_n(3\Delta t)$ from $\mathbf{r}_n(2\Delta t)$ and $\mathbf{r}_n(\Delta t)$, so on and so forth.

In our code, the following parameters are used: $N = 240$, $\Delta t = 2\pi/N/10$. To test the code, we have simulated the evolution of a vortex patch with elliptical shape. The semi-axes of the ellipse are $a = 2$ and $b = 1$. Kirchoff has shown analytically that the elliptic patch will rotate steadily with an angular frequency

$$\Omega = 4\pi \frac{ab}{(a+b)^2} = \frac{8\pi}{9}, \tag{3.192}$$

or in other worlds, the rotating period of the patch is 9/4[54]. The code gives rotation period

$$t_0 = \frac{9}{4} - 0.0003, \tag{3.193}$$

which is quite accurate.

Chapter 4

Characteristics of Two-Dimensional Turbulent Flows that Self-Organizes into Vortex Crystals

4.1 Introduction

Experimentally, the formation of the vortex crystals depends on delicate control of the initial vorticity distribution of the turbulent flow. Slight variations of the initial vorticity distribution can result in different numbers of strong vortices in the vortex crystals. From some initial conditions, no vortex crystal forms; instead, all of the strong vortices merge into a single strong vortex, which sits on the center of the background flow (see Fig.1.2 in chapter 1). In this chapter we show that the number of the strong vortices remaining in the vortex crystals, N_c, can be approximately predicted from the characteristics of the turbulent flows in their early stages of evolution.

Our analysis relies on a physical picture, suggested by the regional maximum fluid entropy (RMFE) theory (see chapter 2) and supported by a recent vortex-in-cell simulation[51], that vortex crystals form because of the interaction between the strong vortices and the low vorticity background. While advecting chaotically and merging occasionally with each other, the strong vortices ergodically mix the background. The mixing of the background, in return, "cools" the chaotic motions of the strong vortices. The chaos in the motions of the strong vortices is necessary for sustaining the mergers of the strong vortices, since to merge, two strong vortices must approach each other within a critical distance [59, 60, 61, 19, 52]. The cooling by the mixing, therefore, eventually stops the merger process, leaving a number of strong vortices to survive the mergers and fall into geometric equilibrium patterns.

Quantitatively, this physical picture suggests that if the average time between merger events, τ_m, is longer than the average time for cooling the chaotic motions of the strong vortices, τ_c, merger stops and a vortex crystal forms. We estimate τ_m from the power law decay of the number $N(t)$ of the strong vortices, which is suggested by the punctuated scaling theory[35], and estimate τ_c from the mixing properties of passive scalars in the field of the point vortices that model the strong vortices. Equating these two time scales, N_c is predicted in terms of the number and the average circulation of the strong vortices, the area occupied by the flow, and the exponents of the power laws for the quantities associated with the strong vortices, all measured in the early stage of the turbulent relaxation. The prediction agrees reasonably well with the data from experiments as well as vortex-in-cell simulations.

4.2 The Theory

4.2.1 Estimation of τ_m

Due to pairwise mergers, the number $N(t)$ of the strong vortices decreases in time t in the early stage of the turbulent relaxation. The merger is a quite complicated process that is subject to detailed theoretical and experimental studies.

However, it is well established that in order to merge, the distance between the two strong vortices must be less than a critical distance, which is about 3.3 times their average radii. Numerical simulations[34, 33] and experiments[62, 38] have found that $N(t)$ evolves according to a power law:

$$N(t) = N(t_0)\left(\frac{t}{t_0}\right)^{-\xi}, \tag{4.1}$$

where $\xi > 0$ is a constant. Other quantities associated with the strong vortices also evolve in time according to power laws. For example, the average circulation of the strong vortices, $\Gamma_a(t)$, increases in time as

$$\Gamma_a(t) = \Gamma_a(t_0)\left(\frac{t}{t_0}\right)^{\eta\xi}, \tag{4.2}$$

where $\eta > 0$ is a constant. Although there are some heuristic arguments[63], the power law behavior of $N(t)$ remains as an empirical fact. The punctuated scaling theory, which is based on a merger model that conserves the total energy and the maximum vorticity of the strong vortices, suggests that $\xi = 0.70 \sim 0.75$, and $\eta = 0.5$[35]. Although the theory is supported by some numerical calculations[36] and experiments done with a thin stratified layer of electrolyte [37], experiments that observed vortex crystals [38] have shown that these exponents can take different values in different situations. In this work, we take Eqs. (4.1) and (4.2) as empirical laws, and measure the the exponents from experiments and simulations.

From Eq.(4.1), we have

$$\frac{\Delta N}{\Delta t} \approx \frac{dN}{dt} = -\frac{\xi N(t_0)}{t_0}\left(\frac{t}{t_0}\right)^{-1-\xi}, \tag{4.3}$$

where ΔN is the change of N in time interval Δt. Therefore, taking $\Delta N = -1$, the average time τ_m between mergers can be estimated as:

$$\tau_m \approx \frac{(-1)}{\frac{dN}{dt}} = \frac{t_0}{\xi N(t_0)}\left(\frac{t}{t_0}\right)^{1+\xi}. \tag{4.4}$$

As t increases, the average time between the mergers increase because there are fewer strong vortices available for mergers.

4.2.2 Estimation of τ_c

As we have shown in chapter 2, vortex crystals are well described as the RMFE states, with the simple assumption that the background flow has a single microscopic vorticity level ω_f. The vorticity field of the background is chaotically mixed by the strong vortices and the random field of the background. A coarse-grained vorticity distribution $\bar{\omega}(\mathbf{r},t)$ describes the macroscopic state of the background flow. There are many possible ways of arranging the microscopic vorticity field to achieve a given $\bar{\omega}(\mathbf{r},t)$, therefore, a fluid entropy can be associated with it:

$$S = -\int_{D_b} d\mathbf{r}^2 \left[\frac{\bar{\omega}}{\omega_f} \ln \frac{\bar{\omega}}{\omega_f} + \left(1 - \frac{\bar{\omega}}{\omega_f}\right) \ln \left(1 - \frac{\bar{\omega}}{\omega_f}\right) \right], \tag{4.5}$$

which follows from Eq.(2.13) for the case of the background flow having the a single microscopic vorticity level. [1] Here D_b denotes the domain occupied by the background. For given positions of the strong vortices $\{\mathbf{R}_i\}$, $i = 1,...,N$, the background can be in any macroscopic state that satisfies the constraints of the turbulent flow: conservations of the total circulation Γ, total angular momentum L (since the flow is subject to a free-slip boundary in a circular domain), and total energy H. Among these states, there is one state that has the maximum fluid entropy of the background. The coarse-grained vorticity distribution of this state is given by the Fermi distribution, Eq.(2.36). We define the fluid entropy of this state, $S_m(\{\mathbf{R}_i\})$, as the "entropy roof" of the background.

The function $S_m(\{\mathbf{R}_i\})$ indicates the maximum degree of mixing that the background can achieve for a given configuration of the strong vortices.

The configurations of the strong vortices in RMFE states correspond to the local maxima of the entropy roof. As we have shown in chapter 2, these configurations are quite symmetric, and the distances between the strong vortices are well beyond the critical distances for mergers. If the positions of the strong vortices deviates from the configuration $\{\mathbf{R}_i^{(0)}\}$ for a RMFE state, the entropy roof

---

[1] We have also renormalized the fluid entropy with the constant k_B/Δ^2, which is present in Eq.(2.13).

decreases in height. Taylor expansion of $S_m(\{\mathbf{R}_i\})$ near $\{\mathbf{R}_i^{(0)}\}$ gives

$$S_m(\{\mathbf{R}_i\}) = S_m(\{\mathbf{R}_i^{(0)}\}) - \frac{1}{2}\sum_{i,j}(\mathbf{R}_i - \mathbf{R}_i^{(0)}) \cdot \mathcal{C} \cdot (\mathbf{R}_i - \mathbf{R}_i^{(0)}), \tag{4.6}$$

where

$$\mathcal{C} \equiv -\frac{\partial^2 S_m(\{\mathbf{R}_i^{(0)}\})}{\partial \mathbf{R}_i \partial \mathbf{R}_j} \tag{4.7}$$

is a positive definite tensor. The entropy roof for the near merger configurations is lower than the entropy roof for the configurations near the RMFE states, since to merge, a pair of strong vortices must be within the critical distance and the configuration of the strong vortices must deviate by large amounts from the RMFE states. For a give size of the deviations $\{\mathbf{R}_i - \mathbf{R}_i^{(0)}\}$, the amount the entropy roof lowered is proportional to the magnitude of the tensor $\mathcal{C}$, or the "curvature" of the entropy roof.

We examine with an example the shape of the entropy roof as the positions of the strong vortices vary. In the example, there are five identical Gaussian strong vortices. Each strong vortex has circulation 0.02 and radius 0.04. The flow has total circulation $\Gamma = 1$, angular momentum $L = -0.08$, and energy $H = 0.093$. The background has a single microscopic vorticity level $\omega_f = 2.0$. We first calculate the RMFE state following the procedure described in chapter 2. In the RMFE state, the strong vortices are arranged in a symmetry pentagon pattern, as shown in Fig.4.1.a. We then produce configurations of the strong vortices that deviate from this equilibrium pattern by shifting each strong vortex from its equilibrium position by a distance ΔR in a random direction. Depending on the random directions, different configurations are generated with the same ΔR. The maximum fluid entropy state for the given configuration is then calculated. [2] The configurations produced with large ΔR are far from the equilibrium pattern, whereas those produces with small ΔR are near to the equilibrium pattern. Accordingly, the entropy roof corresponding to the configurations with large ΔR is in general

---

[2] The method of calculating the entropy roof for given positions of the strong vortices is the same as the calculation of the RMFE state, except that the searching of the equilibrium positions of the strong vortices is omitted.

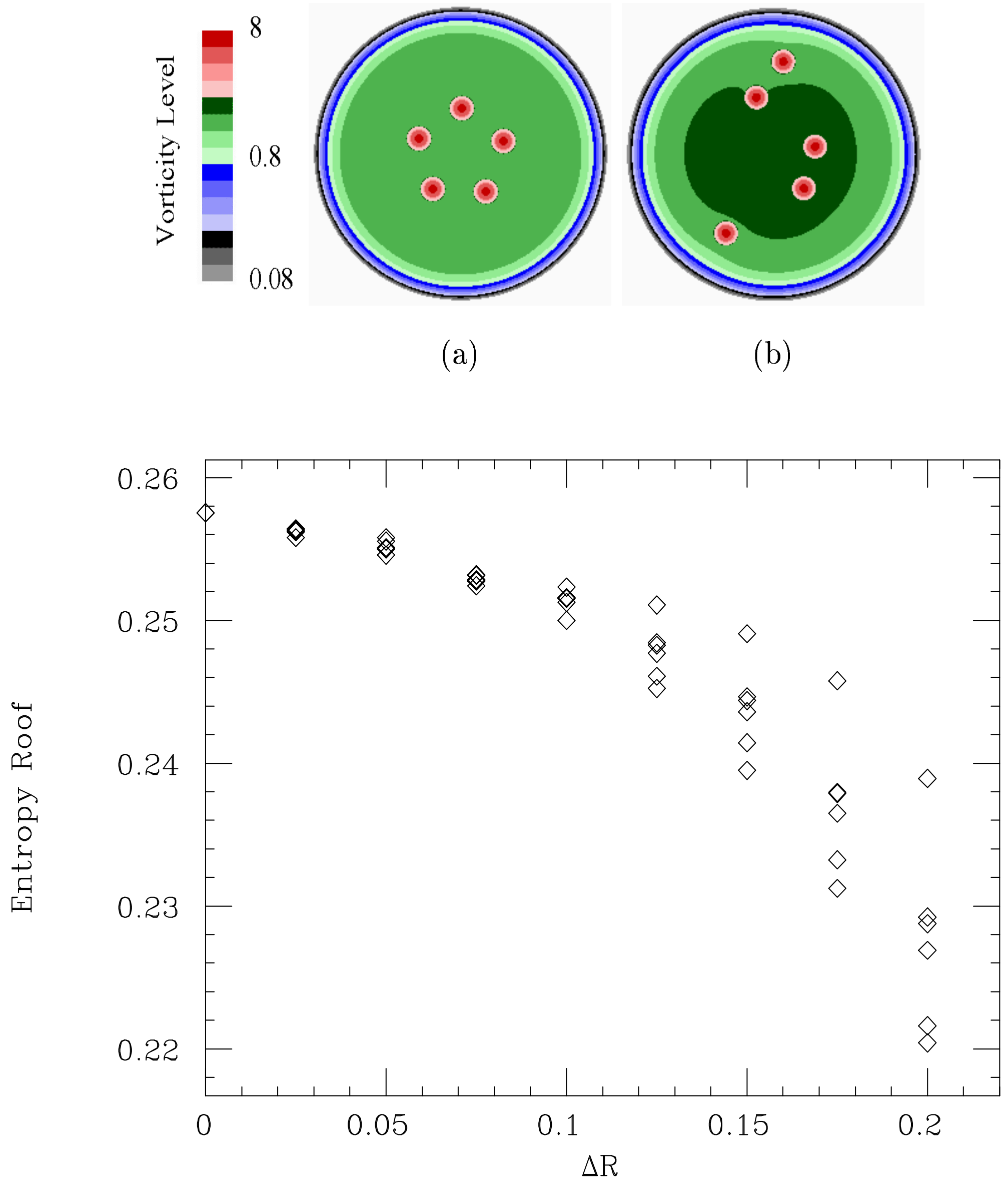

(a) (b)

(c)

Figure 4.1: Entropy roof corresponding to the configurations of the strong vortices generated with deviation ΔR. The strong vortices are identical Gaussian vortices with radius 0.04 and circulation 0.02. The flow has $\Gamma = 1.0$, $L = -0.08$, $H = 0.093$, and $\omega_f = 2.0$. The flow shown in (a) is the RMFE state. In the flow shown in (b), the positions of the strong vortices are generated with with $\Delta R = 0.15$, and the fluid entropy of the background of the flow is 0.2414.

lower than that corresponding to the configurations with small ΔR, as shown in Fig.4.1.c, in which we plot the dependence of the entropy roof on ΔR. In Fig.4.1.b we show a flow with $\Delta R = 0.15$. The background of the flow is the maximum fluid entropy distribution for the given positions of the strong vortices. As can be seen in the figure, the strong vortices are randomly positioned and far from the equilibrium positions. Its entropy roof has a value of 0.2414, which is lower than that of the RMFE state.

In the free relaxation of the turbulence, the fluid entropy of the background S always increases. If S is far away from the entropy roof $S_m(\{\mathbf{R}_i\})$, the increase of S imposes no restriction on the motions of the strong vortices, and they can go into configurations that lead to their mergers. However, if S is close to S_m, the increase of S restricts the configurations that the strong vortices can explore – the strong vortices can not take configurations whose entropy roof is lower than the entropy that the background have already achieved. In this case, the possible configurations that the strong vortices can explore are restricted to a set nearby a local maximum of the entropy roof, and the increase of S reduces the size of the set, until the set reduces into one point – the RMFE configuration. This makes configurations that lead to mergers unlikely, since such configurations deviate from equilibrium by a large distance and hence have a relatively low entropy roof. Therefore, if the background is well mixed so that its fluid entropy is near the entropy roof, the mergers tend to stop. Hence, we can estimate τ_c as the time scale for the background to be well mixed from any initial state.

The mixing in turbulent fluids is in general very complicated and hard to analyze. However, chaotic advection, or the chaotic motion of passive scalars in a prescribed flow that retains the essence of the turbulent flow, can often provide insights into the nature of the turbulent mixing[64, 65]. In our case, since the strong vortices, which are intense in vorticity and small in radius, are the primary mixers of the background, we can study the chaotic advection in the fields of point vortices to understand the mixing of the background.

The velocity field of N point vortices with circulations Γ_i, $i = 1, ..., N$ and subject to a circular, free-slip boundary of radius 1 is given by

$$\mathbf{v}(\mathbf{r}, t) = \nabla \psi_v(\mathbf{r}, t) \times \hat{\mathbf{z}}, \tag{4.8}$$

where

$$\psi_v(\mathbf{r}, t) = -\sum_i \frac{\Gamma_i}{2\pi} \ln |\mathbf{r} - \mathbf{R}_i(t)| + \sum_i \frac{\Gamma_i}{2\pi} \left(\ln \left| \mathbf{r} - \mathbf{R}_i^{'}(t) \right| + \ln R_i(t) \right), \tag{4.9}$$

where $\mathbf{R}_i(t)$ and $\mathbf{R}_i^{'}(t) = \mathbf{R}_i / R_i^2$ are the positions of the i-th strong vortex and its image charge, respectively. The point vortices move according to

$$\frac{d\mathbf{R}_i}{dt} = \mathbf{v}(\mathbf{R}_i, t) = \nabla \psi_v^{'}(\mathbf{R}_i, t) \times \hat{\mathbf{z}}, \tag{4.10}$$

where $\psi_v^{'}(\mathbf{R}_i, t)$ is $\psi_v(\mathbf{R}_i, t)$ excluding the contribution from the i-th point vortex in the first term of the right hand side of Eq.(4.9). The equations of motion for a passive scalar at $\mathbf{r}(t) = (x(t), y(t))$ is given by

$$\frac{d\mathbf{r}}{dt} = \mathbf{v}(\mathbf{r}, t), \tag{4.11}$$

or equivalently,

$$\frac{dx}{dt} = \frac{\partial \psi_v}{\partial y}, \quad \frac{dy}{dt} = -\frac{\partial \psi_v}{\partial x}. \tag{4.12}$$

Observe that ψ_v can be regarded as the Hamiltonian for a particle in one dimensional motion, with $x(t)$ and $y(t)$ being the generalized coordinate and momentum. Then the trajectory of the passive scalar is the phase space trajectory of the particle. The Hamiltonian structure for the motion of the passive scalar enables us to apply many results from the study of the dynamical systems to the chaotic advection problem[64].

If the point vortices are in equilibrium positions, ψ_v is time independent in the rotating frame of the equilibrium. Then, Eq.(4.12) is integrable, and the trajectory of the passive scalar is not chaotic. The trajectory can go around one of the point vortices, or a number of them, depending on the initial position. The initial positions for different types of trajectories are separated by separatrix.

If the strong vortices are slightly out of equilibrium, ψ_v is time dependent. As the generic behavior of systems with time dependent Hamiltonian[66], the trajectory of the passive scalar is chaotic if its position is in a narrow region along the separatrix. As the deviation from the equilibrium increased, this stochastic region grows. If the strong vortices are completely out of equilibrium, their motions are chaotic; then the trajectory of the passive scalar is chaotic starting from all of the initial positions excepts those very close to the strong vortices[67].

The trajectory of a passive scalar is chaotic if its Lyapunov exponent λ is positive, non-chaotic otherwise. The Lyapunov exponent of a trajectory is defined as follows[68]. Consider two infinitesimally close trajectories, $\mathbf{r}(t)$ and $\mathbf{r}(t) + \epsilon\mathbf{p}(t)$. Linearizing Eq.(4.11) in the limit $\epsilon \to 0$, we obtain

$$\frac{d\mathbf{p}}{dt} = \frac{\partial \mathbf{v}}{\partial \mathbf{r}} \cdot \mathbf{p}, \tag{4.13}$$

where

$$\frac{\partial \mathbf{v}}{\partial \mathbf{r}} = \begin{pmatrix} \frac{\partial^2 \psi_v}{\partial x \partial y} & \frac{\partial^2 \psi_v}{\partial y^2} \\ -\frac{\partial^2 \psi_v}{\partial x^2} & -\frac{\partial^2 \psi_v}{\partial x \partial y} \end{pmatrix} \tag{4.14}$$

is the Jacobian matrix. Then,

$$\lambda = \lim_{t \to \infty} \Lambda(t) = \lim_{t \to \infty} \frac{1}{t} \ln \frac{|\mathbf{p}(t)|}{|\mathbf{p}(0)|}. \tag{4.15}$$

Numerically, to avoid unbounded growth of $\mathbf{p}(t)$, Eq.(4.13) is integrated over a period T with $|\mathbf{p}(0)| = 1$. $\mathbf{p}(T)$ is then normalized and Eq.(4.13) is integrated for another period T to get $\mathbf{p}(2T)$. This process is iterated for many times. Then the Lyapunov exponent is given by[69]

$$\lambda = \lim_{n \to \infty} \frac{1}{nT} \sum_{k=1}^{n} \ln |\mathbf{p}(kT)|. \tag{4.16}$$

A collection of passive scalars occupying a small region in the stochastic region will spread out the whole chaotic region exponentially in time. The rate of this complete randomization is given by the average of the Lyapunov exponents of the passive scalars in the chaotic region, since the Lyapunov exponents are the rates of the exponential divergence of trajectories of passive scalars initially placed closely.

It is difficult to obtain an analytic estimation for the average Lyapunov exponent $\bar{\lambda}$ in the stochastic region. However, when the point vortices have approximately equal circulations and their motions are chaotic in a region of area A, the main physical quantities that determine $\bar{\lambda}$ is the average circulation Γ_a of the point vortices and the average distance D between the nearby point vortices. Dimensional analysis then gives

$$\bar{\lambda} \approx \alpha \frac{\Gamma_a}{D^2} \tag{4.17}$$

where α is a constant. Since the point vortices are uniformly distributed on time average in the region of area A, we have

$$D \approx \sqrt{\frac{A}{N}}. \tag{4.18}$$

Therefore, Eq.(4.17) can also be written as

$$\bar{\lambda} \approx \alpha \frac{N\Gamma_a}{A} = \alpha \frac{\Gamma_T}{A}, \tag{4.19}$$

where $\Gamma_T = \sum_i \Gamma_i$ is the total circulation of the point vortices.

To check the validity of Eq.(4.19), we have calculated $\bar{\lambda}$ in the field of N point vortices with circulations 4π. The point vortices are randomly placed initially in a circular region. We vary both N and the radius of the circular region. The result, shown in Fig.4.2, confirms Eq.(4.19), with $\alpha \approx 0.031$.

With the estimation of the Lyapunov exponent for the passive scalars in the fields of the point vortices, the complete randomization time of the background in the free relaxation of the turbulence can be estimated as

$$\tau_c \approx \frac{1}{\bar{\lambda}} \approx \frac{A}{\alpha \Gamma_T}, \tag{4.20}$$

where A is now identified as the area occupied by of the background flow, and Γ_T as the total circulation of the strong vortices.

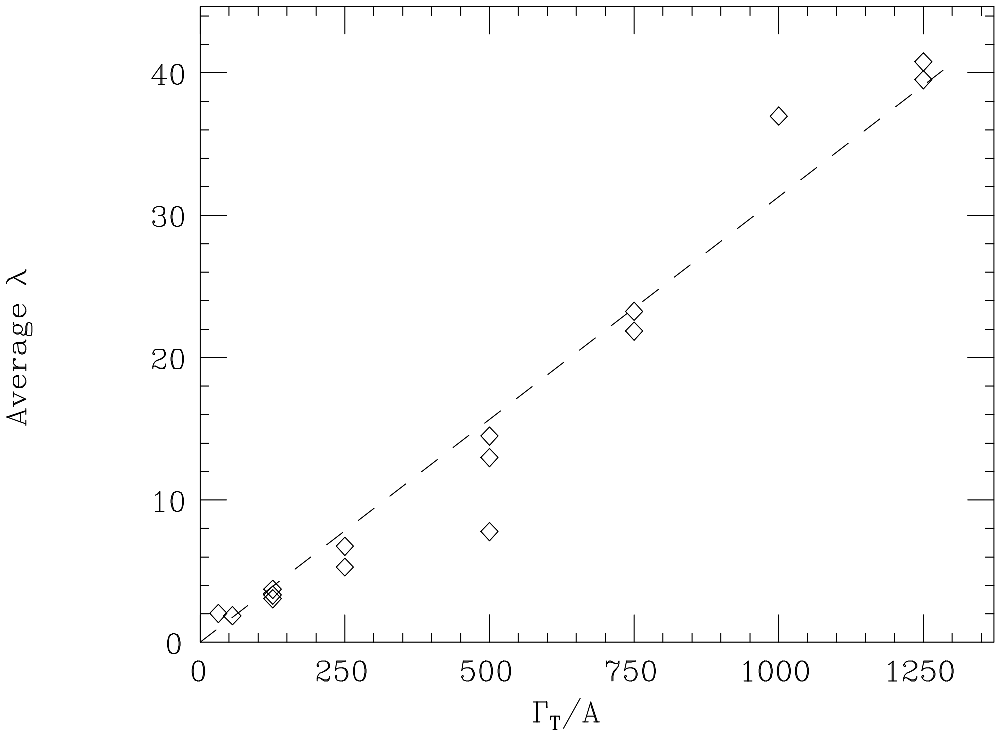

Figure 4.2: Relation between the average Lyapunov exponent $\bar{\lambda}$ of the passive scalars and the ratio Γ_T/A, where Γ_T is the total circulation of the point vortices, and A is the area of the region in which the point vortices are randomly distributed initially. The dashed line, with a slope 0.031, is the best fit to the data.

To show that τ_c as given in Eq.(4.20) is indeed the time scale on which the mergers of the strong vortices tend to stop, we have performed a vortex-in-cell simulation. In the simulation, five identical point vortices with total circulation 0.5 are randomly distributed within a ring vorticity with inner radius 0.4 and width 0.05. The total circulation of the flow is 1. In Fig.4.3, we plot the flow evolution as well as the evolution of the minimum distance between the point vortices. For the flow, $\tau_c = 32.43$ as evaluated by Eq.(4.20), with $A = 0.4^2\pi$. This value is indicated with an arrow in the figure. The figure shows after $t = \tau_c$, the lower limit for the minimum distance that the point vortices can approach each other steadily increase, and the close encounter between the point vortices are prohibited.

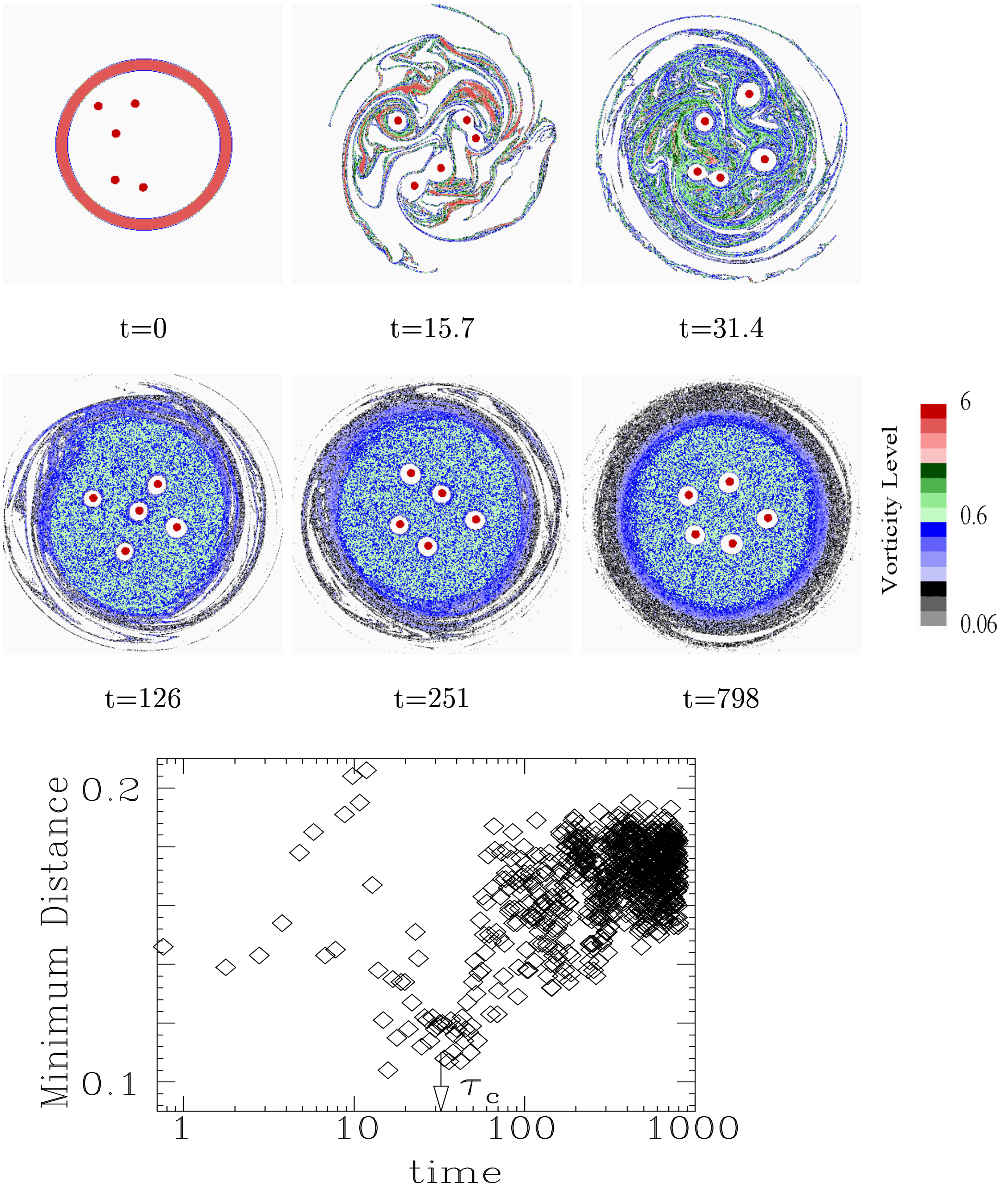
t=0 t=15.7 t=31.4

t=126 t=251 t=798

Figure 4.3: A vortex-in-cell simulation in which five identical point vortices with total circulation 0.5 randomly distributed in a ring vorticity with inner radius 0.4 and width 0.05. The total circulation of the flow is 1. The flow evolution is display on the top rows. In the figure, the minimum distance between the point vortices is plotted against time. The arrow in the figure indicates the complete randomization time τ_c as evaluated by Eq.(4.20), with $A = 0.4^2\pi$.

The randomization time τ_c depends on the total circulation of the strong vortices, which decreases as the strong vortices merge. From Eqs.(4.1) and (4.2), we obtain

$$\Gamma_T(t) = N(t_0)\Gamma_a(t_0)\left(\frac{t}{t_0}\right)^{\eta\xi-\xi}. \tag{4.21}$$

Therefore, from Eq.(4.20) we get

$$\tau_c \approx \frac{A}{\alpha N(t_0)\Gamma_a(t_0)}\left(\frac{t}{t_0}\right)^{\xi-\eta\xi}. \tag{4.22}$$

4.2.3 Prediction of N_c

Equation (4.22) shows that τ_c grows much slower than τ_m since $\eta > 0$ (cf. Eq.(4.4)).[3] Therefore, starting from $\tau_m < \tau_c$, τ_m will eventually catch up with τ_c at $t = t_c$, and mergers of the strong vortices stop. Here t_c is found by setting $\tau_c \approx \tau_m$, and from Eqs. (4.4) and (4.22) we arrive at

$$t_c \approx t_0\left(\frac{\xi A}{\alpha t_0 \Gamma_a(t_0)}\right)^{\frac{1}{1+\eta\xi}}, \tag{4.23}$$

and accordingly, the number of the strong vortices in the vortex crystals is obtained by setting $t = t_c$ in Eq.(4.1):

$$N_c \approx N(t_0)\left(\frac{\alpha t_0 \Gamma_a(t_0)}{\xi A}\right)^{\frac{\xi}{1+\eta\xi}}. \tag{4.24}$$

This equation shows that in order to form vortex crystals with many surviving strong vortices, initially the flow should have a large number of strong vortices with large average circulation.

4.3 Comparison with Experiments and Simulations

The prediction of Eq.(4.24) is checked with both experiments with pure electron columns[38] and vortex-in-cell simulations. The physical quantities are normalized according to the following units: length – r_w, the radius of the free-slip

---

[3] if $\eta > 1$, which is not normally observed, τ_c can actually decrease with time.

circular boundary; vorticity – Γ/r_w^2, where Γ is the total circulation of the flow; time – r_w^2/Γ. The exponents ξ, η, as well as quantities N, Γ_v and A are measured in the power law regime of the turbulent relaxation. Then each flow in this regime predicts N_c according to Eq.(4.24). Predictions at different times vary a little since the power laws are not exact.

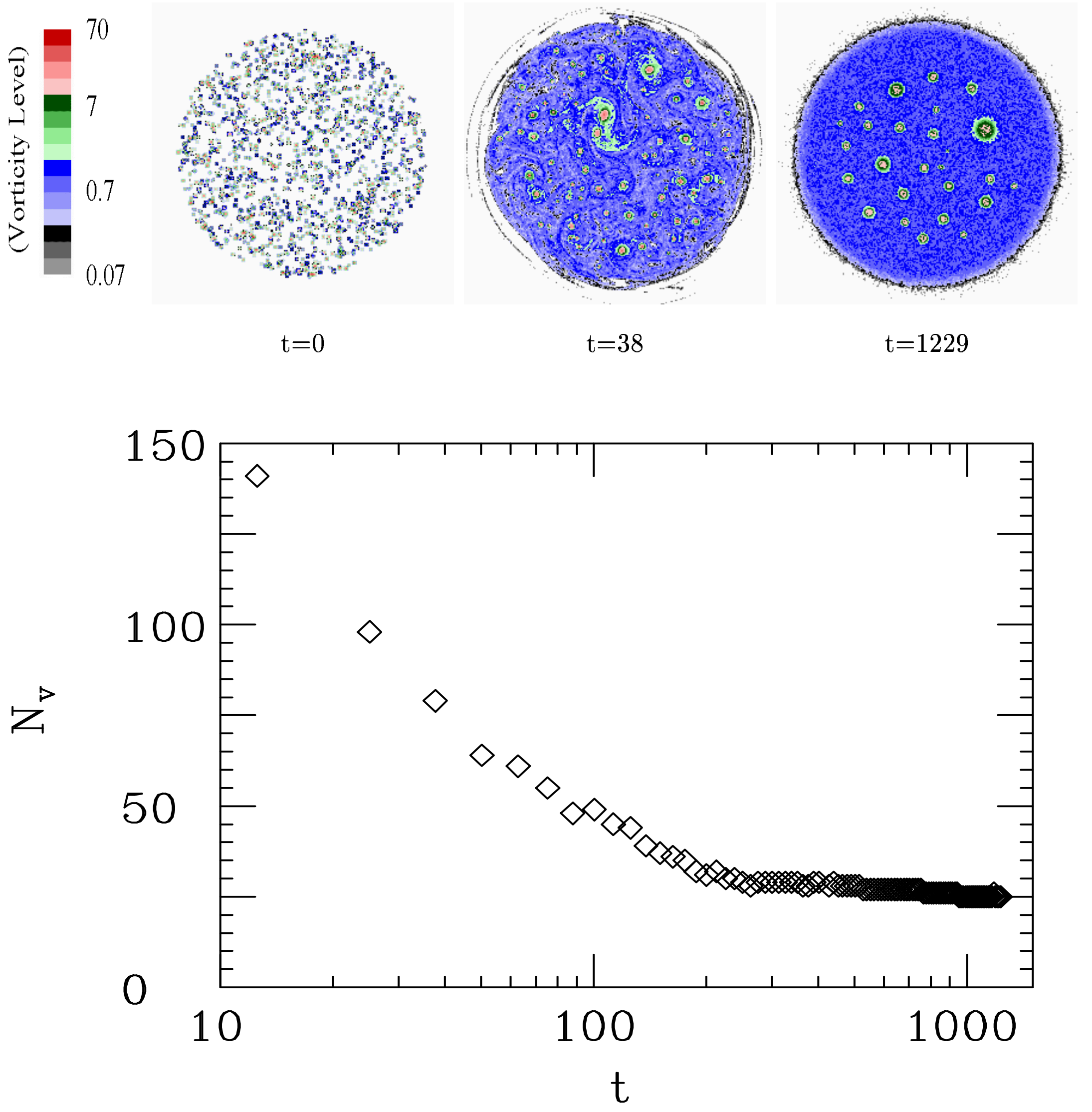

Figure 4.4: Flow evolution in a typical run of the simulation. Up: Vorticity distributions at three different times. Down: The evolution of the number of the strong vortices.

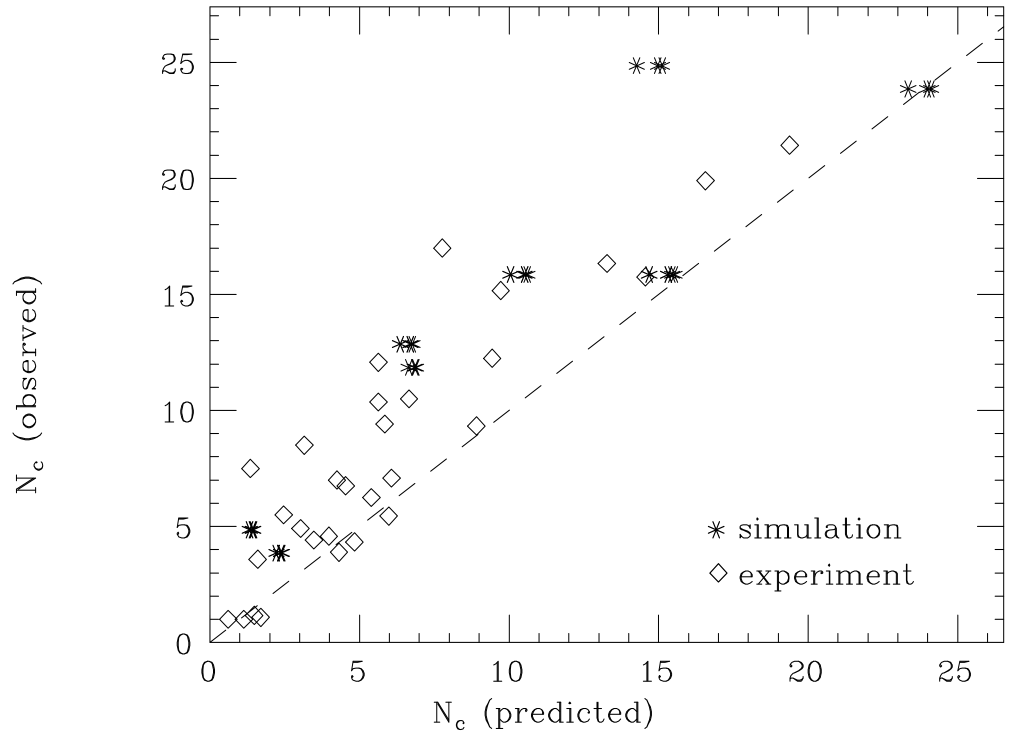

Figure 4.5: Comparison of the predicted number N_c of the strong vortices in the vortex crystals with the N_c of the experiments and the simulations. Each data point represents a particular evolution of the turbulent flow. The value for the predicted N_c for each evolution is obtained by averaging the predictions at different times in the power law regime.

In the simulation, initial conditions are generated by randomly distributing in a circular region a large number of Gaussian vortices with a given radius and random maximum vorticity. The number of the strong vortices initially formed is controlled by the radius of the random Gaussian vortices and their distributions within the circular region. Generally, a large number of strong vortices form if the Gaussian vortices have small radius and sparsely distributed. In Fig.4.4, we show a typical run of the simulation. The vorticity distributions at three times and the evolution of the number of the strong vortices are displayed.

The prediction of Eq.(4.24) agrees reasonably well with the experiments and the simulations. This is shown in Fig.4.5, in which we plot the predicted N_c, averaged over the power region of $N(t)$, against the observed N_c for the experiments the simulations. The scattering of the data, however, is quite large. This is expected, given that our estimation of τ_c is not as yet a detailed theory, and the process of vortex crystal formation is rather chaotic. Nevertheless, the prediction at least clearly distinguishes the characteristics of the flows that form vortex crystals with many strong vortices from that of the flows that form no vortex crystals.

4.4 Discussions

Until now, vortex crystals have been only observed in the turbulent flows with single sign of vorticity, subject to a circular, free-slip boundary condition. It is interesting to know if vortex crystals can form in more general cases with both sign of vorticity and/or different boundary conditions. Our theory suggests that two conditions are crucial for vortex crystal formation. The first condition is that there should be stable RMFE states. Calculations similar to those we have done in chapter 2 should be carried out to reveal that ordered, stable structures for the strong vortices can emerge by maximization of the fluid entropy of the low vorticity background. The second condition is that the mixing time scale τ_c of the background must be sufficiently fast. This can be investigated with the chaotic advection of the point vortices, as we have done in this chapter. It is conceivable that the mixing time scale can be very different depending on the characteristics of the turbulent flow. For example, if there are approximately equal number of similar-sized positive and negative strong vortices, the mixing of the background may not be as efficient as the case we have studied in this chapter, since the opposite signed strong vortices tend to form dipole pairs and hence at least partially cancel each other's mixing ability. If there are stable RMFE states and the mixing time scale can eventually catch up with the merging time scale of the strong vortices, vortex crystals can form. Also, as we have shown in this chapter, another requirement that many strong vortices in the initial stage of the turbulent flow.

Our theory relies on the power laws for the quantities associated with the strong vortices in the early stage of the turbulent relaxation, and the cooling time scale for the strong vortices inferred from the chaotic advection in the field of the point vortices; therefore, it is not yet a rigorous theory. Further study is needed to put the theory on more solid theoretical ground.

Bibliography

[1] D. G. Dritschel and B. Legras, "Modeling oceanic and atmospheric vortices", Phys. Today, Mar **46**, 44 (1993)

[2] U. Frisch, *"Turbulence"*, Cambridge University Press, 240 (1995)

[3] P. S. Marcus, "Numerical simulation of Jupiter's Great Red Spot", Nature, **331**, 693 (1988)

[4] J. Sommeria, S. P. Meyers and H. L. Swinney, "Laboratory simulation of Jupiter's Great Red Spot", Nature, **331**, 689 (1988)

[5] A. P. Ingersoll, "Atmospheric Dynamics of the Outer Planets", Science, **248**, 308 (1990)

[6] M. R. Brown, "Experimental evidence of rapid relaxation to large-scale structures in turbulent fluids: selective decay and maximal entropy", J. Plasma Phys., **57**, 203 (1997)

[7] B. K. Martin, X. L. Wu, W. I. Goldburg, and M. A. Rutgers, "Spectra of decaying turbulence in a soap film", Phys. Rev. Lett., **80**, 3964 (1998)

[8] L. Onsager, "Statistical hydrodynamics", Nuovo Cimento, suppl. **6**, 279 (1949)

[9] G. Joyce and D. Montgomery, "Negative temperature states for the two-dimensional guiding center plasma", J. Plasma Phys., **10**, 107 (1973)

[10] D. Montgomery, W. H. Matthaeus, W. T. Stribling, D. Martinez, and S. Oughton, "Relaxation in two dimensions and the 'sinh-Poisson' equation", Physics of Fluids A **4**, 3(1992)

[11] D. Montgomery, Xiaowen Shan, and W. H. Matthaeus, "Naiver-Stokes relaxation to sinh-Poisson states at finite Reynolds numbers", Phys. Fluids **A5**, 2207 (1993)

[12] R. A. Smith, "Maximization of vortex entropy as an organizing principle in intermittent, two-dimensional turbulence", Phys. Rev. **A43**, 1126 (1991)

[13] J. Miller, "Statistical Mechanics of Euler Equations in Two Dimensions", Phys. Rev. Lett., **65**, 2137 (1990)

[14] R. Robert and J. Sommeria,"Statistical equilibrium states for two-dimensional flows", J. Fluid Mech, **229**, 291 (1991)

[15] D. Lynden-Bell, "Statistical mechanics of violent relaxation in stellar systems", Mon. Not. R. astr. Soc., **136**, 101 (1967)

[16] G. A. Kuz'min, "Statistical mechanics of the organization into two-dimensional coherent structures", in *"Structural Turbulence"*, 203-114, ed. M. A. Goldshtik, Acad. Nauk USSR, Institute of Thermophysics, Novosibirsk.

[17] J. Miller, P. B. Weichman and M. C. Cross, "Statistical mechanics, Euler's equation, and Jupiter's Red Spot" Phys. Rev. A, **45**, 2328 (1992)

[18] J. Michel and R. Robert, "Statistical mechanical theory of the Great Red Spot of Jupiter", J. Statist. Phys., **77**, 645 (1994)

[19] P. Chen and M. C. Cross, "Statistical two-vortex equilibrium and vortex merger" Phys. Rev. E, **53** R3032 (1996)

[20] P. Chen and M. C. Cross, "Phase diagram for coherent vortex formation in the two-dimensional inviscid fluid in circular geometries" Phys. Rev. E, **50**, 2022 (1994)

[21] P. Chen and M. C. Cross, "Complete phase diagram for coherent vortex formation in a two-dimensional inviscid fluid in an annulus", Phys. Rev. E, **56**, 2284 (1997)

[22] P. H. Chavanis and J. Sommeria, "Classification of self-organized vortices in two-dimensional turbulence: the case of a bounded domain", J. Fluid Mech., **314**, 267 (1996)

[23] A. Thess, J. Sommeria and B. Juttner, "Inertial organization of a two-dimensional turbulent vortex street", Phys. Fluid **6** (7), 2417 (1994)

[24] B. Juttner, A. Thess and J. Sommeria, "On the symmetry of self-organized structure in two-dimensional turbulence", Phys. Fluids **7** (9), 2108 (1995)

[25] G. K. Batchelor, "Computation of the energy spectrum in homogeneous two-dimensional turbulence", Phys. Fluid. Supplement II, II-233 (1969)

[26] R. H. Kraichnan, "Inertial ranges in two-dimensional turbulence", Phys. Fluid., **10**, 1417 (1967)

[27] F. P. Bretherton and D. B. Haidvogel, "Two-dimensional turbulence above topography", J. Fluid Mech., **78**, 129 (1976)

[28] W. H. Matthaeus and D. Montgomery, "Selective decay hypothesis att high mechanical and magnetic reynolds numbers", Ann. N. Y. Acad. Sci., **357**, 203 (1980)

[29] C. E. Leith, "Minimum enstrophy vortices", Phys. Fluids, **27**, 1388 (1984)

[30] X.-P. Huang and C. F. Driscoll, "Relaxation of 2D turbulence to a meta-equilibrium near the minimum enstrophy state" Phys. Rev. Lett., **72**, 2187 (1994)

[31] M. E. Brachet, M. Meneguzzi, H. Politano, and P. L. Sulem, "The dynamics of freely decaying two-dimensional turbulence", J. Fluid Mech., **194**, 333 (1988)

[32] B. Fornberg, "A numerical study of 2-D turbulence", J. Comput. Phys., **25**, 1 (1977)

[33] R. Benzi, S. Patarnello and P. Santangelo, "On the statistical properties of two-dimensional decaying turbulence", Europhys. Lett., **3**, 811 (1987)

[34] J. C. McWilliams, "The emergence of isolated coherent vortices in turbulent flow", J. Fluid Mech., **146**, 21 (1984)

[35] G. F. Carnevale, J. C. McWilliams, Y. Pomeau, J. B. Weiss and W. R. Young "Evolution of vortex statistics in two-dimensional turbulence", Phys. Rev. Lett., **66**, 2735 (1991)

[36] J. B. Weiss and J. C. McWilliams, "Temporal scaling behavior of decaying two-dimensional turbulence", Phys. Fluids **A5**, 608 (1993)

[37] A. E. Hansen, D. Marteau, and P. Tabeling, "Two-dimensional turbulence and dispersion in a freely decaying system", Phys. Rev. E, **58**, 7261 (1998)

[38] K. S. Fine, A. C. Cass, W. G. Flynn, and C. F. Driscoll "Relaxation of 2D turbulence to vortex crystals" Phys. Rev. Lett., **75**, 3277 (1995)

[39] C. F. Driscoll and K. S. Fine, "Experiments on vortex dynamics in pure electron plasma", Phys. Fluids **B2**, 1359 (1990)

[40] J .C. McWilliams, "The vortices of two-dimensional turbulence", J. Fluid Mech., **219**, 361 (1990)

[41] D. W. Moore and P. G. Saffman, "Structure of a line vortex in an imposed strain", "*Aircraft wake turbulence*" (eds Olsen, Goldburg, and Rogers), 339, Plenum (1971)

[42] S. Kida, "Motion of an elliptical vortex in a uniform shear flow", J. Phys. Soc. Japan, **50**, 3517 (1981)

[43] D. L. Eggleston, "Experimental study of two-dimensional electron vortex dynamics in an applied irrotational shear flow", Phys. Plasmas, **1**, 3850 (1994)

[44] D. G. Dritschel, P. H. Haynes, M. N. Juckes, and T. G. Shepherd, "The stability of a two-dimensional vorticity filament under uniform strain", J. Fluid Mech., **230**, 647 (1991)

[45] N. K.-R. Kevlahan and M. Farge, "Vorticity filaments in two-dimensional turbulence: creation, stability and effect", J. Fluid Mech., **346**, 49 (1997)

[46] T. H. Havelock, "The stability of motion of rectilinear vortices in ring formation", Philos. Mag., **11**, 617 (1931)

[47] L. J. Campbell and R. M. Ziff, "Vortex patterns and energies in a rotating superfluid", Phys. Rev. B, **20**, 1886 (1979)

[48] W. H. Press, S. A. Teukolsky, W. T. Vetterling, and B. P. Flannery, *"Numerical Recipes in Fortran"*, Cambridge University Press, 847 (1992)

[49] W. H. Press, S. A. Teukolsky, W. T. Vetterling, and B. P. Flannery, *"Numerical Recipes in Fortran"*, Cambridge University Press, 382 (1992)

[50] W. H. Press, S. A. Teukolsky, W. T. Vetterling, and B. P. Flannery, *"Numerical Recipes in Fortran"*, Cambridge University Press, 456 (1992)

[51] D. A. Schecter, K. S. Fine, D. H. E. Dubin, and C. F. Driscoll, "Vortex crystals from 2D Euler flow: experiment and simulation", Phys. Fluids **11**, 905 (1999)

[52] I. M. Lanksy, T. M. O'Neil, and D. A. Schecter, "A theory of vortex merger", Phys. Rev. Lett., **79**, 1479 (1997)

[53] H. Aref, "Integrable, chaotic, and turbulent vortex motion in two-dimensional flows", Annu. Rev. Fluid Mech., **15**, 345 (1983)

[54] P. G. Saffman, *"Vortex Dynamics"*, Cambridge University Press, Chapter 9 (1992)

[55] D. I. Pullin, "Contour Dynamics Methods", Annu. Rev. Fluid Mech., **24**, 89 (1992)

[56] G. S. Deem, N. J. Zabusky, "Vortex waves: Stationary "V states", interactions, recurrence and breaking", Phys. Rev. Lett., **40**, 859 (1978)

[57] D. G. Dritschel, "The repeated filamentation of two-dimensional vorticity interfaces", J. Fluid Mech., **194**, 511 (1988)

[58] N. J. Zabusky, M. H. Hughes, and K. V. Roberts, "Contour dynamics for the Euler equations in two dimensions", J. Comput. Phys., **30**, 96 (1979)

[59] K. S. Fine, C. F. Driscoll, J. H. Malmberg, and T. B. Mitchell, "Measurements of Symmetric Vortex Merger", Phys. Rev. Lett., **67**, 588 (1991)

[60] M. V. Melander, N. J. Zabusky, and J. C. McWilliams, "Symmetric vortex merger in two dimensions: causes and conditions", J. Fluid Mech., **195**, 303 (1988)

[61] D. G. Dritschel and D. W. Waugh, "Quantification of the inelastic interaction of unequal vortices in two-dimensional vortex dynamics", Phys. Fluids **A 4**, 1737 (1992)

[62] P. Tabeling, S. Burkhart, O. Cardoso, and H. Willaime, "Experimental study of freely decaying two-dimensional turbulence", Phys. Rev. Lett., **67**, 3772 (1991)

[63] Y. Pomeau, "Vortex dynamics in perfect fluids", J. Plasma Phys. **56**, 407 (1996)

[64] H. Aref, "Stirring by chaotic advection", J. Fluid Mech., **143**, 1 (1984)

[65] J. M. Ottino, "Mixing, chaotic advection, and turbulence", Annu. Rev. Fluid Mech., **22**, 207 (1990)

[66] G. M. Zaslavsky, R. Z. Sagdeev, D. A. Uskikov, and A. A. Chernikov, *"Weak chaos and quasi-regular patterns"*, Cambridge University Press, (1991)

[67] A. Babiano, G. Boffetta, A. Provenzale, and A. Vulpiani, "Chaotic advection in point vortex models and two-dimensional turbulence", Phys. Fluids, **6**, 2465 (1994)

[68] E. Ott, *"Chaos in dynamical systems"*, Cambridge University Press, (1993)

[69] G. Benettin, A. Giorgilli, L. Galgani, and J. M. Strelcyn, "Lyapunov characteristic exponents for smooth dynamical systems and for Hamiltonian systems; a method for computing all of them. Part 1: Theory, Part 2: Numerical applications", Meccanica, **15**, 21 (1980)